AWARD NUMBER: W81XWH-15-1-0147

TITLE: Virtual Tissue Modeling for Real-time Surgical and Interventional Procedure Simulation

PRINCIPAL INVESTIGATOR: Dr. Peyman Benharash, M.D.

CONTRACTING ORGANIZATION: University of California, Los Angeles

REPORT DATE: SEPTEMBER 2020

TYPE OF REPORT: Final Technical Report

PREPARED FOR: U.S. Army Medical Research and Materiel Command
Fort Detrick, Maryland 21702-5012

REPORT DOCUMENTATION PAGE

Form Approved
OMB No. 0704-0188

1. REPORT DATE	**2. REPORT TYPE**	**3. DATES COVERED**
SEPTEMBER 2020	Final Report	07/01/2015 – 06/30/2020

4. TITLE AND SUBTITLE

Virtual Tissue Modeling for Real-time Surgical and Interventional Procedure Simulation

5a. CONTRACT NUMBER
W81XWH-15-1-0147

5b. GRANT NUMBER

5c. PROGRAM ELEMENT NUMBER

6. AUTHOR(S)
Peyman Benharash, M.D.

E-Mail: benharash@gmail.com

5d. PROJECT NUMBER

5e. TASK NUMBER

5f. WORK UNIT NUMBER

7. PERFORMING ORGANIZATION NAME(S) AND ADDRESS(ES)

University of California, Los Angeles
11000 Kinross Ave, Ste 102
Los Angeles, CA 90095-2000

8. PERFORMING ORGANIZATION REPORT NUMBER

9. SPONSORING / MONITORING AGENCY NAME(S) AND ADDRESS(ES)

U.S. Army Medical Research and Materiel Command
Fort Detrick, Maryland 21702-5012

10. SPONSOR/MONITOR'S ACRONYM(S)

11. SPONSOR/MONITOR'S REPORT NUMBER(S)

12. DISTRIBUTION / AVAILABILITY STATEMENT

Approved for Public Release; Distribution Unlimited

13. SUPPLEMENTARY NOTES

14. ABSTRACT

This project aims to develop a platform for modeling of virtual tissues to be used in simulation of surgical and interventional procedures. The investigative team has made major advances in collection of mechanical tissue properties of the liver, integration into complex constitutive models, re-tooling the hemodynamic simulation model, and delivery of physics based visual models. Moreover, the group has been able to successfully demonstrate interaction of the virtual liver model with external forces including external shock wave and actual ballistic projectile. The results of the work performed during this award period have allowed for a physics-based model of tissue trauma and hemorrhage based on actual physical properties of the liver in a viscoelastic model, with superimposed hemorrhage using a smooth particle hydrodynamics method, in order to generate a high-fidelity virtual model of the said organ.

15. SUBJECT TERMS

liver constitutive modeling, material point methods, fluid/elastic multi-species continuum, hepatic tissue, hysteresis, compression, cardiovascular network simulation, hemorrhage modeling, smoothed-particle hydrodynamics

16. SECURITY CLASSIFICATION OF:			17. LIMITATION OF ABSTRACT	18. NUMBER OF PAGES	19a. NAME OF RESPONSIBLE PERSON
					USAMRMC
a. REPORT	b. ABSTRACT	c. THIS PAGE	Unclassified	125	19b. TELEPHONE NUMBER *(include area code)*
Unclassified	Unclassified	Unclassified			

Standard Form 298 (Rev. 8-98)
Prescribed by ANSI Std. Z39.18

TABLE OF CONTENTS

1. INTRODUCTION:

The UCLA Center for Advanced Surgical and Interventional Technology (CASIT) shall lead a R&D program, "Virtual Tissue Modeling for Real-time Surgical and Interventional Procedure Simulation," to develop and evaluate a new virtual tissue modeling methodology for use in military medical training simulators for forward surgical and interventional care of combat injuries.

2. KEYWORDS:

liver constitutive modeling, material point methods, fluid/elastic multi-species continuum, hepatic tissue, hysteresis, compression, cardiovascular network simulation, hemorrhage modeling, smoothed-particle hydrodynamics

3. ACCOMPLISHMENTS:

What were the major goals of the project?

The overall project goals are to develop a general framework for creation and sharing of virtual tissue models; create a prototype virtual tissue simulation of the liver and associated soft tissue and fluidic physiological systems; develop and integrate needed mathematical models, constitutive models, and interactive graphical models as a functional system of physics-based dynamic tissue simulations capable of real-time interaction appropriate for medical training simulators. The constitutive models shall be populated with validated physiological material properties. Virtual injury mechanisms and surgical tools shall be created for manipulation of the virtual tissue and methods developed for integrating component models (e.g. the liver) into a virtual patient body habitus model. Results shall be documented in a final report. The system shall be demonstrated in either a video or online interactive presentation format. The technologies and capabilities that shall be included are: computational simulation, graphical simulation, constitutive models, material property data acquisition, toolkits for injury and surgical procedures, and an online model repository and sharing system.

The goals for this project were the research and development in the following focal areas:

1. Fluid dynamics & tissue constitutive modeling
2. Numerical methods for real-time modeling
3. Biomechanical and graphical modeling of organs
4. Tissue properties measurement and validation
5. Body habitus graphical and physical modeling
6. Medical requirements and assessment
7. Open standards development for virtual anatomic models
8. Project advisory activity
    a) Formation of advisory panel of military medicine SMEs
    b) Formation of advisory panel of surgical and interventional simulation industry SMEs

What was accomplished under these goals?

1. Fluid dynamics & tissue constitutive modeling

There are two overall objectives of the fluid dynamics modeling team in this project. The first objective is to develop a comprehensive network model of the human cardiovascular system, with associated cardiac and autoregulation sub models, coupled with a fluid and nutrient transport model of the liver. The second major objective is to create a computational fluid dynamics simulation, based on smoothed particle hydrodynamics (SPH), of visualized bleeding from injury or surgical sites in the virtual model of the liver. These objectives are intertwined, since the visualized bleeding simulator requires the dynamic inflow conditions from the network model.

During Q1 of Y1 in fluid dynamics, in order to achieve these objectives, we planned to carry out several intermediate tasks. One task was to adapt the current cardiovascular network simulation tool (based in LabView) into a more modular and platform-independent form based on C++ or Python. In this adaptation, the tool would be extended to enable plug-in modules for organs, customizable physiological parameters, and a validation framework. Another task was to obtain—from medical imaging—a three-dimensional geometric model of the liver's three vascular trees, so that segments in the network model can be rigidly mapped to their proper geometric coordinates for use in the virtual injury and surgery functions. A third task was to adapt the current visualized bleeding simulator to the liver, which, in the short term, will require, e.g., a particle model of the liver geometry and surrounding abdominal cavity and organs, and some determination of porosity properties in liver tissue.

Q1 of Y1 contained preparatory stages of this work. One new graduate research assistant, supported by the project, carried out literature review and familiarized himself with the network simulation tool. A post-doc partially supported by the project fine-tunned the bleeding visualizations from earlier leg modeling work, which has direct impact on the tasks required for this project.

During Q1 of Y1 in tissue constitutive modeling, our constitutive modeling efforts focused on evaluation and comparison of the various stress-strain models in the current literature. Dr. Klug worked on a refactoring of his group's C++ finite-element code that will lead to more efficient numerical implementation of constitutive models and fracture algorithms for simulating cutting and tearing. He has also recruited a new Ph.D. student in Mechanical Engineering, Mr. Michael Reyes, and he began training Reyes in the development of the requisite numerical methods.

The Klug research group also completed the initial development of a new method for experimental characterization of tissue material properties. The method is specifically designed to ensure that parameters of a constitutive model are identified uniquely from a given experimental data set. Shockingly, uniqueness is not guaranteed by most approaches presented today in the literature. In order to overcome this limitation and regain the diagnostic capability of the identified material properties, during Q1 we completed and submitted a paper (Perotti, et al, 2015) in which we present a new method termed DEMO - Direct Equilibrium Matching Optimization. Our method is based on force and full-field displacement data, i.e., the displacement field due to the applied forces is known everywhere in the body of interest. This can be achieved clinically using magnetic resonance imaging. In our method, we impose the displacement field and minimize the difference between computed and experimentally measured forces (see Fig 1). When combined with material strain

energy functions based on the linear combination of polyconvex terms, DEMO determines the tissue material properties uniquely by minimizing a convex objective function. In the paper, we describe a new numerical strategy to obtain material energy laws that optimally describe the available experimental data. Moreover, a natural outcome of DEMO is the straightforward analysis of the reliability of the identified material properties. In the paper, we evaluated DEMO using passive myocardium experimental data at the material point and demonstrated its applicability to identify potentially diseased tissue with an in silico experiment modeling the passive ventricle.

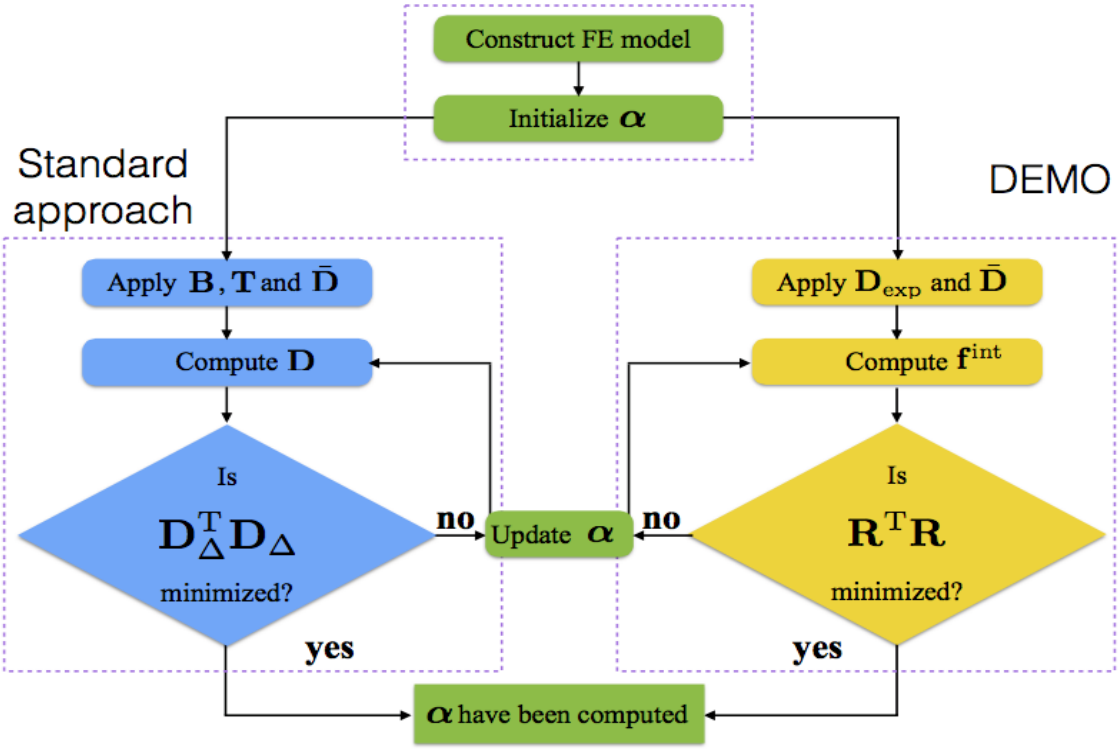

Fig. 1: Comparison of the Standard Approach — left — and the DEMO method — right — for material properties identification.

During Q2 of Y1 in fluid dynamics, we started our development on two target areas that will comprise the fluid dynamics component of the virtual tissue model.

The first target area involves the development of a modular real-time network model of the human cardiovascular system. This model will drive the local network model of the organ (liver) once that is developed. We started implementing this systemic model in an API (application program interface) format, which enables easy connection to other components of the overall tissue model.

The second target area involves the extension of our bleeding visualization framework to the liver. During this review period, we performed a preliminary simulation of bleeding from a static model of the liver. Since we still lack many details, such as the local pressure in the liver, the details of the injury geometry, and a mapping of the vasculature, we proceeded in an ad hoc manner in order to gauge our capabilities.

During Q2 of Y1 in tissue constitutive modeling, the constitutive modeling worked to develop mathematical models that characterize the mechanical response of liver tissue to applied loads the elastic mechanical response of liver tissue. Specific objectives are: 1) to characterize the spatial heterogeneity of elastic properties; 2) to couple tissue solid mechanics with fluid mechanics in the vasculature; and 3) to develop simulations of irreversible cutting, tearing, and rupture of tissue.

We continued the refactoring of our group's C++ computer code for implementation of new consititutive laws, especially oriented toward multiphysics models (for example, models coupling tissue elasticity to fluid flow). Dr. Klug also began discussions with Dr. Eldredge about possible approaches for coupled simulation of bleeding in deformable geometries. We resolved to focus on large-deformation poroelasticity as a modeling framework for bringing together tissue elasticity and blood flow. Plans were made to begin joint work with a new Ph.D. student in Mechanical Engineering, Yi-Jui Chang.

We also continued the evaluation of models from the literature for the elastic and viscoelastic response of both the liver capsule and parenchyma. We advised Dr. Teran and his group on how to structure the constitutive modeling components in the real-time FE code, specifically focusing on hyperelastic strain energy models, and variational constitutive updates for viscoplastic models.

During Q3 of Y1 in fluid dynamics, we continued our development on two target areas that will comprise the fluid dynamics component of the virtual tissue model.

The first target area involves the development of a modular real-time network model of the human cardiovascular system. This model, which provides local pressure and flow rate in the vascular tree, will drive the local network model of the organ (liver) once that is developed. We have now implemented this systemic model in an API (application program interface) format, which enables easy connection to other components of the overall tissue model. We evaluated the model by simulating a patient in a baseline (healthy) state and comparing with typical data.

The second target area involves the extension of our bleeding visualization framework to the liver. During this review period, we performed a pair of simulations of bleeding from a static model of the liver, improving the previous simulation by using a more realistic internal pressure in the liver to generate realistic oozing. We are still carrying these simulations out without detailed data for the liver, simply to refine our visualization approach.

During Q3 of Y1 in tissue constitutive modeling, the constitutive modeling team worked to develop mathematical models that characterize the mechanical response of liver tissue to applied loads the elastic mechanical response of liver tissue. Specific objectives are: 1) to characterize the spatial heterogeneity of elastic properties; 2) to couple tissue solid mechanics with fluid mechanics in the vasculature; and 3) to develop simulations of irreversible cutting, tearing, and rupture of tissue.

We have continued the refactoring of our group's C++ computer code for implementation of new constitutive laws, especially oriented toward multiphysics models (for example, models coupling tissue elasticity to fluid flow). This work is an important prerequisite for accomplishing all three of the above objectives.

Toward objective 1), Dr. Klug worked with a new Mechanical Engineering Ph.D. student, Yi-Jui Chang, on the review of a number of papers on mechanical properties of liver. Mr. Chang has begun to get familiar with hyperelastic constitutive laws for large-deformation elasticity, implementing some standard constitutive models in a C++ code.

Toward objective 2), Dr. Klug worked with Dr. Eldredge and the Fluid Dynamics team on coupling tissue solid mechanics with vasculature. In particular, Dr. Kwitae Chong, a postdoc on the Fluid Dynamics team was partially supported by Dr. Klug to begin working on a plan for coupled simulation of bleeding in deformable geometries. Also, Klug and Eldredge mentored Yi-Jui Chang in the study of large-deformation poroelasticity, which we have chosen as a modeling framework for bringing together tissue elasticity and blood flow.

During Q4 of Y1, we continued our development on three target areas that will comprise the fluid dynamics and elasticity components of the virtual tissue model.

The first target area involves the development of a modular real-time network model of the human cardiovascular system. This model, which provides local pressure and flow rate in the vascular tree, will drive the local network model of the organ (liver). We have now assembled a Matlab-based network model of the systemic arterial tree and the vasculature in the liver. We have also implemented an auto regulatory and cardiac sub model, and are exploring how to best combine this with the vascular sub model.

The second target area involves the extension of our bleeding visualization framework to the liver. During this review period, we have been preparing a simulation in which the liver is under active deformation during the bleeding visualization. This required some modification of our existing bleeding simulation framework. We expect results on this in the following quarter.

We also explored the equations of poro-elasticity, which govern the mechanics of a porous, elastic, fluid-filled material, such as the perfused liver. These equations will form the basis for the ultimate form of our virtual liver modeling, since they will account for the effect of blood (and bile) on the liver deformation, and also provide a clear coupling between the elastic deformation and the bleeding simulations.

There are two overall objectives of the fluid dynamics modeling team in this project. The first objective is to develop a comprehensive network model of the human cardiovascular system, with associated cardiac and autoregulation sub models, coupled with a fluid and nutrient transport model of the liver. The second major objective is to create a computational fluid dynamics simulation, based on smoothed particle hydrodynamics (SPH), of visualized bleeding from injury or surgical sites in the virtual model of the liver. These objectives are intertwined, since the visualized bleeding simulator requires the dynamic inflow conditions from the network model.

During Q1 of Y2, we continued our development on three target areas that will comprise the fluid dynamics and elasticity components of the virtual tissue model.

The first target area involves the development of a modular real-time network model of the human cardiovascular system. This model, which provides local pressure and flow rate in the vascular tree,

will drive the local network model of the organ (liver). We have now combined the various component submodels — systemic vasculature, cardiac, and autoregulation — into a single Matlab-based model, and demonstrated its performance on a basic hemorrhage event. The vascular submodel is expressed in the frequency domain, wshile the other submodels are in the time domain.

The second target area involves the extension of our bleeding visualization framework to the liver. During Q1 of Y2, we have performed a visualization of hemorrhage during a ballistic penetration of the liver. This is the first time in which we have coupled the bleeding simulation to the deforming liver geometry, so it's an important milestone. We are currently pursuing a longer-duration simulation of a similar injury event.

We have also been exploring the equations of poro-elasticity, which govern the mechanics of a porous, elastic, fluid-filled material, such as the perfused liver. These equations will form the basis for the ultimate form of our virtual liver modeling, since they will account for the effect of blood (and bile) on the liver deformation, and also provide a clear coupling between the elastic deformation and the bleeding simulations. In this quarter, we have established the governing equations and proposed a candidate hyperelastic constitutive model for liver tissue.

During Q2 of Y2, we continued our development on three target areas that will comprise the fluid dynamics and elasticity components of the virtual tissue model.

The first target area involves the extension of our bleeding visualization framework to the liver. During this quarter, we carried out a more refined and longer-duration simulation of a ballistic penetration of the liver. We are currently pursuing a second simulation involving a complete resection of the liver. These simulations have been very promising, and have been helpful for refining our procedures for introducing computational blood particles into the scenario. For example, we now are able to determine which major vascular segments in the three major networks (portal vein, hepatic artery, hepatic vein) within the liver have been severed by a given injury, and introduce bleeding from these precise locations.

However, the simulation still relies on a few ad hoc aspects: one, we are only guessing at the pressure and flow rate of the severed vessels; and two, we carry out the simulation as a one-way coupling: tissue deformation and failure is simulated first, and these are used a posteriori to simulate bleeding in a geometry of prescribed deformation. Both of these aspects are currently being addressed.

In order to obtain pressure and flow rate at the site of the injury (or treatment), we have been developing a modular real-time autoregulated network model of the cardiovascular system and a local network model of the liver. In the previous quarter, we recognized some drawbacks of our previous submodel of the systemic vasculature, which had been expressed in the frequency domain. During this quarter, we have been developing a time-domain version of the submodel, which enables more consistency and flexibility when connecting it to the cardiac and autoregulatory submodels. This work should be completed by the end of the next quarter.

In order to more strongly couple the dynamics of the bleeding and the tissue deformation, we have been developing the equations of poro-elasticity, which govern the mechanics of a porous, elastic,

fluid-filled material, such as the perfused liver. These equations will form the basis for the ultimate form of our virtual liver modeling, since they will account for the effect of blood (and bile) on the liver deformation, and also provide a clear coupling between the elastic deformation and the bleeding simulations. In this quarter, we have been carrying out some preliminary simulations of poro-elasticity in simple scenarios, such as a wet sponge under compression.

During Q3 of Y2, we continued our development on three target areas that will comprise the fluid dynamics and elasticity components of the virtual tissue model.

In the first target area, we applied our bleeding visualization framework to a complete resection of the liver. This virtual resection exposed a number of severed vascular segments in the associated network model of the liver vasculature. Computational blood particles were introduced at the distal ends of these segments and allowed to flow, using approximate flow rates based on the flow into the hepatic artery. This was mostly carried out to develop more guidance on how much resolution is needed to achieve a good rendering of the bleeding. The movie is embedded below:

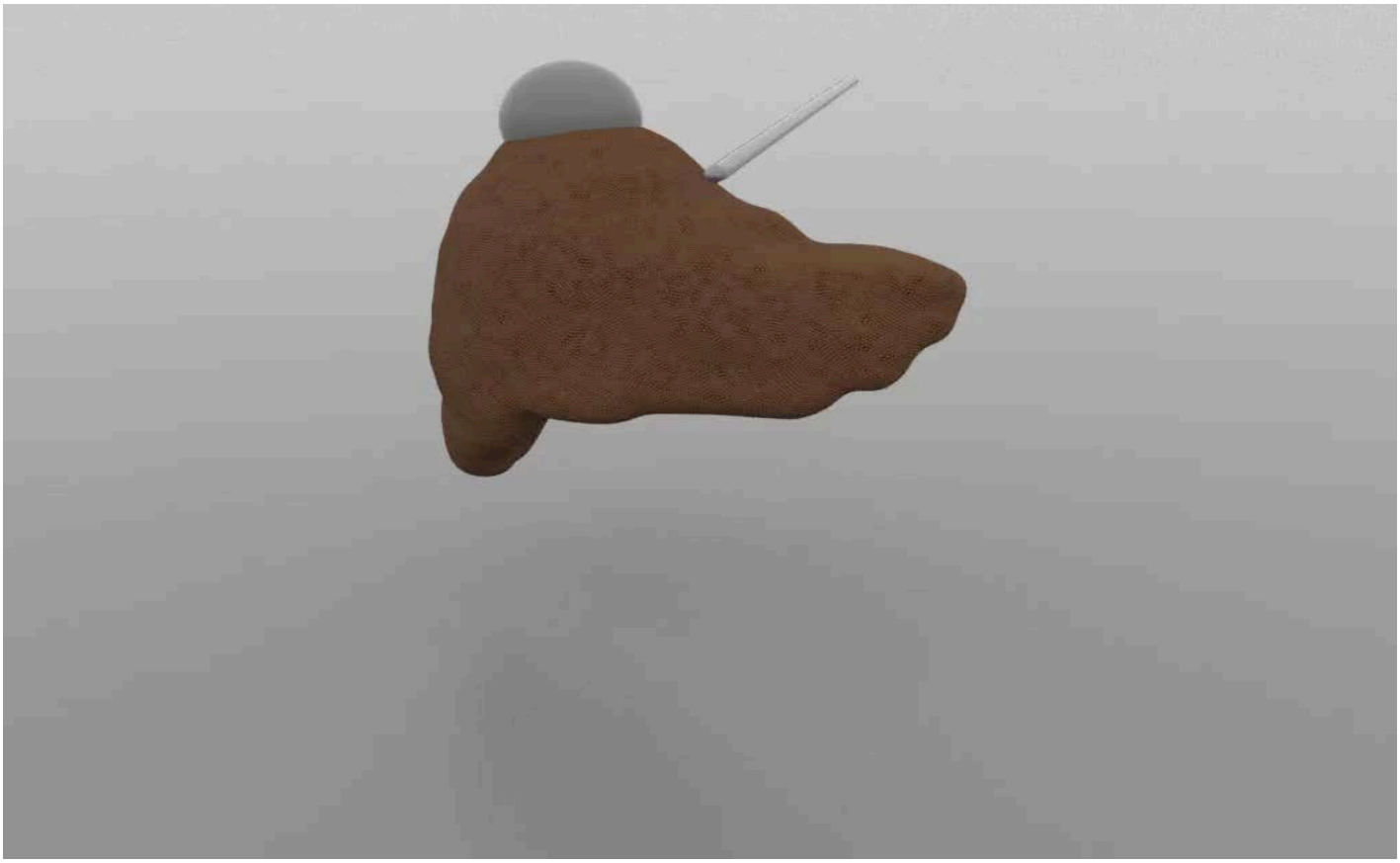

As mentioned in the previous report, the simulation still relies on a few ad hoc aspects: one, we are only guessing at the pressure and flow rate of the severed vessels; and two, we carry out the simulation as a one-way coupling: tissue deformation and failure is simulated first, and these are used a posteriori to simulate bleeding in a geometry of prescribed deformation. Both of these aspects are currently being addressed, as we describe below.

In order to obtain pressure and flow rate at the site of the injury (or treatment), we have been developing a modular real-time autoregulated network model of the cardiovascular system and a local network model of the liver. During this quarter, we mostly completed our time-domain version of the 1-d vascular submodel, and this is closed with the cardiac and neurogenic regulatory submodels. The code was originally written in Matlab, a non-compiled language that isn't very efficient, so we will rewriting this in Julia, a very good and modular language that exhibits much better performance. We will also be testing the full cardiovascular model with reported results in the literature.

In order to more strongly couple the dynamics of the bleeding and the tissue deformation, we have been developing the equations of poro-elasticity, which govern the mechanics of a porous, elastic, fluid-filled material, such as the perfused liver. In this quarter, we implemented the governing "bi-phasic" equations for this model, using Smoothed Particle Hydrodynamics (SPH), the same methodology that we had previously used for just the blood phase in our uncoupled visualizations. Here, we have used SPH for the solid phase, as well. This SPH bi-phasic simulation tool is completely novel. We have begun carrying out simulations of simple configurations of a spongy cubic specimen: compression (with associated ejection of the liquid phase) and expansion (the absorption of liquid from a bath in which the specimen is immersed). These have allowed us to tune some of the numerical parameters.

During Q4 of Y2, we focused on the continuing development of the two target areas that will comprise the fluid dynamics and elasticity components of the virtual tissue model: a simulation tool for the coupled fluid-tissue mechanics of liver and its constituent liquids, driven by an auto-regulated model of the full cardiovascular system. We also completed our efforts on our "uncoupled" bleeding visualizations, since these will be supplanted by the coupled fluid-tissue simulations.

The overall objective of this simulation framework is to enable a physics-driven, visually faithful rendering of the liver, when subjected to various injuries or surgical interventions. This requires

- A simulation of the liver tissue mechanics, with material properties obtained by mechanical testing of liver samples, coupled with
- A simulation of the spatially resolved flow of the homogeneous interstitial blood (and bile) phase in the perfused tissue
- A complete set of dynamically-variable "inflow" and "outflow" conditions for the liver, from the systemic vasculature and cardiac function, and the feedback control provided by the autonomic response to, e.g. hemorrhage or pharmacological intervention.

We have pursued the first two of these in a fully coupled manner, through a bi-phasic computational model, in which the solid (tissue) and liquid (blood and bile) are regarded as superimposed phases, which interact through relative drag force and a constraint that preserves their total volume fraction. This model accounts for essential physical behaviors: tissue swelling by absorption of liquid, expulsion of liquid by local compression, and overall mechanical response of the perfused tissue under various loadings. Beginning with the previous quarter, and continuing in this quarter, we have computationally implemented these equations with Smoothed Particle Hydrodynamics (SPH). We have been testing and refining this implementation using simple scenarios that allow us to identify

and fix problems that would also be present in the full liver simulation. Among these simple problems are the mechanical tests pursued by the Candler research group on this team.

In parallel with this, we have also been addressing the other component, the cardiovascular model. We have developed and implemented (in a language called Julia) a modular real-time autoregulated network model of the cardiovascular system. During this quarter, we have been evaluating this computational model against reported results in the literature, such as the pulsatile waveform generated at the ascending aorta under normal physiological conditions, the evolution of the pressure and flow rate signals into the major peripheral arteries, and the behaviors of the heart rate, systemic vascular resistance, and other gross physiological parameters in response to disruptions that trigger the sympathetic and parasympathetic nervous system. One of these triggers will, of course, be hemorrhage in the liver, so we place a premium on getting this response correct.

During Q9, we focused, as in the previous period, on the development and implementation of the two target areas that will comprise the fluid dynamics and elasticity components of the virtual tissue model. Below is a snapshot for one test case, in which a cubic liver specimen, initially perfused with blood, is also supplied continuously with blood at the specimen's center. The specimen is inside of a container, which traps the draining blood. The upper snapshots show the blood (red particles) and the tissue (blue particles) at two different stages, and the lower snapshots depict just the tissue, which shows the relaxation (under gravity) and the subsequent swelling. The simulation framework is based on the method of Smoothed Particle Hydrodynamics (SPH).

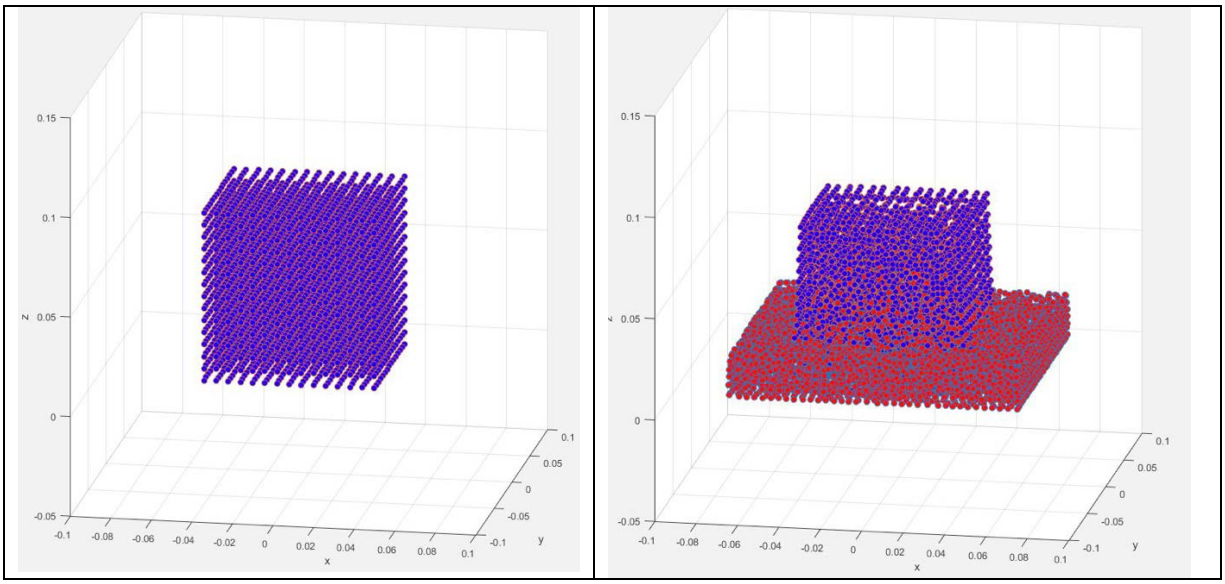

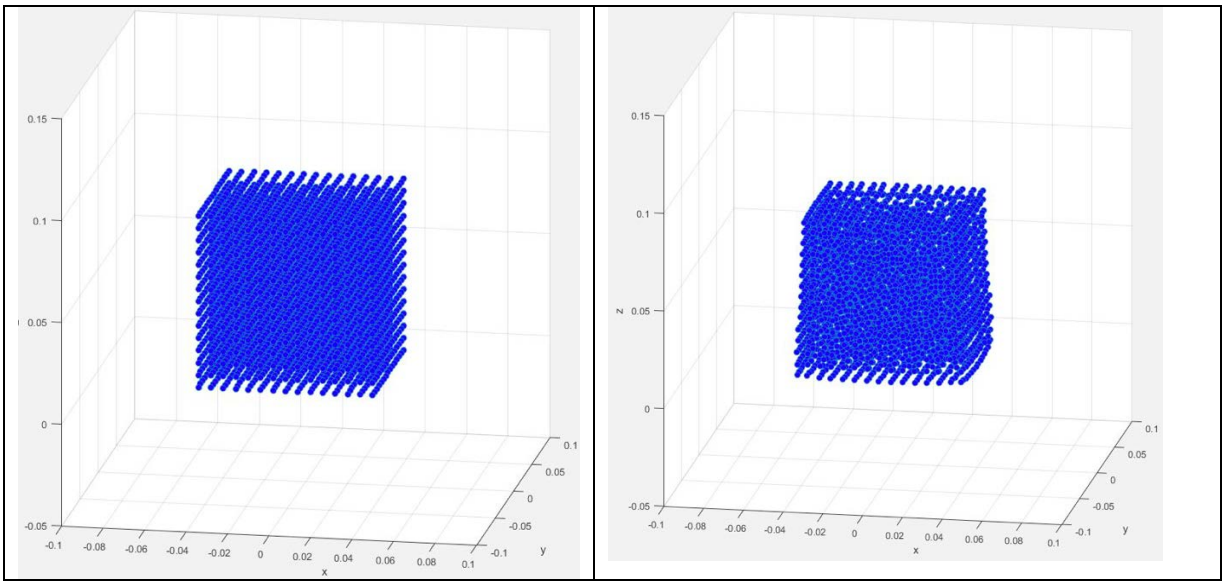

In parallel with this, we have also been addressing the other component, the cardiovascular model. We have developed and implemented (in a language called Julia) a modular real-time autoregulated network model of the cardiovascular system. During this quarter, we have finished our testing of the simulation tool, evaluating it on criteria such as the pulsatile waveform generated at the ascending aorta under normal physiological conditions, the evolution of the pressure and flow rate signals into the major peripheral arteries, and the behaviors of the heart rate, systemic vascular resistance, and other gross physiological parameters in response to disruptions that trigger the sympathetic and parasympathetic nervous system. One of these triggers will, of course, be hemorrhage in the liver, so we place a premium on getting this response correct. The methodology and results have been submitted for publication to the journal *International Journal for Numerical Methods in Biomedical Engineering*.

During Q10, we have pursued more sophisticated mechanical tests of the fully-coupled biphasic computational simulations of the liver sample, including the movie embedded below, which depicts a projectile passing through the perfused sample. These tests enable us to develop and refine the various mechanisms that constitute tissue response, failure, and interaction with perfused blood.

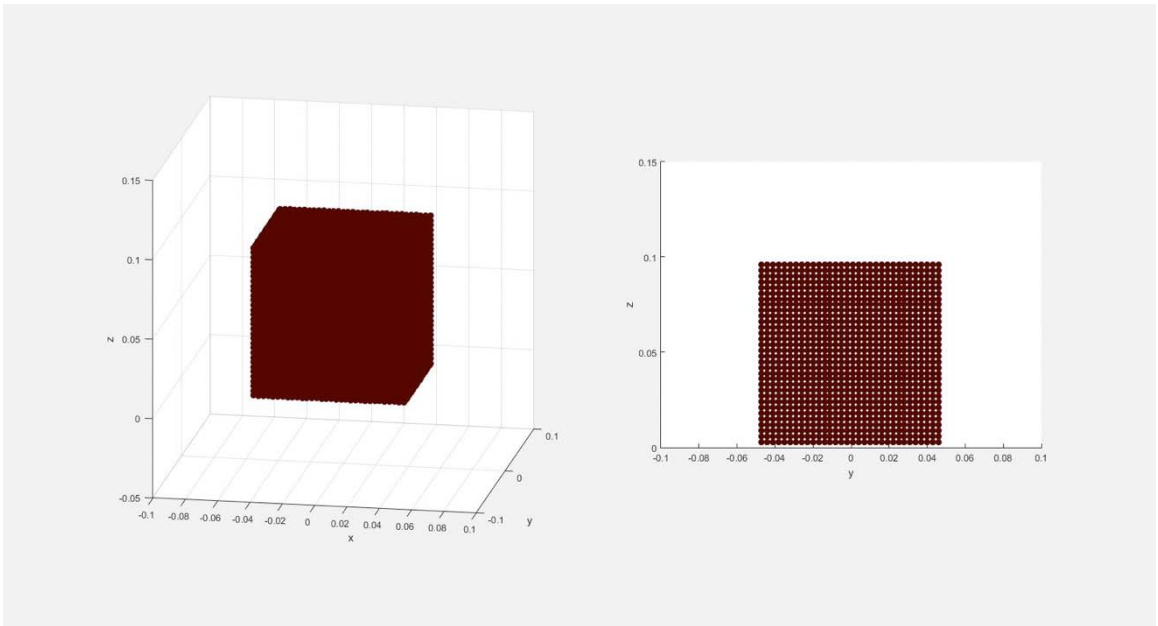

In parallel with this, we have also been addressing the other component, the cardiovascular model. We have developed and implemented (in a language called Julia) a modular real-time autoregulated network model of the cardiovascular system. During this quarter, we have revised our previously-submitted paper to the journal *International Journal for Numerical Methods in Biomedical Engineering*. We have also been planning the software links between this cardiovascular model and the biphasic model of the liver.

During Q11, we have carried out a wide array of mechanical tests of a virtual cubic tissue sample — including gravity-driven drainage when initially perfused with blood and indentation tests of the perfused sample. We have also begun to couple the virtual tissue model with our autoregulated cardiovascular simulator.

Our paper on the cardiovascular simulator was published in International Journal for Numerical Methods in Biomedical Engineering, and can be found here.

During Q12, we have completed more tests, including impact by a high-speed projectile and drainage during continuous perfusion. The second of these was achieved by coupling with our autoregulated cardiovascular model.

The cardiovascular model itself has also been the subject of significant effort in this quarter. We are pursuing the use of data assimilation, in order to incorporate real-world measurements that improve the overall fidelity of the model. In this quarter, we have carried out a simple test of this approach. By assimilating real measurements of flow through the pulmonary artery, we have been able to use an extracted part of our overall cardiovascular model in order to predict the pressure waveform in the pulmonary artery, and from this, detect differences between healthy patients and those with pulmonary hypertension. Though pulmonary hypertension is not explicitly related to the overarching virtual tissue modeling effort, the data assimilation framework will allow us, in ongoing work, to determine more accurate model parameters from conventional medical monitoring data.

During Q13, we carried out a test on the full-scale liver model. In this test, the liver was subjected to a complete resection, carried out by applying a scalpel to the computational model that cut through the tissue. This resection cut through the outer layer and exposed the perfused tissue, allowing blood to drain. The complete set of tests can be seen here. The link is to a video submitted by our team to the Gallery of Fluid Motion at the American Physical Society's Division of Fluid Dynamics meeting.

We have also been carrying out an investigation of the use of data assimilation to improve fidelity of our cardiovascular modeling tool. In the previous term, we had used data assimilation to improve a limited cardiovascular model, of the pulmonary circulation. In this term, we began exploring the sensitivity of various common measurement modalities (e.g. brachial pressure, cardiac output) to variations in model parameters in the overall cardiovascular model. This sensitivity study provides essential information for determining what parameters can be tuned most effectively from measurement data. This process is carried out within an Ensemble Kalman Filter, which utilizes an ensemble of randomly-perturbed versions of the model. The mean of the ensemble results provides the prediction, and the spread of results provides an estimate of the uncertainty. Both are essential for constructing a modeling framework that can be applied on a patient-specific basis. In future work, this data assimilated cardiovascular model, in conjunction with the virtual tissue model, can be used to provide reliable simulations of liver injury and surgery.

During Q14, we presented our work on both the virtual tissue modeling and on the data-assimilated cardiovascular modeling at the American Physical Society's Division of Fluid Dynamics meeting. We also have been preparing the virtual tissue modeling work for journal publication. This paper is nearly completed and will be submitted next quarter.

The sensitivity study of the cardiovascular model, started in the previous quarter, has been completed. We are also using the data assimilation framework for a different subtask now: determining optimal parameters for outlet impedance boundary conditions for CFD simulations. We are working with a CFD simulation of the lower leg for this task. Though it is not directly related to the virtual tissue modeling, it expands our capabilities for developing patient-specific models for biomedical simulation and training.

During this review period, we put final touches on the development and implementation of the two components that comprise the fluid dynamics and elasticity components of the virtual tissue model: a simulation tool for coupled fluid-tissue mechanics; and a data-assimilated model of the full cardiovascular system.

In this period, we validated our coupled fluid-tissue simulation framework on several benchmark problems, including vibration of a cantilever beam and the flow through a static porous medium, performing convergence test on the second case, demonstrating good agreement with test problem. We also reimplemented our SPH solver from CPU-based to GPU-based , improving the computational efficiency by a factor of 10. The figure below exhibits this efficiency and its scalability to (more realistic) simulations with more computational particles. We made our simulation framework more general by adding a surface tension formulation at the interface between liquid and air. The liquid droplet now maintains its shape on a plane due to surface tension, as shown in the figures below, rather than spreading outward unphysically. We will imminently submit a paper on our computational framework for fluid-tissue modeling.

The methodology and results of the basic model have already been published in the journal *International Journal for Numerical Methods in Biomedical Engineering*.
During this period, we have refined our data assimilation framework for the cardiovascular model, using real measurement data to accurately estimate the model parameters of (1) a pulmonary circulation model, successfully distinguishing the characteristics healthy patients and those with

pulmonary hypertension, and (2) a circulatory model of the lower leg, focused on modeling diabetic patients. This framework can be used, for example, to determine optimal inlet and outlet boundary conditions for high-fidelity computational fluid dynamics simulations of the modeled geometries. In particular, it is used to drive the SPH-based fluid-tissue simulations in the liver. We have published a paper on the data assimilated cardiovascular model to a special issue on Machine Learning in Fluids in the journal *Theoretical and Computational Fluid Dynamics*.

2. Numerical methods for real-time modeling

During Q1 of Y1, PI Teran and postdoc Chenfanfu Jiang wrote a new code for the finite element (FEM) simulation of the liver as a homogeneous, isotropic hyper elastic Mooney-Rivlin solid. This agrees with the observations in the literature. A still frame from one of these sims is below. The geometry of the liver was built from a procedural model of the surface geometry and various resolution tetrahedron meshes were created for simulation purposes. In the future, we will build these methods directly from patient specific scanning data.

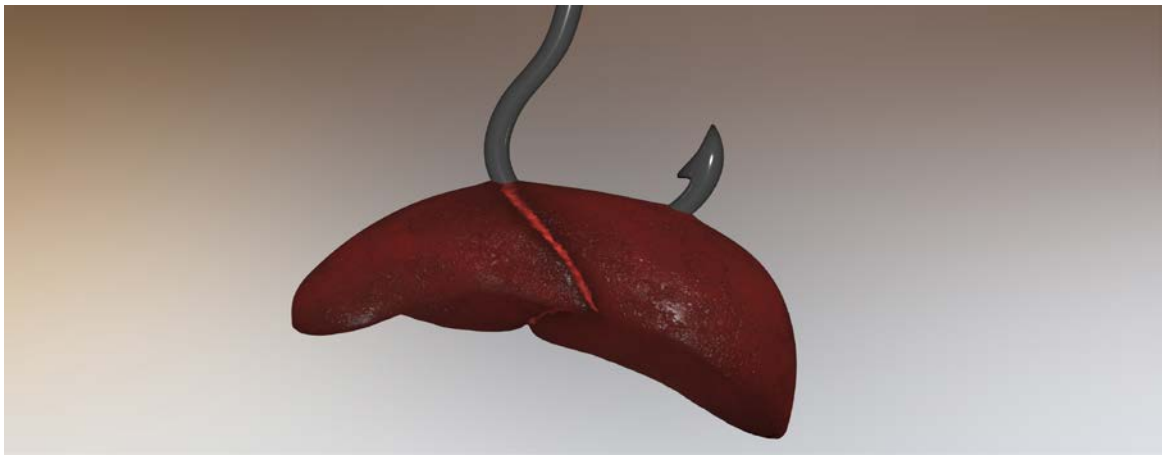

The PIs started regular meetings for designing the process of determining constitutive parameters from experimental and imaging data sources. These meetings are biweekly and will help finalize our suggested mechanical response. While initial efforts have characterized the model as hyper elastic, the final model needs to include some viscous effects and these aspects are also being hypothesized in the meetings.

During Q2 of Y1, PI Teran and his group continued developing a new code for the finite element (FEM) simulation of the liver. They have developed a framework that should allow for easy creation of subject specific liver models from scan geometries obtained from PI Santhanam. Also, they have developed a framework for simulating a wide range of elastoplastic constitutive laws, as well as treatment of surface based elasticity. These new techniques allow for discretization of plastic flows described by very general yield surfaces and associative and non-associative flows. A discrete return mapping algorithm has been developed that works with both semi and fully implicit time discretization.

Teran and his group have investigated and are still developing a new vectorization/SIMD friendly singular value decomposition (SVD) algorithm for large arrays of 3X3 matrices. This is needed for

the elastoplastic discretization of the liver constitutive model. The new technique improves on accuracy of a rival technique developed by the PI a few years ago, and also provides improved accuracy. Furthermore, they are investigating a new optimization class of integrators for solving implicit equations with added efficiency.

During Q3 of Y1, we continued to develop three different aspects of the simulation infrastructure. First, we are developing a Material Point Method (MPM) based simulation of liver with surface membrane elasticity combined with elastoplastic interior. We have developed a new class of algorithms capable of treating a wide range of elastoplastic models to help facilitate the creation and testing of subject specific constitutive models. One of the primary advantages of the MPM approach is the treatment of failure and self-contact. MPM does not require any modifications to its basic implementation to treat these phenomena and this allows for more efficient simulations. Once complete, this infrastructure should let us synthesize a number of injuries (including blast wave and projectile based trauma) and subsequent surgical repairs.

The second aspect of our development is concerned with new optimization techniques for solving the nonlinear equations needed with implicit time stepping. Implicit time stepping allows for maximal computational efficiency, but this is contingent upon the ability to robustly and efficiently solve the equations. We are investigating a new class of methods that give stable results with far fewer iterations than the more commonly used Newton iteration. This is proving to provide drastic performance improvements, independent of other factor such as parallelization.

Lastly, we are developing a new code base that can be released to the computational and surgical community to allow others to use the simulation techniques.

During Q4 of Y1, we developed new algorithms for simulating the failure of the surface membrane used in the MPM simulation of the liver. While traditional MPM naturally allows for failure, the addition of the surface elastic membrane requires a novel treatment. This allowed us to simulate ballistic based traumatic injury of the liver at unprecedented level of detail. We gave a demo of this functionality at the meeting in May.

We also continued our efforts with fine tuning the constitutive relation for the mechanical response of the liver tissue. This has been complicated by the tragic loss of Professor William Klug. The groups of Teran and Eldredge have doubled our efforts to compensate for the loss of expertise that only Professor Klug could provide. Despite this loss, we are making good progress. We have modified our model to include the effects of pre-stress in the liver. We have also developed a new approach that allows us to model the blood and elastic tissue interaction as a porous medium. This novel development is proving very powerful and is giving us a wide range of new functionality to explore.

During Q1 of Y2, we further developed the constitutive model of the liver including the effects of blood as a porous multi-species medium. We will soon enter into a fitting stage where we directly fit experimental observation with our model.

We additionally included the effects of damage/topological change of the vascular during traumatic injury simulation. We have further developed an excision tool to allow for simulated surgical manipulation, e.g. in response to the traumatic injuries we have simulated.

We now have a model that consists of an elastic surface membrane, a hyperelastic bulk interior, an embedded elastic vascular as well as a porous fluid matrix. Furthermore, this model can be simulated with considerable flexibility to topological change and extreme deformation.

During Q2 of Y2, we completed an investigation of coupling terms between the porous fluid matrix and the bulk fluid interior of the liver. We use a multi-species continuum approach to do this. Blood is modeled as its own continuum species and the elastic fluid matrix as another. The two materials individually obey conservation of mass and momentum. The mass density and momentum of the fluid/matrix model is the sum of the individual species mass density and momentum. This defines the velocity of the combined phases as the mass average velocities of the species and balance of linear momentum follows if we define the effective fluid/matrix stress as the sum of the individual species stresses. The individual species momenta evolve under the influence of their local stress, as well as a momentum exchange term between the species. This term is stiff and we have developed appropriate implicit time stepping treatments of the term. This is done via the material point method (MPM). Our initial investigations have included the effect of the vascular structure in the elasticity and we have demonstrated our method on oozing and bleeding following liver surgical incision. We have also begun the model fitting phase for with a suite of experiments that can be used to fit the model to data.

During Q3 of Y2, we have continued the process of fitting our model to experimental data. We designed and started the development of surgically relevant simulation examples involving sutures incisions in soft tissues. We explored various algorithmic options for this.

This quarter we completed an investigation of coupling terms between the porous fluid matrix and the bulk fluid interior of the liver. We use a multi-species continuum approach to do this. Blood is modeled as its own continuum species and the elastic fluid matrix as another. The two materials individually obey conservation of mass and momentum. The mass density and momentum of the fluid/matrix model is the sum of the individual
species mass density and momentum. This defines the velocity of the combined phases as the mass average velocities of the species and balance of linear momentum follows if we define the effective fluid/matrix stress as the sum of the individual species stresses. The individual species momenta evolve under the influence of their local stress, as well as a momentum exchange term between the species. This term is stiff and we have developed appropriate implicit time stepping treatments of the term. This is done via the material point method (MPM). Our initial investigations have included the effect of the vascular structure in the elasticity and we have demonstrated our method on oozing and bleeding following liver surgical incision. We have also begun the model fitting phase for with a suite of experiments that can be used to fit the model to data.

During Q4 of Y2, we have continued the process of developing new techniques for cutting soft tissues in Material Point Method simulations. Furthermore, we have developed a framework for generating libraries of simulation data that will serve as the enabling technology for real-time computing applications. We hope to achieve real-time technology by leveraging advances in

machine learning and we are investigating how this can be done in the context of soft tissue simulation.

During Q9, we have continued the process of developing new techniques for cutting soft tissues in Material Point Method simulations. We continue to develop a machine learning approach to real time simulation. We are also investigating the simulation of membrane stiffness and suture torsional resistance in our MPM simulation context.

During Q10, we developed a few new network models for the machine learning framework and we tested a few more virtual tissues configurations to assure robustness/effective generalization from the simulation data. We also developed an MPM technique for collision resolution with co-dimensional objects with appreciable thickness/bending resistance that will serve as a starting point for strands and sutures.

During Q11, we investigated different strand models and ultimately build on the work of Begou et al., Discrete Elastic Rods, ACM Transactions on Graphics, 2008. We are working on how to incorporate this in to our MPM computational framework. We also made good progress on how to simulate injuries to soft tissues via ductile failure.

During Q12, we made good progress on the suture/strand modeling by abandoning the updated Lagrangian nature of MPM. We had to augment our model with new collision impulses based on purely Lagrangian considerations. We showed that this is still efficient and robust.

During Q13, the suture/strand model continues to resolve a good number of new phenomena, including simple contact and collision issues that we found were clearly an issue with our older approaches. We also made big strides in developing tissue failure visualization. Our discovery is a big improvement over the model we used in prior years.

During Q14, we successfully submitted two papers related to our work on sutures/strands and ductile failure of soft tissues.
These papers were accepted at the ACM SIGGRAPH/Eurographics Symposium for Computer Animation. The paper on the simulation info ductile failure of tissues and related materials was awarded best paper. Our new techniques will vastly improve the level of detail possible with MPM simulation of soft tissues and more generally for ductile failure. Notably our technique allows us to run simulations with accuracy that would normally be only achievable with much higher (and thus more computationally expensive) spatial resolution.

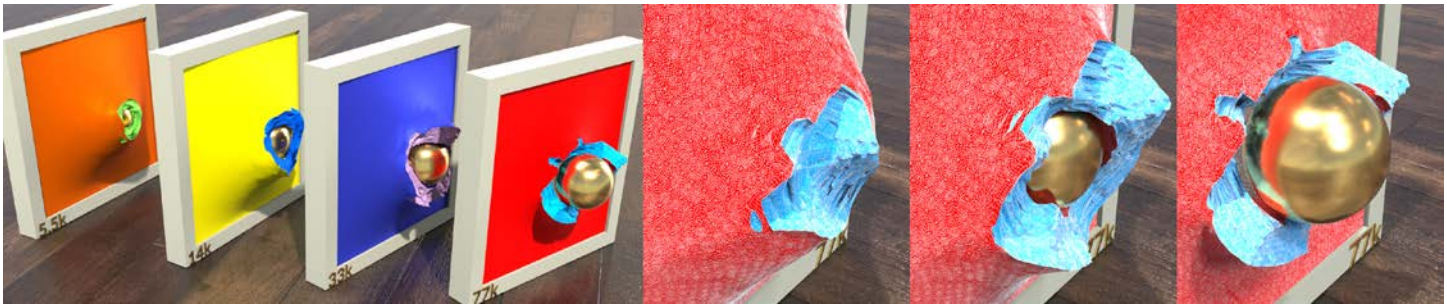

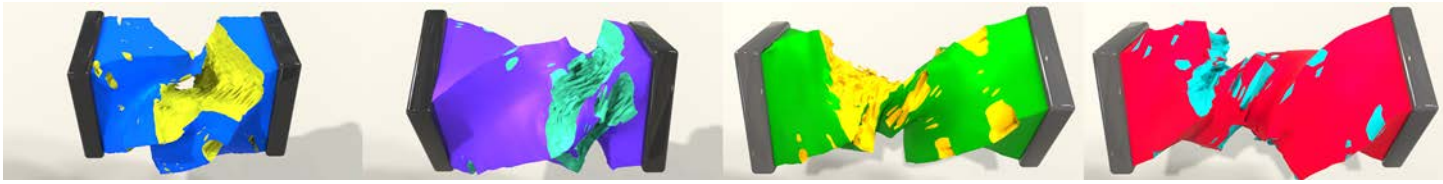

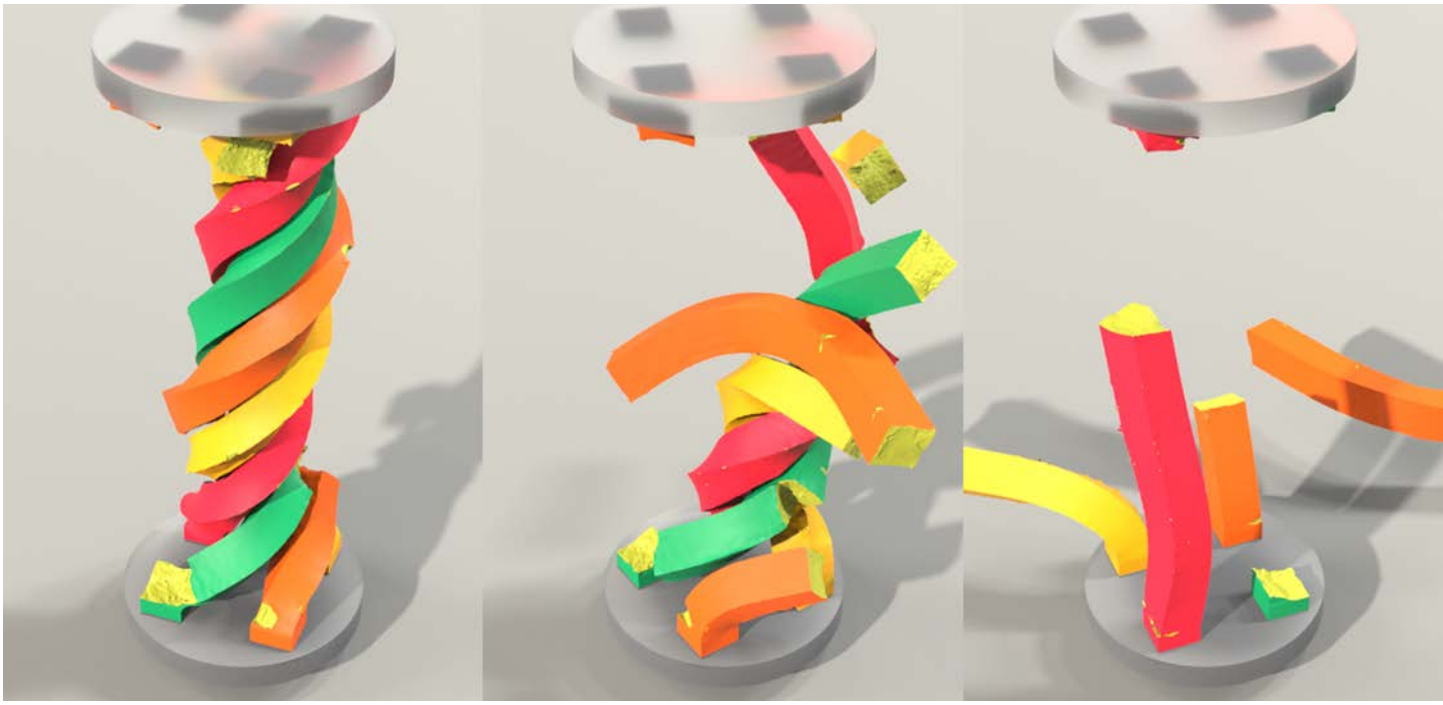

3. Biomechanical and graphical modeling of organs

During Q1 of Y1, the graphics modeling of the liver anatomy was based on a patient-specific anatomy obtained from imaging protocols such as the CT and gated MR systems. During the Q1 of the year 1, we focused on developing methodologies for processing CT and MR imaging system to segment liver anatomy, perform 3D mesh generation and estimate 3D liver motion during the breathing process. Fig (a) shown below depicts a high-resolution liver image acquired from a CT image scans. Each finite element shown here is a 1 mm^3 mesh element and each element also includes the internal constituents such as the blood vessels and parenchymal structures. Fig (b) shown below demonstrates a GPU based implementation of a linear deformation model of the liver generated from the high-resolution anatomy. The green colored elements show regions where no deformation was observed. The model was perturbed with a spherical bolus for deformation purposes. The blue region shows the tissue construction caused by the spherical bolus.

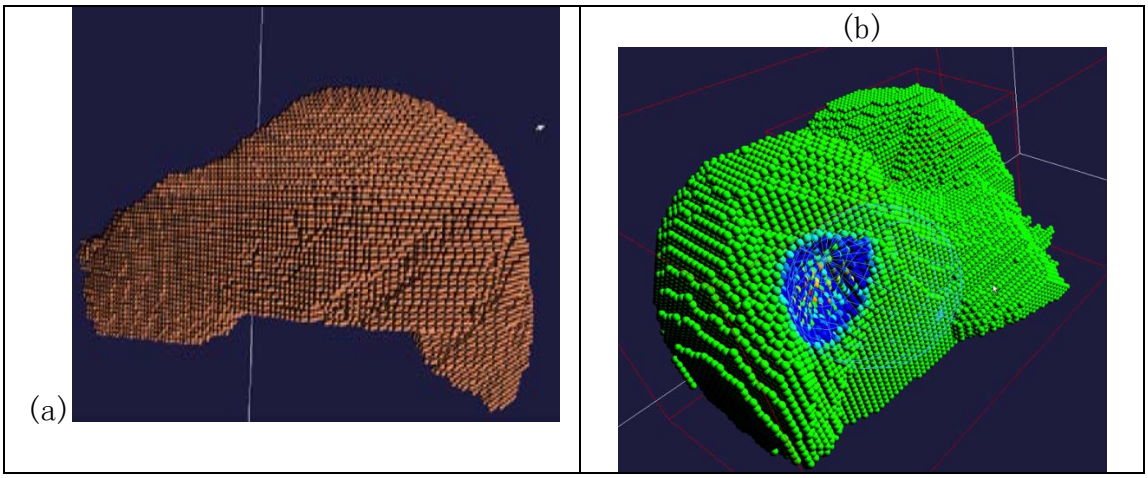

Fig (a) shown below depicts the lung (in pink) and liver (in brown) geometry and how they are placed with each other. Lung expands and contracts during breathing causing the liver to compress during the inhalation and expand during the exhalation. Fig (b) shows the regional lung expansion and liver contraction during the inhalation and fig (c) demonstrates the liver stretching during the exhalation. Here the lung surface is shown in blue (during inhalation) and red (during exhalation) because of its outward construction and inward stretching. The process consisted of both regional tissue expansion (in blue) and contraction (in red) in both liver and lungs.

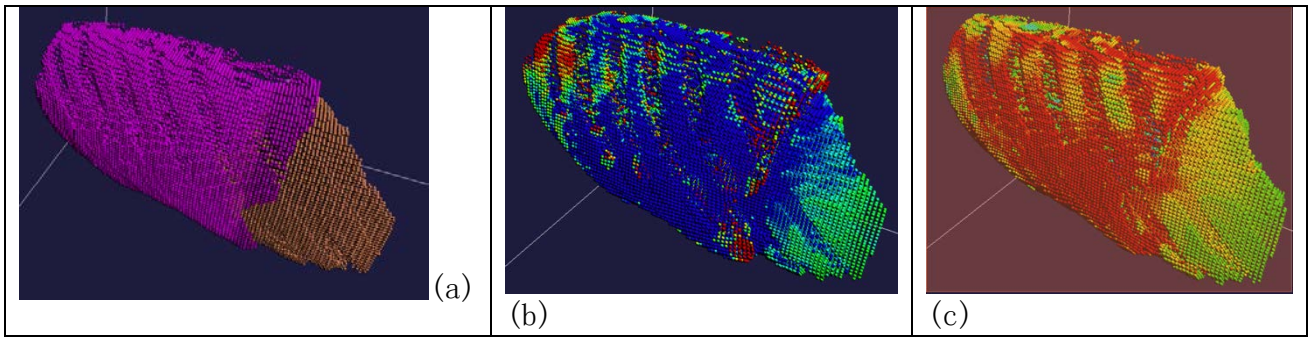

During Q2 of Y1, automatic quantification of the registration accuracy for liver image processing was studied as described below.

Errors and artifacts during the imaging process may lead to errors in the DIR procedure and subsequently errors in the treatment delivery and ultimately a lowered treatment efficacy. Errors in the imaging process stem from internal structures (e.g. parotid glands) that are both not clearly visible with on-board imaging as well as deform during the patient setup for subtle changes in the patient posture. Artifacts in the on-board imaging may stem from a high signal-to-noise ratio (SNR) and implants in the patient anatomy. The gold standard for quantitatively assessing registration accuracy is manually placed landmarks. However, placing landmarks are time consuming, user dependent, and suffer from small sample size. ISMs provide a mathematical formulation for quantifying the similarity of two intensity fields but provide little value without proper context.

Since the above-mentioned errors and artifacts are both patient and anatomy specific, there is a need to quantify the DIR accuracy on a subject-specific and site-specific basis, which forms the focus of

this paper. Developing a formulation that encapsulates the image similarity would enable quantifying the DIR accuracy. The process is limited by the lack of validation datasets that can be used for setting the formulation. Conventional approach to validate DIR is to employ landmark-based approach, which for our purposes, is cumbersome and may be affected by inter-subject differences in the ground-truth. Image Similarity Metrics such as the Mutual Information (MI), Entropy Correlated Coefficient (ECC) are potential metrics that can be used for quantifying the DIR accuracy. They are however limited by the fact that their usage has not been parameterized yet.

This work aims to propose and test a formulation, which is based on image similarity metrics (ISMs) for processing 4D liver imaging, to provide a robust quantification of DIR accuracy. The key contribution of this paper is (a) to formulate the parameterized way to quantify DIR accuracy on a patient and site-specific basis, and (b) to quantify the DIR accuracy using high-resolution biomechanical models. To our knowledge, such a method has not been previously investigated. Such a metric can also be eventually integrated into the DIR procedure to ensure the registration procedure can be constrained for specific accuracy requirements.

The parameterization process was numerically quantified as follows. We employed the biomechanical head and neck model to generate changes in the patient posture and physiological changes. Specifically, for the case of head and neck anatomy, we simulate biomechanical deformation at three different neck rotations and tumor regression at 15 and 25 percent volume reduction. For each of the combination, a kVCT, Cone Beam CT (CBCT) and Mega Voltage CT (MVCT) was generated. The Gaussian SNR for each image was set to 4.0 as commonly observed for 4D imaging. In addition, for each contoured structure inside the head and neck anatomy, landmarks were automatically generated to quantify the DIR accuracy. A total of 4500 landmarks were generated for each of the 15-patient geometry. In summary, a total of 45 source-target dataset pairs were generated with each pair having 4500 landmarks for parameterizing the formulation.

For DIR, we employed an in-house developed GPU-based optical flow based registration procedure, which has been previously validated. The registration parameters for the optical flow (smoothness, number of iterations, warps) was systematically varied and the registration was performed in order to characterize the DIR accuracy domain.

Equation 1 (below) shows the proposed cost function, where *I* is the image similarity metric, *m* and *n* are CF variables to be optimized for each similarity metric, and *f* is a weighting factor between 0 and 1. Ideally, X = 0, Y = 1, and R = 1. Initial work focused on normalized mutual information, but additional metrics could easily be added in the future.

$$R = f(1-X)^m - (1-f)Y^n \; ; X = |I_{ST} - I_{SW}| \; , Y = I_{TW}$$

Four registration parameters were systematically sampled to fill a dense parameter space with DIR produced DVFs and known TREs. Initial tests showed that calculating a single TRE and CFR value for the entire 3D data volume produced poor results. However, targeting specific structures such as the PTV or parotids showed good correlation between the CFR and TRE.

During Q3 of Y1, we discovered that a limitation in the recognition and characterization of diseased liver tissue is that a clinical detection is not followed by an assessment of its mechanical properties

in an in-vivo manner. Reports have suggested that diagnostic discrimination of tissue malignancy may be possible using tissue stiffness as a metric, as malignant lesions exhibit considerable higher elasticity than the surrounding normal tissue.

Elastography is a non-invasive way to image the local elastic properties of soft tissue. Liver elastography has many clinical benefits, including the ability to discriminate between healthy and diseased tissue, visualize liver tissue changes during a clinical intervention, and detect pathological changes within the liver. Current elastography techniques involve applying low frequency oscillation to tissue and measuring the resulting deformation with US, extracting elasticity from the observed motion. Another technique, magnetic resonance elastography (MRE), uses synchronized cyclic shear wave displacement, encoded into the phase of the MR signal, to derive the elastic properties of tissue. Despite the usefulness of image-based elastography and its proven diagnostic accuracy in the thyroid, breast, and prostate, it has not yet been thoroughly investigated in the liver particularly within the modeling and simulation context, where the usage of multiple imaging modalities also raises the need to precisely register the multi-modal data, a problem has not been fully addressed so far.

Knowledge of biomechanical properties would also be useful for physics-based biomechanical modeling applications. Biomechanical tissue deformation modeling has been investigated by peers in many biomedical applications related to lung disease diagnosis and cancer treatment planning. Sophisticated biomechanical models can use material properties of soft tissue to correctly predict outcome and response to tissue interaction, calculate mechanical deformation of surrounding tissue caused by tumor growth, and accurately model tissue movement during radiation therapy treatments. For instance, tissue motion due to lung deformation can hamper the accuracy of brachytherapy seed implantation, and compensating for tumor motion caused by such tissue deformation requires tissue biomechanical modeling. By taking the mechanical effects of lung enforced liver deformation into account during the biomechanical simulation, respiratory liver motion can be estimated in real time. Describing respiratory-induced liver deformation can help in modeling and simulation techniques.

The focus of our research is to formulate a method to perform high-precision image-based liver elastography using patient-specific 4DCT data acquired during radiotherapy treatment planning, and to systematically validate and quantify the accuracy of this methodology. A linear elastic biomechanical model, which has been previously used for representing head and neck (Neylon, Qi et al. 2015) and breast (Hasse, Neylon et al. 2016) deformations, will be employed as a deformation model to represent the lung anatomy. Each mass element of the biomechanical simulation represents a corresponding voxel of tissue from the source image of the 4DCT data. Lung surface displacements were applied as boundary constraints for the model-guided liver tissue elastography, while the inner voxels were allowed to deform according to the linear elastic forces within the model. A novel biomechanically-based anisotropic convergence magnification technique was applied to the inner voxel in order to amplify the subtleties of the interior deformation. The inverse elasticity problem is solved by implementing a gradient-based search algorithm. Fig 1a shows the lung and liver anatomy at the start of the breathing cycle. The registered liver anatomy at the middle of the breathing cycle is shown in 1b while 1c shows the lung and liver anatomy simulated by the image-based liver model.

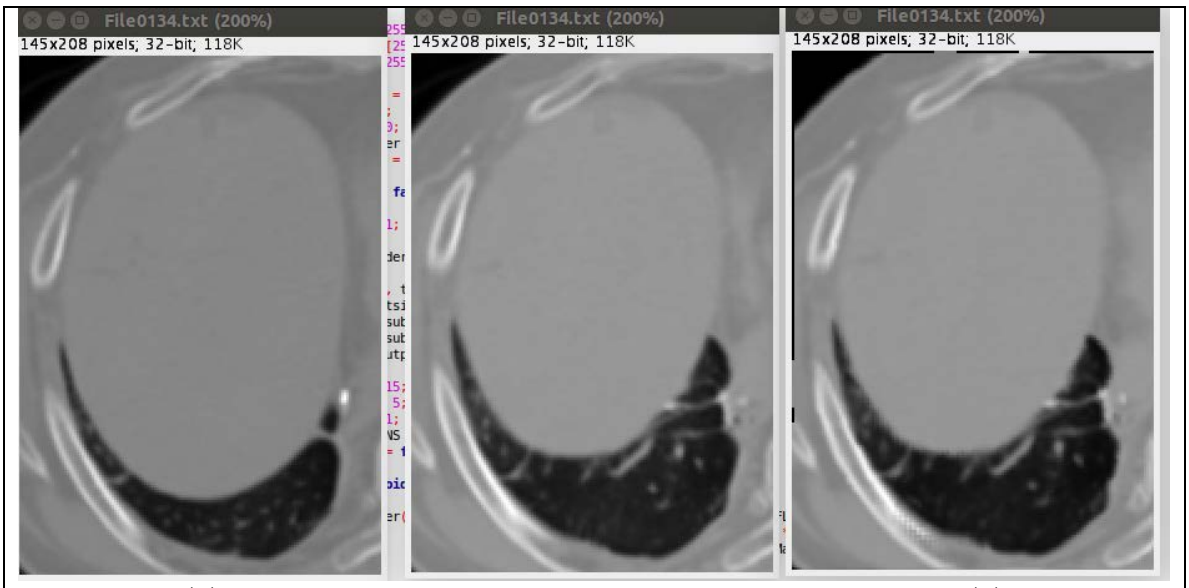

(a) Shows the lung and liver anatomy at the start of the breathing cycle. The registered liver anatomy at the middle of the breathing cycle is shown in (b) while (c) shows the lung and liver anatomy simulated by the image-based liver model.

During Q4 of Y1, we have instituted a liver elastography approach that will allow us to estimate tissue elasticity using conventional 4D imaging that is typically employed for deformable organs such as the lung. Conventional approach using MATLAB based solvers that typically employ a CPU based computing environment will not be able to address the computational complexity. Using a GPU based framework developed ground-up enables us to perform the elastography within 1 hour of computing time.

During Q1 of Y2, the overall goal is to develop a liver elastography framework using 4DCT and 4D MR based imaging paradigm coupled with the hyperelastic liver tissue modeling. For this quarter, we intend to develop an in-house codebase that will enable doing the same.

Model guided liver elastography framework: The focus of our research is to formulate a method to perform high-precision image-based liver elastography using patient-specific 4DCT data acquired during radiotherapy treatment planning, and to systematically validate and quantify the accuracy of this methodology. A linear elastic biomechanical model, which has been previously used for representing head and neck (Neylon, Qi et al. 2015) and breast (Hasse, Neylon et al. 2016) deformations, will be employed as a deformation model to represent the lung anatomy. Each mass element of the biomechanical simulation represents a corresponding voxel of tissue from the source image of the 4DCT data. Lung surface displacements were applied as boundary constraints for the model-guided liver tissue elastography, while the inner voxels were allowed to deform according to the linear elastic forces within the model. A novel biomechanically-based anisotropic convergence magnification technique was applied to the inner voxel in order to amplify the subtleties of the

interior deformation. The inverse elasticity problem is solved by implementing a gradient-based search algorithm.

Background: Elastography is a non-invasive way to image the local elastic properties of soft tissue. Liver elastography has many clinical benefits, including the ability to discriminate between healthy and diseased tissue, visualize liver tissue changes during a clinical intervention, and detect pathological changes within the liver. Current elastography techniques involve applying low frequency oscillation to tissue and measuring the resulting deformation with US, extracting elasticity from the observed motion. Another technique, magnetic resonance elastography (MRE), uses synchronized cyclic shear wave displacement, encoded into the phase of the MR signal, to derive the elastic properties of tissue. Despite the usefulness of image-based elastography and its proven diagnostic accuracy in the thyroid, breast, and prostate, it has not yet been thoroughly investigated in the liver, particularly within the modeling and simulation context, where the usage of multiple imaging modalities also raises the need to precisely register the multi-modal data, a problem has not been fully addressed so far.

In-house codebase development: As part of the grant, we have instantiated a liver elastography approach which will enable the liver tissue elasticity to be estimated using conventional 4D imaging that is typically employed for deformable organs such as the lung. Conventional approach using MATLAB based solvers that typically employ a CPU based computing environment will not be able to address the computational complexity. Using a GPU based framework developed ground-up enables us to perform the elastography within 1 hour of computing time.

Iterative hyperelastic value determination: To move from the initial estimates developed in §C.2.2.3 to the final estimates, we will employ forward model-guided elastography, where the forward model (Finite Element) will be employed to generate deformations using the previously estimated hyperelastic properties. The hyperelasticity will be iteratively optimized until a preset convergence is achieved. During the deformation phase, the outer lung surfaces will be constrained based on their deformable image registration displacements (SA1) while the inner lung voxels will be allowed to deform using their transient hyperelasticity. At steady state deformation, a unidirectional perturbation force will be applied to the inner voxels in order to amplify their convergence. The optimization of the estimated hyperelastic values will be performed using gradient descent and fast simulated annealing, which are well suited for hyperelasticity estimations. The desired hyperelastic properties *R* will be determined using the relation,

$$R = argmin\|D - R \otimes F\| + B\sqrt{|\nabla f^2|} + \varepsilon \qquad (1)$$

where *D* represents the lung deformation (SA1), *F* the applied force, and *B* is a regularization parameter. The deformation operator will consist of the eigenvalues of the 2nd Piola-Kirchoff stress tensor's inverse. In vector form, *D* is expressed as a convolution of *F* and *R* (Equation 4).

Because the hyperelasticity is numerically described as a sequence of parameters, optimizing the hyperelasticity is a multi-local minima problem. To address this issue, a fast-simulated annealing algorithm will be used to optimize the hyperelasticity simultaneous to a regularization, similarly to our previously published application in the breast.

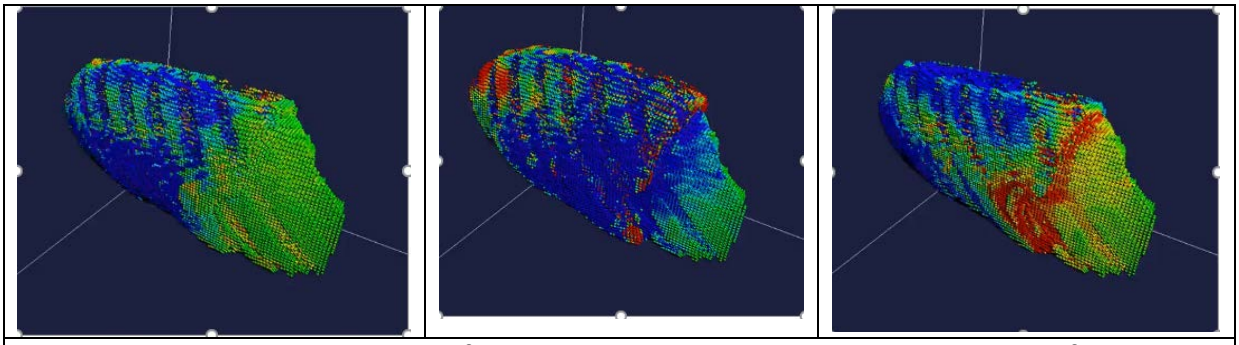

Fig 1. Lung and liver model setup for elasticity estimation. Fig a shows the start of lung inhalation (tightening colored in blue). (b) shows the end of the inhalation where the liver constriction is caused by the expansion fo the lung. (c) shows the end of exhalation where the liver expansion is caused by the contraction of the overall lung.

Deformation setup: A physics-based biomechanical model of the lung and liver was used as a forward model to solve the inverse elasticity problem. The forward model focused on iteratively computing the liver tissue deformation for a given lung surface displacement for a given liver elasticity distribution. Fig 1 shows the deformation interaction between the lung and liver. For our research, we consider the lung models as the boundary constraint for the liver elastography estimation.

Preliminary results using synthetic lung phantoms: We published a systematic analysis of a linear version of the elasticity estimation process using synthetic lung phantoms, normal and emphysemic lung, with and without embedded lung tumors, enabling us to test the algorithms using ground-truth tissue elasticity and lung deformations. Fig 2 presents the results. Employing 18 synthetic lung phantoms, our results showed that 99.98% (right lung) and 99.92% (left lung) of the voxels converged with an average of within 0.5 mm of the ground-truth displacement values, which resulted in 91.59% (right lung) and 91.87% (left lung) of the voxels converging within 1 kPa of the ground-truth elasticity. Figure 4 shows the linear elasticity estimate for a normal lung. Figure 4b shows the estimation errors were less than ~0.8 KPa. While these results employed linear elasticity, they indicate feasibility of the more general hyperelastic approach. The simulations of emphysemic lung and lung tumors also showed good agreement with the estimated and ground truth elasticity. Emphysema lowers the elastic modulus of normal tissue, and malignant tumors generally have a greater elasticity than surrounding tissue. On average, the methodology converged with displacement accuracy values of 99.95%, 99.94%, and 99.95% for simulated emphysematous, cancerous, and normal tissues respectively, corresponding to 91.90%, 91.68%, and 91.62% of voxels converging within 1 kPa of the ground-truth elasticity values.

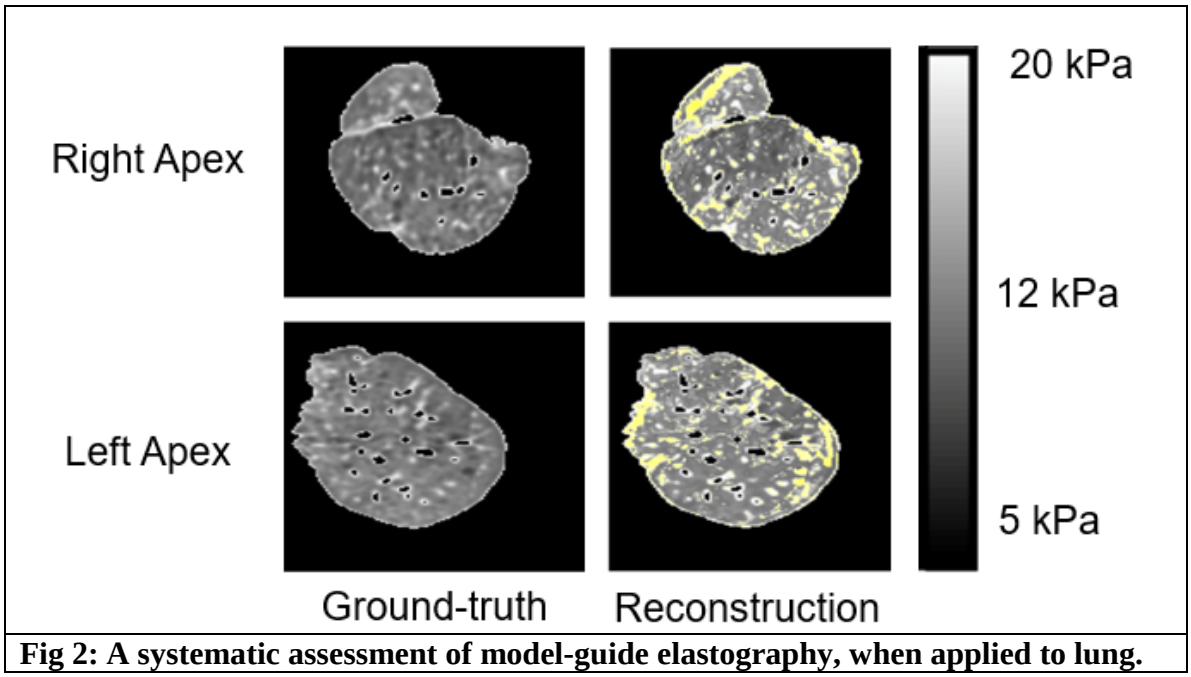

Fig 2: A systematic assessment of model-guide elastography, when applied to lung.

During Q2 of Y2, we studied our preliminary results using human patient data.

Preliminary results using human patient data: We estimated the linear elasticity for human patient datasets using the methodology discussed above. We employed both non-COPD and COPD patient lung datasets for our study. Figure 1 shows the elasticity estimation results for a non-COPD patient. The elasticity estimated from the lung deformation (figure 1a) is shown in figure 1b. Figure 2 shows the elasticity estimation results for two severe COPD lung patients. The elasticity estimated from the lung deformations (figures 2a and 2c) are shown in figures 2b and 2d. Much of these lungs have elasticity (0-2 KPa) consistent with COPD lung tissues. The difference between COPD and normal lung tissues are clear in these examples and are consistent with expected values. We conducted the elastography estimation on 13 lung cancer patients, 7 of which had COPD and the remaining had otherwise normal lungs, using images reconstructed at peak inhalation and exhalation using the techniques of Low et al [47]. These datasets simulate breath-hold at these breathing phases, avoiding the added complexity of dynamic breathing, which will be modeled in SA3. Figure 7 shows the average elasticity for voxels with HU values of -600 to -800, representing parenchymal tissues, for the 13 patients, ranked in order of average elasticity. As expected, the mean elasticity values of the COPD patients were consistently lower than the non-COPD patients. These data indicate that we are able to differentiate between COPD and non-COPD patients. We anticipate that by directly utilizing the FHFBCT images and employing hyperelastic property estimation, we will be able to provide data that investigators will be able to use to make subtler differentiations, such as those needed to evaluate treatment efficacy.

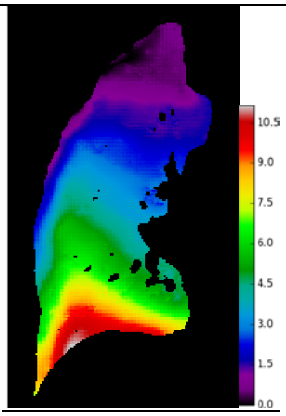

(a)

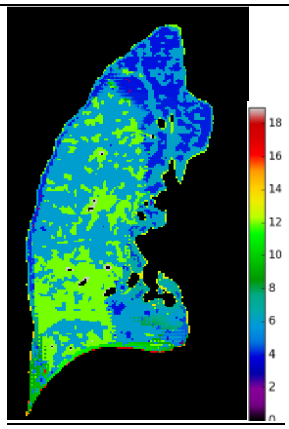

(b)

Fig 1. 2D slice view of the deformation magnitude (in mm) for a non-COPD lung (a) is shown. The corresponding 2D slice view of the estimated elasticity (in KPa) is shown in (b).

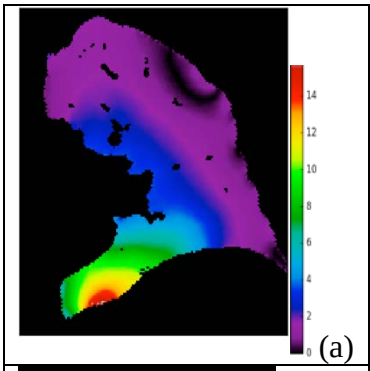

(a)

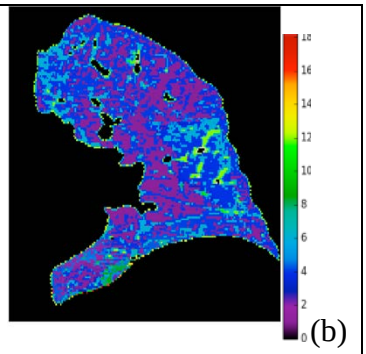

(b)

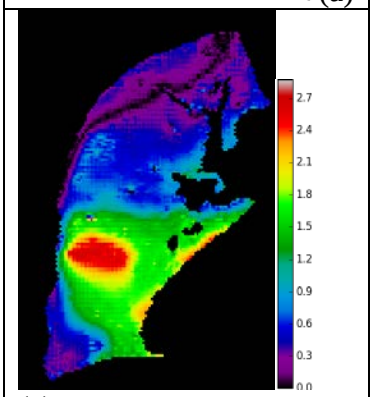

(c)

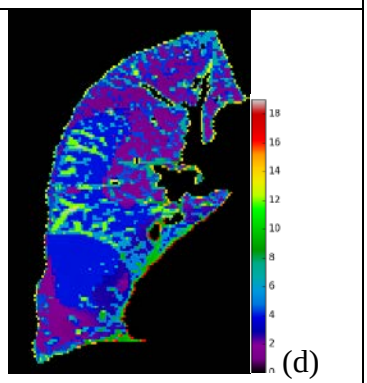

(d)

Fig 2. 2D slice view of the deformation magnitude (in mm) for two COPD lung patients is shown in (a) and (c). The corresponding 2D slice view of the elasticity (in KPa) is shown in (b) and (d).

Elastography validation techniques: We will validate the elastography techniques using the technique by Low et al [47] to model human breathing motion. This technique uses free-breathing CT scans and a breathing motion model to create CT datasets at any breathing phase. Because SA2 involves only biomechanical property estimation and not airflow dynamics, we will create breath-hold CT scans for validating SA2. FHFBCT scans will be employed to test the full FSI model.

(a) The elasticity estimates will be validated by employing them to predict the tissue deformations and comparing the predicted deformations to the actual deformations of the breath-hold CT scans using techniques we have described when validating elasticity estimates of the head and neck and breast. We conducted this analysis with the patient data shown in Figures 5 and 6, and our observations showed that for both datasets, 95% of the voxels demonstrated <10% displacement error.

(b) We will determine if the linear elastic components of our estimated tissue elasticity values agree with published data.

(c) Elasticity properties are independent of the breathing state, and so should be our estimated properties. We will systematically exclude one or more lung geometries at specific breathing phases and re-compute the elastic properties. The property values should be the same regardless of which breathing phases are excluded; variations will indicate errors in our approach.

The primary outcome will be a voxel-by-voxel description of tissue hyperelasticity. To date, such subject-specific hyperelastic properties have not been available and will be the key contribution of the proposed work.

During Q3 of Y2, we present a novel methodology for performing lung elastography within the radiotherapy context. Our approach employed a physics-based model and a novel convergence magnification approach to estimate the lung elasticity distribution. For a systematic analysis, we employed a physics-based virtual lung phantom with CT source geometry and a heterogeneous voxel-to-voxel elasticity distribution. A set of 18 synthetic CT image datasets with known ground-truth elasticity representing normal, emphysematous, and tumor tissue within the lungs was generated and used as input for the lung elastography. During the lung elastography, we start by re-estimating the lung deformations using a deformable image registration procedure. For known phantom geometry, boundary conditions and lung deformation, we solve for the elasticity distribution by iteratively optimizing the tissue elasticity and deforming the lung model for given boundary constraints. To improve the estimation accuracy, a convergence magnification approach was formulated using a physics-based process that amplified the geometrical differences between the ground-truth and the deformed geometry. Our results showed that the model-guided approach estimated the elasticity with $91.94 \pm 5.20\%$ of voxels within 0.5 mm of ground-truth displacement and 1 kPa of the ground-truth elasticity. The novel convergence technique presented in this paper improved the accuracy of the estimated elasticity from 77.05% to 91.94%. In the systematic analysis, variations in forward model, ground-truth elasticity distribution, boundary deformation, and geometry were investigated with respect to their effect on the accuracy of the elasticity estimation technique.

Assessing the estimation accuracy for variations in the ground-truth elastic distributions: Table 2 lists the average results for the systematic analysis performed using the locally heterogeneous convergence magnification method. The results were also broken down by experimental category; these results are further explained in sections 4.3 – 4.4 below. Three different ground-truth elasticity distributions—emphysematous, cancerous, and normal tissue—were investigated to analyze the robustness of our methodology. On average, the methodology converged with displacement accuracy values of 99.95%, 99.94%, and 99.95% for emphysematous, cancerous, and normal tissue respectively. These results, presented in table 2 above, corresponded to 91.90%, 91.68%, and 91.62% of voxels converging within 1 kPa of the ground-truth elasticity values. Figure 9 illustrates the robustness of the methodology for reproducing different ground-truth elasticity distributions. Figure 9(a) shows the conventional elasticity reconstruction, which was the same for normal, emphysematous, and cancerous ground-truth elasticity distributions. Discrepancies between the reconstruction and the normal ground-truth elastic distribution that are greater than 1 kPa are highlighted in yellow. It can be seen that initially, the reconstruction is very different from the ground-truth, with a similarity of less than 50%.

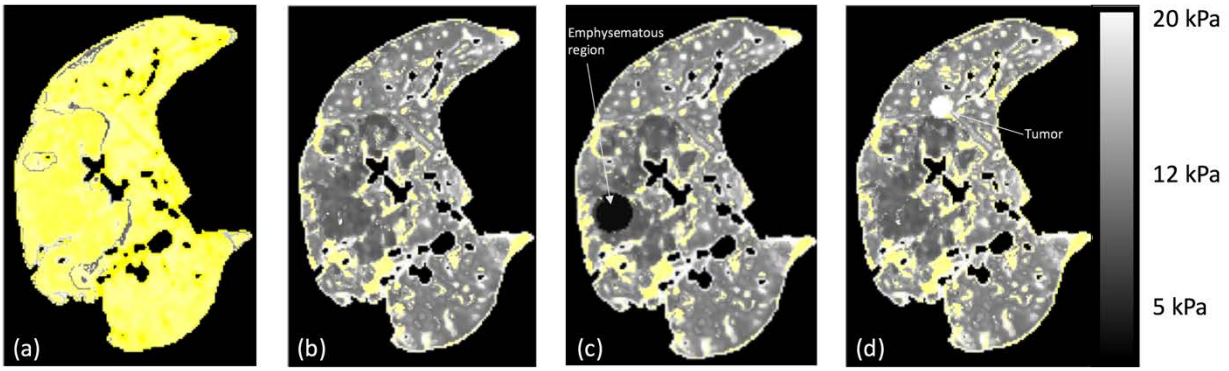

Figure 1. 2-D slice of middle right lung. (a) shows the conventional reconstruction for all 3 ground-truth elasticity distributions. (b) shows the novel reconstruction for normal tissue, (c) shows the reconstruction for normal tissue with emphysematous region, and (d) shows the reconstruction for normal tissue with tumor. Discrepancies (error > 1 kPa) between the reconstructed and ground-truth distributions are highlighted in yellow.

Figure 1(b – d) show the novel elasticity reconstruction for normal, emphysematous, and cancerous tissue respectively, with the discrepancies (error > 1 kPa) between the reconstructed and ground-truth data highlighted in yellow. With similarity values of 92.73%, 93.44%, and 91.10%, it can be seen that use of the locally heterogeneous convergence magnification greatly improves the elasticity reconstruction, allowing for the visualization of emphysematous and cancerous regions within the lungs. It should be noted that for each lung geometry, cancerous and emphysematous regions were placed at different locations within the 2-D slices to ensure that the regions could be localized regardless of position. A two-sample t-test was performed between the mean values of 18 different emphysematous, 18 different cancerous, and 18 normal tissue distributions, and the observed difference was convincing enough to say that the average values of each ground-truth elasticity distribution did not differ significantly ($P > 0.05$).

Assessing the estimation accuracy for variations in the boundary constraints: As described in section 3.2.4 above, the outward motion of the lung boundary was constrained to three different values for each section of the lung as listed in table 1. The resulting displacement and elasticity accuracy values of the methodology are listed in table 4 below.

Table 1. Displacement and elasticity accuracy values for different geometries and boundary constraints.

Lung Geometry - Boundary Constraint	Displacement Accuracy < 0.5 mm (%)	Elasticity Accuracy < 1 kPa (%)
Apex – 2 mm	99.99	97.89
Apex – 4 mm	99.99	97.55
Apex – 6 mm	99.97	96.82
Middle – 3 mm	99.92	94.17
Middle – 6 mm	99.94	92.18
Middle – 9 mm	99.95	90.07
Base – 10 mm	99.98	89.37

Base – 13 mm	99.99	82.86
Base – 16 mm	99.78	84.80

Overall averages are listed for the three different boundary constraints in table 2 above. A two-sample t-test was performed on these values, and it was found that there were no significant differences between the results regardless of whether boundary constraint 1, 2, or 3 was used for each geometry.

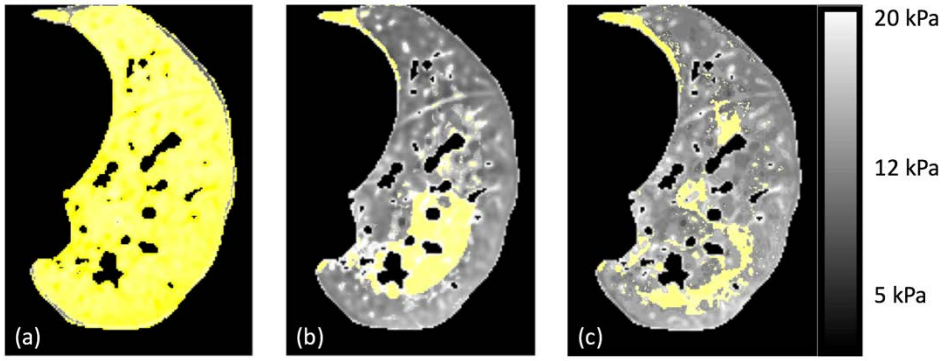

Figure 2. 2-D elasticity reconstruction of base of left lung. (a) shows conventional reconstruction, (b) shows novel reconstruction with 10-mm boundary constraint, and (c) shows novel reconstruction with 16-mm boundary constraint. Discrepancies (error > 1 kPa) between the reconstructed and ground-truth distributions are highlighted in yellow.

Figure 2 further illustrates that the reconstruction converges similarly regardless of the boundary constraint magnitude. Figure 10(a) shows the conventional reconstruction of the base of the left lung, (b) shows the reconstruction when a 10-mm boundary constraint was applied, and (c) shows the reconstruction when a 16-mm boundary constraint was applied. Figure 2(a) is over 50% different than the ground-truth, while 2(b) and 2(c) are only 6.07% and 6.34% different from the ground-truth respectively. The result supports the accuracy in estimating the lung elasticity for varying boundary constraints.

In summary, our elasticity estimation converged with about 99% sub-millimeter accuracy, resulting in an elastic convergence of about 92%. We have shown that the use of the locally heterogeneous convergence magnification approach is necessary in the transition to apply our conventional elastography technique to lung anatomy. However, use of different ground-truth elasticity distributions and different boundary constraint magnitudes did not affect the convergence of our technique. While we mainly focus on ground-truth values obtained from an elastodynamic forward model, “noisy” and elastostatic forward models also produced reliable elasticity estimations.

During Q4 of Y2, our work is summed up below.

Objectives: Liver diseases, such as liver cancer and cirrhosis, are commonly associated with changes in the biomechanical properties of liver tissue. Functional imaging techniques such as elastography have shown great promise in measuring the biomechanical properties of liver tissue; however, current liver elastography techniques require additional equipment that is not available within the radiotherapy setup. We present a novel methodology for estimating liver elasticity

derived from deformation observed during 4DMR ViewRay (MRIdian System™, ViewRay™, Cleveland, OH, USA) scans within a radiotherapy setup.

Methods: Phase 1 and phase 8 datasets, categorized by diaphragm position, were deformably registered. The resulting displacement maps were considered ground-truth. A GPU-based biomechanical model was then assembled from the segmented phase 8 liver dataset and, along with patient-specific boundary constraints, used to iteratively solve for the liver elasticity distribution. The liver elastography process was performed for 11 4DMR patients.

Results: Maximum liver deformation was observed to be between 3.99 and 9.04 mm. On average, 95% convergence within 1 mm was observed. A validation study using phase 4 liver datasets illustrated an accuracy of 86%. Normalized cross-correlation quantified high similarity between the results of the estimation and validation studies with their respective ground-truths.

Conclusions: Overall, the results suggest that liver elasticity can be measured with approximately 95% convergence using 4DMR scans acquired within the radiotherapy workflow.

Advances in knowledge: These results indicate the potential for performing liver elastography within the radiotherapy setup without the need for additional equipment, which can lead to improved tissue-sparing radiotherapy treatment plans and more precise monitoring of treatment response.

Hepatocellular carcinoma (HCC) is one of the most common malignancies, and the third most common cause of cancer-related death worldwide.[1, 2] Surgical resection and liver transplantation are the primary treatment methodologies, however strict criteria limit the pool of eligible patients for both cases. HCC has a poor prognoses, with a 5-year survival rate of less than 12% due to a combination of late diagnosis and lack of efficient therapies for advanced stages.[3] Stereotactic body radiotherapy (SBRT) has been used to treat patients with HCC who are not eligible for other treatments.[4] SBRT uses advances in imaging and conformal radiotherapy to deliver ablative, high dose radiation in order to optimize local control. Radiation-induced liver disease (RILD) is a significant limiting factor in the use of SBRT because there are no effective treatments or predictors.[2] Most patients with HCC have pre-existing cirrhosis or hepatitis, which may significantly increase their risk of RILD.[5] Baseline liver function is thought to be the most important factor associated with risk of RILD.[1] Pre-treatment visualization of liver function in vivo is necessary in order to expand the use of SBRT for HCC.

The liver plays a role in metabolism, synthesis, secretion, immunity, and many other functions.[6] Liver disease, including cirrhosis, fibrosis and tumors, can disrupt the functions of the liver by altering the biomechanical properties of the tissue, most notably by changing the tissue stiffness.[7, 8] Clinically, elastography provides a measurement of liver stiffness and is a predictor for HCC.[9] Magnetic resonance elastography (MRE) can noninvasively and quantitatively assess the elasticity characteristics of soft tissue.[7] Liver stiffness measured by MRE has been shown to correlate well with histologic staging of fibrosis and differentiation of benign and malignant liver lesions.[10] However, current MRE techniques require equipment that is not typically available within a conventional radiotherapy setup.

Recently, an MR guided radiation therapy (MRgRT) system (MRIdian System™, ViewRay™, Cleveland, OH, USA) was introduced in the field of radiotherapy (RT).[11] The ViewRay system integrates a 0.35T MRI and 3 Cobalt sources, which allows for simultaneous MRI acquisition and treatment delivery for a variety of malignancies.[12] The superior soft tissue contrast from ViewRay's on-board MRI enables soft tissue based gated RT and also provides an effective way for on-line adaptive RT. Both techniques are especially helpful for treating thoracic and abdominal tumors by effectively accounting for intra-fractional and inter-fractional motion. In addition, a 4DMRI sequence on the 0.35T magnet on ViewRay was recently developed for motion characterization.[13] In this study, we present a novel elastography process for estimating liver tissue elasticity using 4DMRI to observe liver deformation in each respiratory cycle during patient treatment simulation. The rest of this paper is organized as follows: Section 2 introduces the methods employed for the deformable imaging registration, elasticity estimation, validation, and quantitative evaluation. Section 3 presents the qualitative and quantitative results of the deformable image registration, elastography, and validation processes. Section 4 presents a discussion of the results and highlights the areas for continued research, while section 5 concludes the paper.

Our elastography process focuses on estimating the effective Young's modulus for each voxel of liver tissue using 4DMR liver data. Figure 1 shows a flow chart summarizing the elasticity estimation. First, phase 1 and phase 8 datasets from the 4DMR liver images were registered using an optical flow deformable image registration (DIR) algorithm.[14] Liver deformation vectors (DVFs) were obtained for every voxel of liver tissue. The biomechanical model was then assembled using segmented phase 1 liver geometry and a randomly initialized elasticity distribution. Using the ground-truth liver DVFs, the elasticity distribution was optimized. The inverse elasticity problem was formulated as a parameter-optimization problem with an objective to determine the elasticity parameter that would minimize the difference between the ground-truth deformation and the deformation computed by a biomechanical model. The biomechanical model and inverse elasticity estimation was implemented on a GPU cluster, which allowed the elasticity estimation for each patient dataset to converge in around 2 hours. Spatial elasticity and displacement error distributions were then obtained and validated.

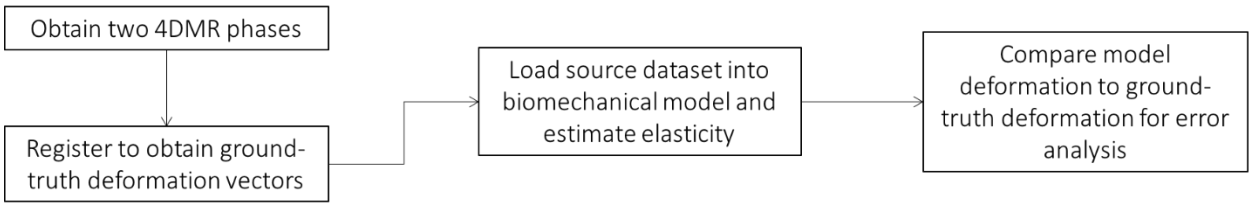

Figure 1. Flow chart describing the liver elastography process. Two 4DMR liver phases are registered and ground-truth deformation vectors are obtained. A biomechanical model is used to obtain an optimal elasticity estimation and error analysis.

In this section, we first briefly present the 4DMR acquisition process and the DIR technique used to obtain the ground-truth DVF. Next, we present the constitutive model and convergence criteria used for the elasticity estimation process. We then describe a technique that was used to validate the estimated elasticity. We conclude the section with a discussion of the metrics used to evaluate the quantitative accuracy of the elasticity estimation and validation results.

The study was approved by our institutional review board and each patient provided written informed consent. Eleven patients with tumors in the liver treated on ViewRay were included in our study. The MRI study was performed immediately after high resolution 3D MRI simulation acquisition. The 4DMRI sequence parameters are: TE/TR=3.0/6.0ms; bandwidth=400Hz/pixel; FA=110°, field-of-view=500x350x200mm, resolution=1.3x1.3x1.8mm^3, acquisition time = 7min. No specific breathing instruction was given to the subjects during the MRI exam.

The model-guided elasticity approach presented in this paper relies on displacement values extracted from DIR of 4DMR datasets. 4DMR datasets were acquired from 4DMR ViewRay (MRIdian System™, ViewRay™, Cleveland, OH, USA) scans taken within a radiotherapy setup. The 4DMR datasets were separated into phases according to diaphragm position. The liver was segmented and phase 1, corresponding to end inspiration, and phase 8 datasets, corresponding to end expiration, were then deformably registered using a well-validated in-house multi-level optical flow DIR algorithm.[14] The resulting DVFs were taken to be the ground-truth displacement for the elasticity estimation process. For the rest of the paper, the phase 8 datasets will be considered the source images, the phase 1 datasets will be considered target images, and the phase 8 datasets deformed according the ground-truth displacement will be considered warped images.

The accuracy of the DIR results is necessary to ensure the validity of the ground-truth deformation data. Figure 2 illustrates an example of the DIR for a 2D-slice of 4DMR data. Figure 2(a) shows the source data (phase 8 dataset) in red overlain with the target (phase 1) data in green. Mismatches can be seen between the source and target, especially near the diaphragm and liver boundaries. Figure 2(b) shows the target data is red overlain with the warped source data in green. It can be seen that the registration accounts for the liver deformation well, with little mismatch seen between the target and warp images. The extent of the registration accuracy will be further quantified in Section 3.4.

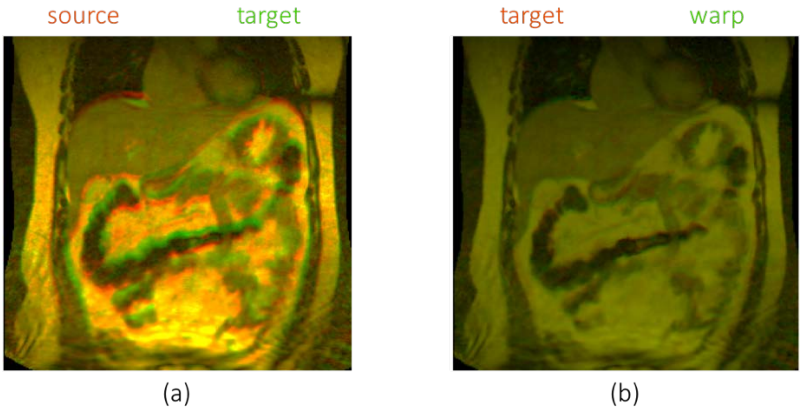

Figure 1: Example of the registration results achieved with our in-house optical flow algorithm. The source (red) and target (green)(a) were registered, resulting in the warped (green) image that is overlain with the target in (b).

During Q9, we worked on Code parallelization**.** The liver anatomy processing consists of a number of voxels representing the liver anatomy. Biomechanical modeling of the liver using the voxels require a streamlined usage of the graphical processing units. The computational complexity of the liver finite deformations was computed to be O(N M), where N represents the total number of liver

voxels and the M represents the total neighbors (26) for each of the N voxels. As N gets higher and higher, processing biomechanical liver deformations becomes a complex task. To this end, we developed a code streamline process, where we transferred the code to work in a GPU based setup. We designed and developed a novel winged-edge data structure that stores the voxel neighbors in a compact manner. The data structure works as follows: For each voxel, we have a set of 26 neighboring voxels which are needed to be processed. For each voxel, we first created a bigger volume box and placed all the voxels inside the box in a shared memory. For each voxel, the neighboring volume box is also redundantly kept in the shared memory. When processed, each voxel has a read-only shared memory access to all its neighboring voxels in a winged-edge data access manner. This enabled processing of the biomechanical liver data in a streamlined manner.

During Q10, we worked on Data analysis using noise-inherent data**.** Elastography has the potential to inform diffuse liver disease phenotype characterization and staging and treatment response monitoring. Elastography is a non-invasive method of mapping the distribution of a critical liver biomechanical property, elasticity, or tissue stiffness. In our preliminary work, we demonstrated a novel elastography approach using virtual phantoms. This methodology was quantified and validated for lung cancer radiation therapy CT scans reconstructed using a published breathing motion model.

Our elastography estimation method used multiple 4DMR scans, each delivering 3 T magnetic field to the liver. Our current technique delivers exposures similar to routine diagnostic MR studies at 0.35 Tesla. Diagnostic MR studies are used for human image interpretation while the scans acquired for elastography estimation are used to determine the motion and distortion characteristics of liver tissues during breathing. Therefore, we assessed elastography quality using simulated reduced MR scans.

In this study, low magnetic field scans were simulated using a noise injection process in order to determine the effect of noise on our liver elastography process. Simulated scans with tube current-time products representing various stages up to 0.5 T were investigated. The results of the baseline scans and low magnetic field simulated scans were not significantly different, indicating that low dose MR scans could produce reliable elastography results. Since the baseline scans were taken with 3 T and an effective equivalent CT dose of 1.2 mSv, this suggests that the effective dose could be reduced to about 1.5 T per scan while still obtaining useful elastographic information.

We foresee a few limitations to this study. Firstly, the noise injection code assumed no tube current modulation, which is not typically employed in radiation therapy but is often employed for diagnostic purposes. The algorithms to select tube current modulation are proprietary and depend on the capability of the x-ray generator, which place limits on the slew rate of the tube current. The lack of modulation creates increased noise at the top or bottom of the image as the shoulders or abdomen starts to appear. However, as the parenchymal tissue is located near the center of the image on the chest MR, we believe these artifacts did not affect the parenchymal registration process. Secondly, the quality of the elastography results depend on the quality of the deformable image registration, which is affected by the addition of noise. There is a need to investigate registration algorithms that are more robust to high imaging noise, which will be addressed in future work. Thirdly, we employed image domain-based noise injection which is not as accurate as noise injection in the raw data domain. As shown in the Appendix, the image domain-based noise

injection generated results that closely match experimental data. Future work will focus on extending the noise injection technique to the raw data domain, and performing more water tank scans to ensure the accuracy of the results.

During Q11, we worked on Elasticity Optimization**.** Variations in the elasticity estimation optimization may lead to variations in the estimated liver tissue elasticity. To systematically study this phenomenon, we implemented 4 different optimization algorithms, (a) gradient descent optimization, (b) ADAM optimization and (c) particle swarm optimization. Gradient descent optimization focused on following the gradients of the deformation accuracy until the minimum accuracy was achieved. ADAM optimizer focused on optimizing the elasticity based on the minimization of the moments. Finally, the Particle swarm optimization was employed as a way to address a multi-local minima optimization, where multiple elasticity distributions may provide the same deformation pattern observed in the 4DMR images. Our study showed that using the ADAM optimizer we were able to estimate the linear elasticity distribution consistently.

During Q12, we worked on Extension to hyperelasticity**.** We formulate hyperelasticity using a generalized Ogden material model, which defines a strain energy, *W*, in terms of principal stretches, λ_i, and a shear modulus, μ:

$$W = \sum_{p=1}^{N} \frac{\mu_p}{\alpha_p}\left(\lambda_1^{\alpha_p} + \lambda_2^{\alpha_p} + \lambda_3^{\alpha_p} - 3\right); where\ 2\mu = \sum_{p=1}^{N} \mu_p \alpha_p$$

where α_p is the hyperelastic model power term for parameter *p* of *N* parameter. The principal stretches were determined by solving for the image deformation tensor field eigenvectors. We employed the Ogden material model to experiment with a physically realistic range of strain-energy functions. The principal Cauchy stresses, σ_i, were determined from the 2nd Piola-Kirchoff stress tensor, which were itself be derived from the partial derivative of the strain energy *W* with respect to the principal stretches.

$$\sigma_i = \lambda_i \tau_i = 2\lambda_i \frac{\partial W}{\partial \lambda_i} = \sum_{p=1}^{N} \mu_p \lambda_i^{\alpha_p}$$

Typical implementations of the Ogden material model employ a hydrostatic pressure term, which we will not need due to the relative incompressibility of the tissues. The internal force vectors were computed from the principal Cauchy stress at each element, enabling update of the velocity, assuming near-linearity for small time increments. Although implementation is relatively straightforward, the methodology is much more computationally intensive than typical linear Hookean material models. In order to maintain performance at interactive speeds, we implement the Ogden material model on a multiple GPU framework employing an in-house compute cluster that we have previously employed for real-time radiotherapy calculations.

3.C.2.2 Elasticity estimation: The Ogden model data inputs are: the FHFBCT images and associated deformation vector fields (SA1), pressure transducer-measured intraoral pressure, spirometer-measured airflow, abdominal strain-gauge belt measurements to provide initial estimates

of the forces (as boundary conditions) within the livers, and ECG to relate heart induced liver tissue motion to cardiac phase. Estimating the hyperelasticity associated with each liver voxel is a mathematically complex problem, mostly attributed to the size of hyperelasticity parameter search space and the fact that the hyperelasticity values may be degenerate, leading to multiple solutions for the same deformations. To this end, we employ the following two-step process to reduce the parameter search space and solve for the global minimum:

Step 1: Compute the initial hyperelasticity properties using a pseudo-direct hyperelasticity estimation procedure employing a Green's function model and physics-based airflow distribution.

Step 2: Refine the hyperelasticity properties employing a hyperelastic finite element deformation model that deforms the liver geometry for known actuation parameters (pressure at the mouth, spirometry measurements) and the hyperelasticity distribution estimated in step 1.

3.C.2.3 Initial hyperelasticity estimation: A pseudo-direct hyperelastic property estimation reduced the optimization process to a workable search. We associate with each voxel a deformation operator, which is a vector of numerical values representing the hyperelastic properties of the voxel's local neighborhood, separating the deformation operator estimations into voxels at the liver surface and inside the liver.
Estimation of Linear Elasticity of liver surface voxel: We first estimate the effective Young's Modulus, a linear elastic parameter associated with each liver surface voxel, employing our approach discussed in Santhanam et al 2008 [21]. In that approach, the effective Young's Modulus is represented as a linear combination of steady state structural and functional parameters. The former is related to the location of the voxel, and the latter is directly related to the voxel deformation computed from the registration process. The functional parameters were solved using an inverse deformation analysis employing the known 3D displacements and applied forces approximated from the spirometry and strain gauge belt measurements.

Estimation of Volumetric Deformation Operator of Internal Liver Voxel: For the voxels inside the liver, we employ a Green's function representation for the Ogden material model (Equation 3). The Green's function deformation operator takes as input the force applied on the voxels inside the liver and computes the subsequent steady state change in shape. Without further modifications, the formulation would be ill posed, so we employ two mathematical modifications to make the problem well posed. We first employ a Hyper Spherical Harmonic transformation to re-formulate the Ogden material model in that domain. This transformation converts the formulation into a well-posed formulation for homogeneous hyperelastic solvers, but the heterogeneous hyperelasticity distribution requires the addition of the boundary element constraints, which is in turn computed from the functional parameter of liver surface voxels. The transformation was be used to compute the initial hyperelastic properties for the known values applied force and volumetric liver displacement.

We published a linear elasticity application of this technique, showing the feasibility of the proposed process to provide the initial elasticity estimation.

Iterative hyperelastic value determination: To move from the initial elasticity estimates to the final estimates, we employ forward model-guided elastography, where the forward model (Finite

Element) was employed to generate deformations using the previously estimated hyperelastic properties. The hyperelasticity is iteratively optimized until a preset convergence is achieved. During the deformation phase, the outer liver surfaces was be constrained based on their deformable image registration displacements (SA1) while the inner liver voxels was allowed to deform using their transient hyperelasticity. At steady state deformation, a unidirectional perturbation force was applied to the inner voxels in order to amplify their convergence. The optimization of the estimated hyperelastic values was performed using gradient descent and fast simulated annealing, which are well suited for hyperelasticity estimations. The desired hyperelastic properties *R* is determined using the relation,

$$R = argmin\|D - R \otimes F\| + B\sqrt{|\nabla f^2|} + \varepsilon$$

where *D* represents the liver deformation (SA1), *F* the applied force, and *B* is a regularization parameter. The deformation operator consists of the eigenvalues of the 2nd Piola-Kirchoff stress tensor's inverse. In vector form, the volumetric liver displacement is expressed as a convolution of the air force and the hyperelastic properties.

Because the hyperelasticity is numerically described as a sequence of parameters, optimizing the hyperelasticity is a multi-local minima problem. To address this issue, a fast-simulated annealing algorithm is used to optimize the hyperelasticity simultaneous to a regularization, similarly to our previously published application in the breast.

During Q13, we worked on GPU cluster-based implementation. Computing the hyperelastic parameters is a more complex problem than estimating the linear elastic parameters. To this end, we need to employ a multi-GPU computing setup for estimating the hyperelasticity. We developed an innovative parallelization algorithm that use a multitude of search directions for the hyperelastic parameters. A set of 52 GPUs were employed in this study to analyze the hyperelasticity of each liver anatomy. The ground-truth deformation was calculated from the 4DMR datasets using an optical flow based deformable registration algorithm. The computation time for this step was approximately 2 minutes. Once estimated, each of the GPUs were then loaded with the same patient dataset and ground truth deformations. A central GPU was assigned the task of integrating the search results and disseminating the results to the other GPUs. Each GPU was assigned the task of optimizing a single hyperelastic parameters at a given time step. At the end of 5 search iterations, the results were then transferred to single CPU that sorted the hyperelastic values based on the observed cost/error. The value with the minimum cost is set and the search process continued with that hyperelastic parameters as the starting point. The process continued until the search process yielded a consistent result. To avoid being captured inside a local minimum, fast simulated annealing was employed by each of the GPU. The process randomly shuffles the search parameter based on an exponentially converging probability value. Results, showed that we were able to converge quickly on the estimated elasticity values.

During Q14, we hypothesize that biomechanical modeling alone will be insufficient to characterize tissues for liver management. In future work, we will investigate the need to integrate tissue hyperelastic property estimation with blood modeling into an integrated model that will fully characterize the dynamic status of the patient's liver function. A critical component of this is the simultaneous automated vessel mapping using multiple FHFBCT scans. A goal of this aim is to

provide vessel maps (tracheobronchial and bronchiole tree) that include vessels with sub-voxel cross sections. This is made possible by the quantitative nature of CT and the acquisition of numerous free-breathing images.

Reference Geometry: We first define a reference geometry, likely the geometry of the first MR scan. The selection of the specific reference condition is somewhat arbitrary except that it has to have unique spatial morphology and be able to be tied to the breathing amplitude and ultimately to the airflow model. The first helical CT scan meets both of these criteria.

We propose to take advantage of the quantitative nature of CT coupled with the multiple scan acquisition to map small bronchi and bronchi at sub-voxel resolutions. The justification for this is shown in Figure 7, where a bronchus has a sub-voxel diameter, but its impact on the voxel intensity can be measured as it transitions between two voxels.

Density-based subvoxel blood-vessel mapping: The voxel resolution of the FHFBCT scans are 1 x 1 x 1 mm^3, which corresponds to the diameter of the 6-10th bronchial generation. Further generations, such as bronchioles have sub-voxel diameters and might be considered to be undetectable (Figure 8). However, even sub-voxel bronchioles have an impact on the voxel density measurement. As the blood vessel moves between voxels, its impact on the MR voxel density can be predicted and mapped if there is a blood vessel tree (BT) map to guide vessel mapping.

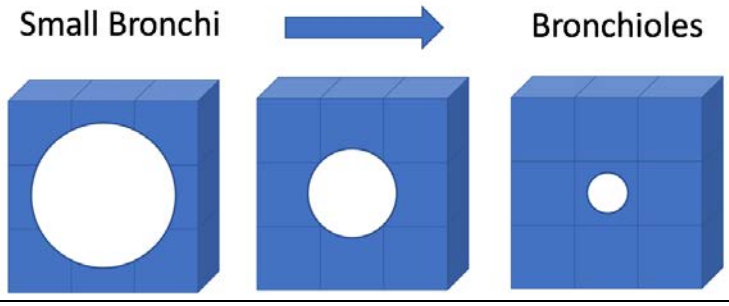

Fig 7. Schematic showing the partial volume averaging effect of imaging bronchi and bronchioles in CT.

Connectivity likelihood map using tubularity geometric features: Detecting the *potential* existence of a bronchus is insufficient to develop the vessel map. We also connect the BT using a technique we recently developed for imaging and tracking the small bowel. We propose to first generate a BT likelihood map over the imaged liver. Global geometric descriptors are challenging to identify the BT by themselves due to the variation of the BT shape between successive images. We propose to use both the global descriptor and density-based detection to characterize the chance of each pixel belonging to the BT. Our preliminary results of conducting this evaluation for the small bowel favored using a scale-optimized outward gradient flux, compared to alternatives such as Frangi or bi-Gaussian filter. Specifically, the flux at a specific scale σ is defined by

$$flux_{\sigma}(x) = \frac{-1}{4\pi r^2} \int_{S_r(x)} < \nabla(G_{\sigma} * I), \hat{n} > ds$$

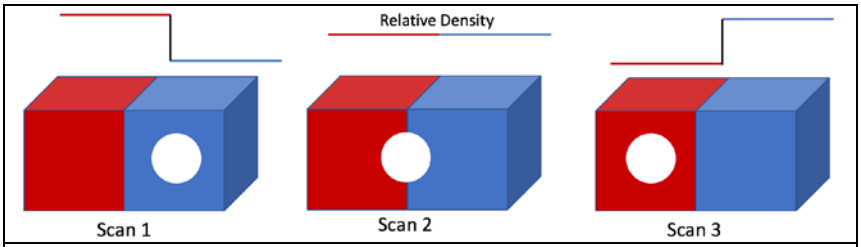

Fig 8. Schematic showing the impact of a sub-voxel bronchus on the MR-measured density for a series of MR scans that image the bronchus in different relative positions to the red and blue voxels.

where I denotes the image input, G_σ denotes a Gaussian kernel with bandwidth σ, $S_r(x)$ is the sphere with radius r centered on voxel x, and $\hat{n}$ is the outward normal on the sphere. To make the extracted flux feature robust towards the shape and scale variation in local sections of the BT, we propose to compute the flux at multiple scales, $\sigma \in \{\sigma_i\}, i = 1,,2,\ldots,k$, normalize the computed flux at each scale, and use the maximum across the scales as the final flux characteristic value at each voxel, as shown below.

In previous studies, we found three scales of $\sigma \in \{2.0,3.0,,4.0\}$ to be sufficient. We further suppress parenchymal background using a function of voxel intensity. We calculate the probability that a bronchus resides within the voxel using a piecewise linear intensity map f

$$flux(x) = \max_{\{\sigma \in \sigma_i\}} flux_\sigma(x)$$

$$p(bronchus \in x) = c \cdot f(I(x)) \cdot flux(x)$$

Where c is a normalization factor to make the overall likelihood a legitimate probability, f is the intensity function kernel applied to the voxel-wise MRE image intensity, and $flux(x)$ is the scale-robust flux characteristic value.

4. Tissue properties measurement and validation

During Q1 of Y1, work began toward the design and development of a custom system for tissue force measurements. The system will allow for the direct application of both shear and compressive forces to ex vivo tissues to characterize their properties. Various load conditions can be applied to the tissues via 3D printed applicators, which can be designed to simulate blunt or sharp objects in contact with tissues. They can also be printed with materials of different shore hardness to improve our understanding of tissue response to various mechanical stimuli.

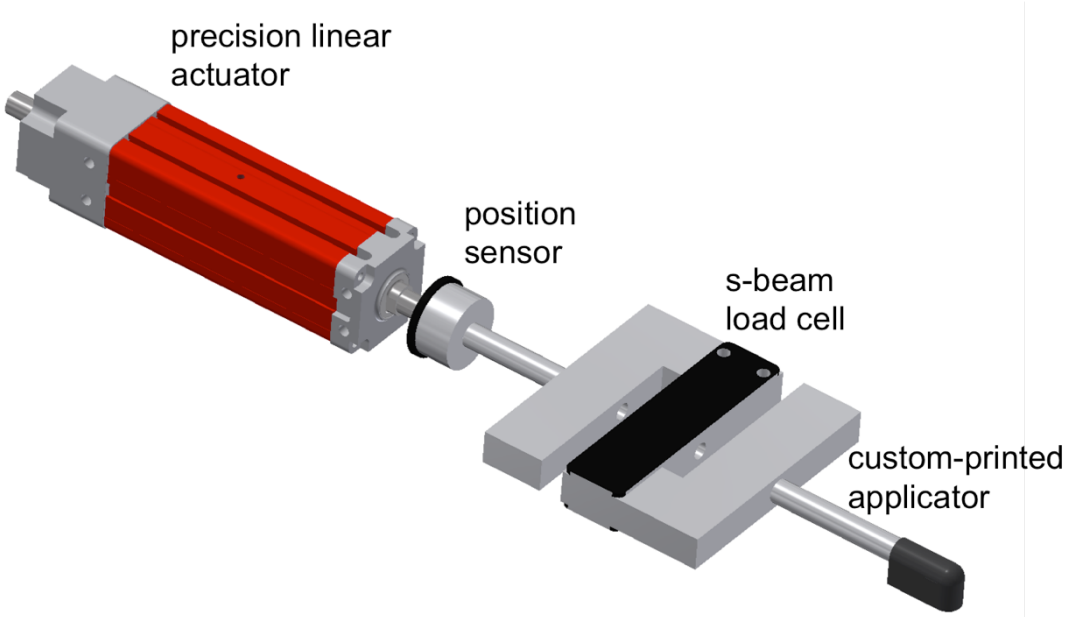

Figure 2. Force application system. A precision linear actuator is used for fine motor control. The position of the applicator tip is determined by the position sensor, which is in line with the system. The magnitude of the load is obtained from the output of the s-beam load cell.

The major activities during this reporting period include the design of the force application system (Figure 1). We also began to identify the major components that are to be implemented into the system.

During Q2 of Y1, our work has focused on the development of measurements of mechanical properties -especially viscoelasticity - of liver tissue *in vivo* and *ex vivo*. Compression and elongation tests have been conducted on a phantom tissue sample using a compact testing instrument (300C Dual-Mode system, Aurora Scientific Inc., Canada). By controlling the value of applied force and displacement, a variety of dynamic physical properties of tissue *ex vivo* such as creep, relaxation and strain-stress hysteretic curves at different strain rates can be obtained.

We are also developing transient elastography for measurement of the Young's modulus of liver tissue *in vivo*. By vibrating the skin of a patient using an electromechanical transducer at relatively low frequency (50Hz), a shear wave is induced and passes through the tissue. An ultrasound imaging system (Flex Focus 400, BK Ultrasound Inc., US) is used to monitor the shear wave and Young's modulus of tissue *in vivo* can be calculated from the measured shear wave speed.

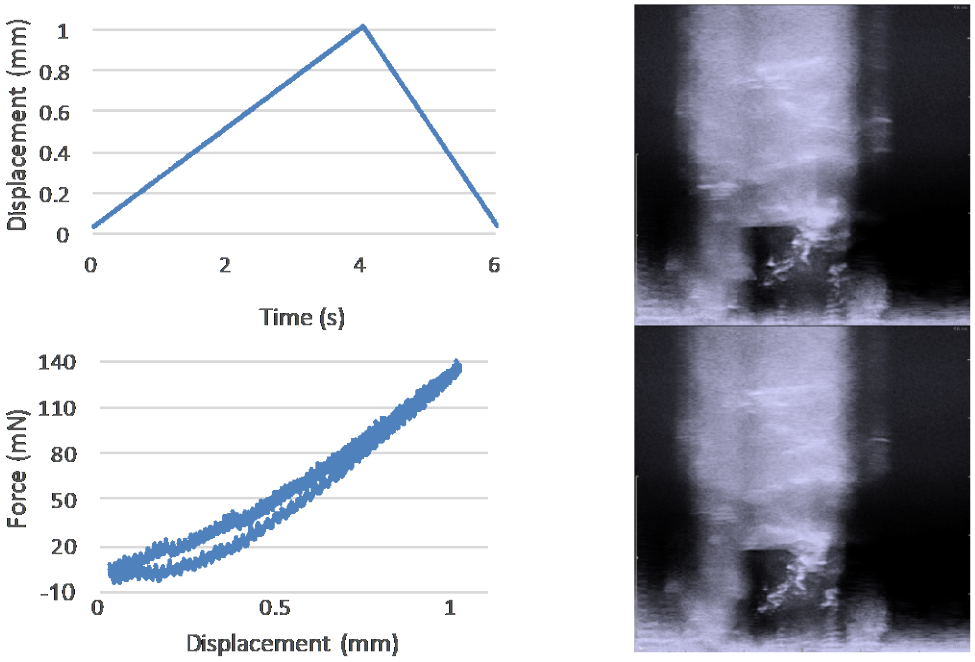

Fig. Preliminary results of measurements of a test (cubic sample, 19mm per side) phantom tissue piece. (a) Force-displacement curve at a loading speed of 0.25mm/s by using a cylindrical probe with 4 mm in diameter. (b) Ultrasound images of the phantom tissue for use in Young's modulus characterization.

During Q3 of Y1, our work focused on the measurement of mechanical properties - especially the hysteretic strain-stress curve – of *ex-vivo* porcine liver tissue. We are in regular contact with the modeling team to ensure our choice of measurements and methodologies (e.g., tissue sample choice, strain rates of measurement) are most applicable to their models.

A testing instrument (300C Dual Mode Muscle Lever system, Aurora Scientific Inc., Canada) was used to conduct compression tests on tissue samples. Test pieces of porcine liver tissue were cut from the middle and edge parts of lobes (as shown in Figure 1) into small cubes and the natural length of each test piece free from external force was measured before experiment. Both the top surface of stage and the bottom surface of actuator were covered with sandpaper to prevent slippage of the tissue. A picture of experiment setup is shown in Figure 2.

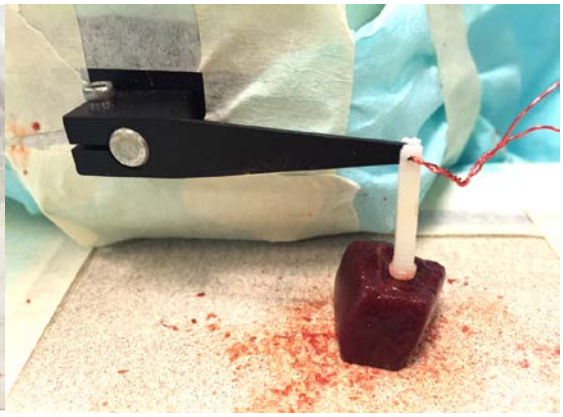

Figure 1 Porcine liver

Figure 2 Experiment setup

Compression tests were conducted on 6 test pieces from middle part (as shown in Figure 1) with lengths of 10, 10, 12 mm and from edge part with lengths of 7.5, 8.5 and 7 mm at different loading rates (1, 2, 5, 10mm/s). The maximum loading displacement was 3 mm for all test pieces and test pieces were unloaded immediately at the same rate once displacement reached maximum. The radius of actuator was 2 mm. All pieces were tested within 2 hours after the removal from the pig and were at room temperature.

Figure 3 shows the results of hysteretic strain-stress curves of test pieces from middle and edge parts of liver with different maximum strains at a loading rate of 10mm/s. Figure 4 shows the results of measurements of #1 test piece from middle part and #3 test piece from edge part at different loading/unloading rates.

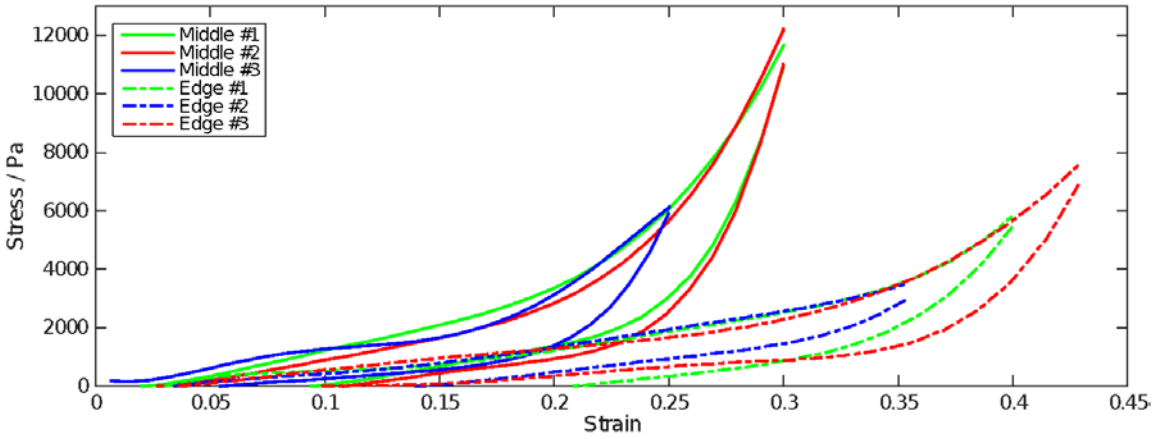

Figure 3 Results of measurements at a loading rate of 10 mm/s.

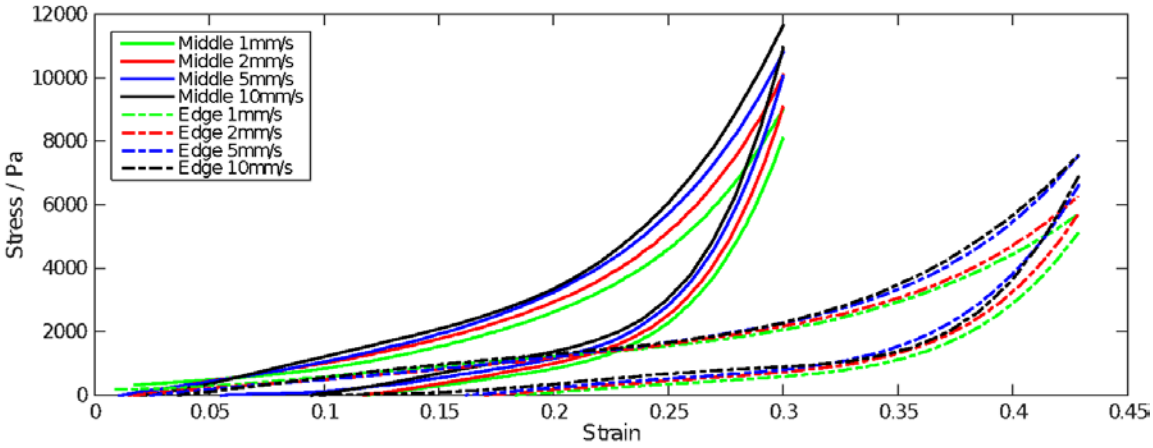

Figure 4 Results of measurements of piece 'Middle #1' and 'Edge #3' at different loading rates.

During Q4 of Y1, our work focused on the measurement of the reproducibility of the hysteretic displacement-force curve under different orders of loading rates of *ex vivo* rat liver tissue. We are in regular contact with the modeling team to ensure our choice of measurements and methodologies (e.g., tissue sample choice, strain rates of measurement) are most applicable to their models.

Biological tissue is a viscoelastic material, which shows both viscous and elastic characteristics when subjected to deformation. Two properties used to describe the behavior of viscoelastic materials are hysteresis and stress relaxation. Hysteresis is defined here as the time-based dependence of the detected force (or displacement) of tissue on present and past displacement (or force) applied to tissue). Stress relaxation is measured by applying a constant strain and measuring the decrease in restoring force of the material as a function of time.

The same testing instrument (300C Dual Mode Muscle Lever system, Aurora Scientific Inc., Canada) as mentioned in Y1Q3 report was used to conduct compression tests on the liver tissue samples from a male rat, which weighed ~ 420 - 460 g. Test pieces were cut from the middle part of lobes (as shown in Figure 1(a)) into small cubes (as shown in Figure 1(b)) and the natural length of each test piece (*i.e.*, free from external force) was measured before experiment. The sample was mounted on a stage, and force was applied with a robotically-controlled actuator. Both the top surface of the stage and the bottom surface of the actuator were covered with sandpaper to prevent slippage of the tissue. A picture of experiment setup is shown in Figure 1(c).

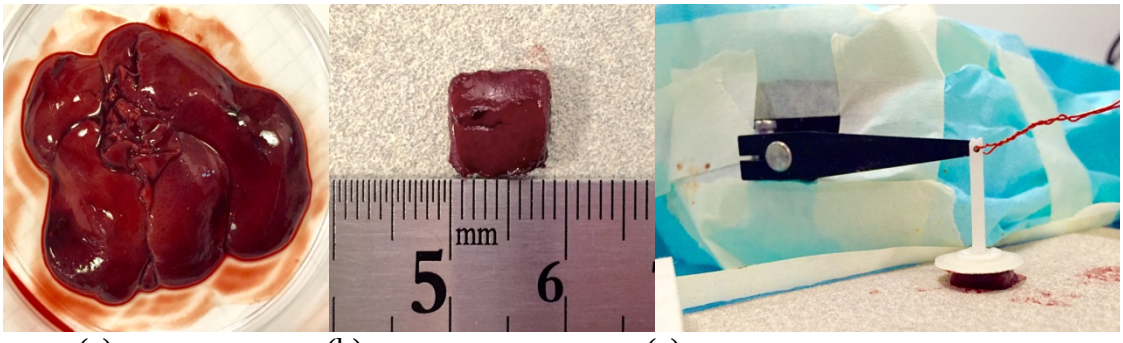

(a) (b) (c)

Figure 1 (a) Gross rat liver tissue; (b)Test pieces cut from the tissue; (c) Experimental setup.

Compression tests were conducted on 4 test pieces from middle part of the rat liver with lengths of 9.5, 9, 8, 9 mm and thicknesses of 3.5, 2.5, 2, 5 mm, respectively,. The samples were numbered #1-#4 corresponding with the order they are given in the previous sentence, and each sample was tested at multiple loading rates (0.02, 1, 2, 5, 10 mm/s). The maximum loading displacement was 1 mm for all test samples. To measure the hysteretic displacement-force curves of tissue, test samples #1 to #3 were unloaded immediately at the same rate once displacement reached maximum. To measure the stress relaxation curves of tissue, sample #4 was loaded at 0.02 mm/s for 50 seconds, held still for 300 seconds and unloaded at 0.02 mm/s for 50 seconds. The diameter of the actuator was 15 mm which is larger than the characteristic lengths of all test samples and offered more uniform compression on test pieces. All pieces were tested within 2 hours after removal of the liver from the rat and were kept at room temperature, 23.8±0.5°C.

Figure 2 shows the results of reproducibility test of the hysteretic displacement-force curves for samples #1 to #3 at a loading rate of 0.02 mm/s. The experiment was performed 3 times for each sample. The blue line indicates the average value of force measured and red lines indicate the standard deviation at selected displacements. As can be seen, the standard deviation of force becomes larger when displacement becomes larger. Figure 3 shows the hysteretic displacement-force curves of sample #1 to #3 at different orders of loading rates. These experiments were primarily designed to validate and improve experimental protocols and no statistically significant conclusions can yet be made due to the small sample size. Figure 4 shows the results of relaxation test of test sample #4. The blue line indicates the average value of force measured and the red line is a fitting line of the blue curve. Stress relaxation can be seen as the force steadily decayed from 50 to 350 seconds caused by the induced plastic displacement of tissue, which provided a smaller force compare to the elastic displacement, when tissue was held at a constant displacement for a finite time. From 350 to 400 seconds, the tissue was unloaded. As can be seen, force reached a negative value after unloading since tissue was still stuck on the probe of actuator which applied a force to the probe in the opposite direction.

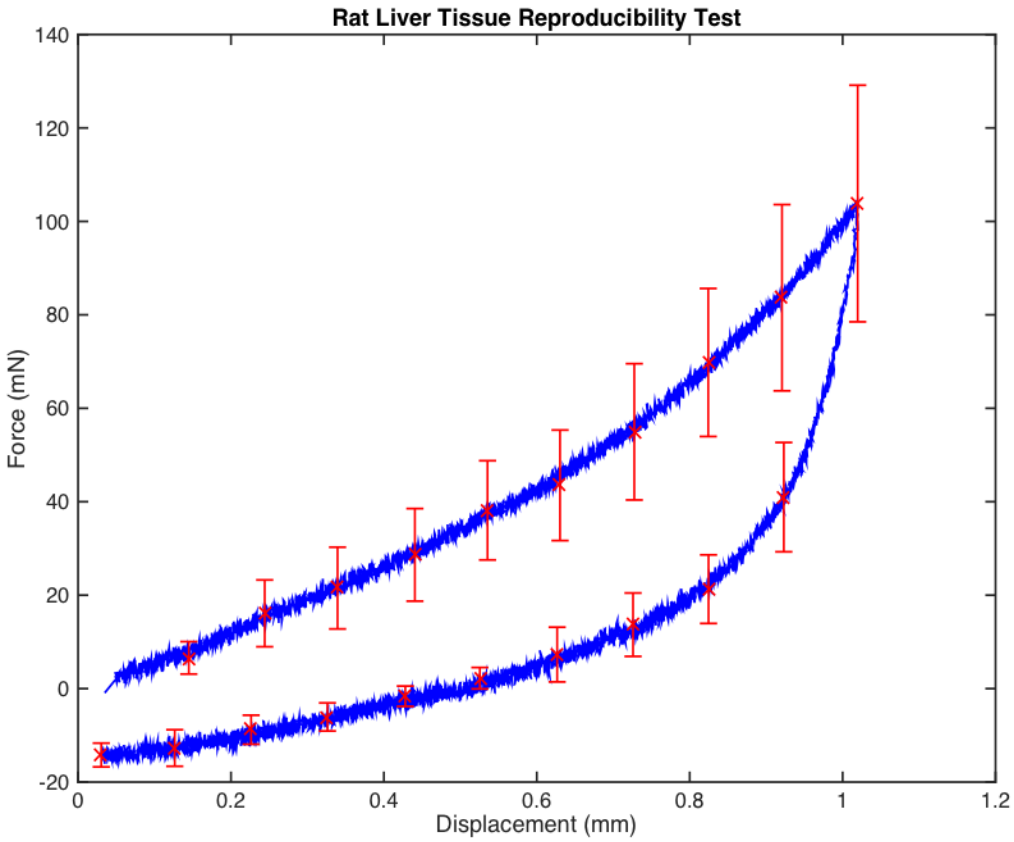

Figure 2 Results of reproducibility test at a loading rate of 0.02 mm/s.

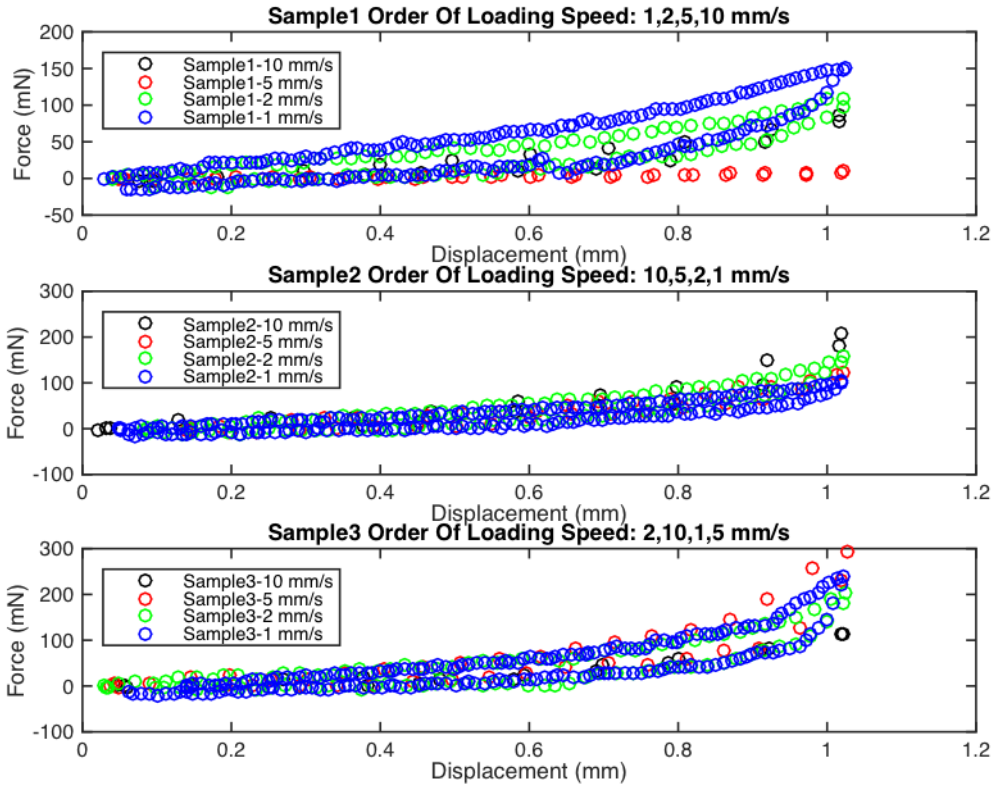

Figure 3 Results of measurements of sample #1 to #3 at different orders of loading rates.

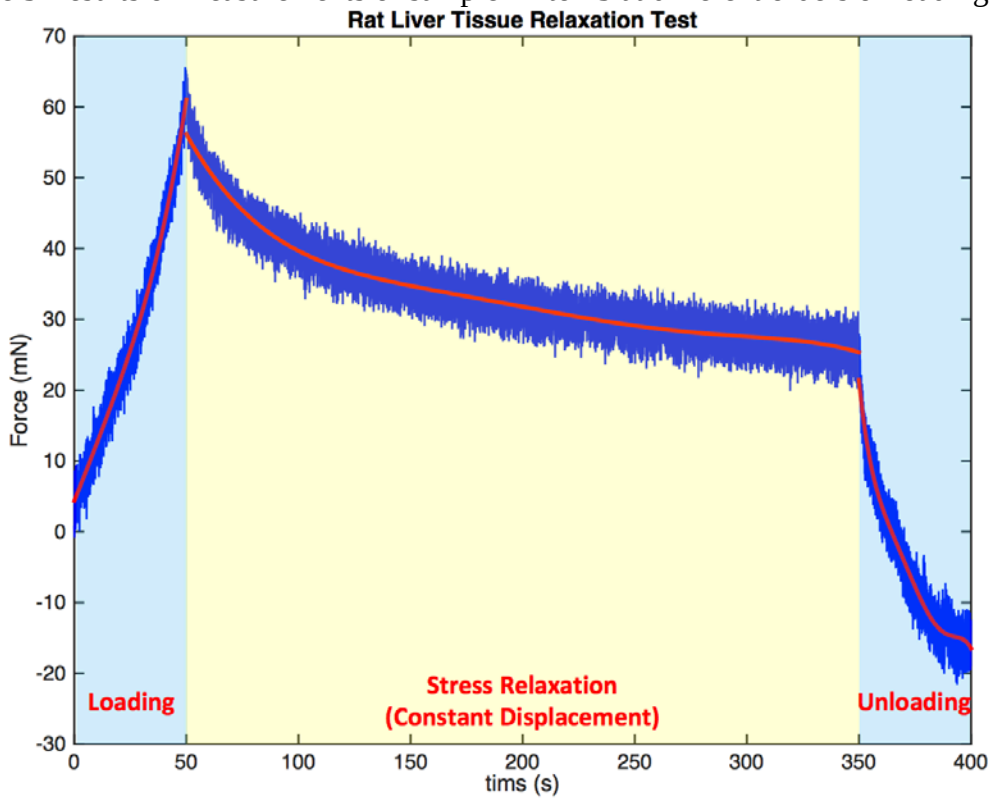

Figure 4 Results of relaxation test of sample #4.

During Q1 of Y2, our work focused on developing a comprehensive experiment method to measurement the mechanical properties of ex vivo perfused and sectioned porcine liver. We are in regular contact with the modeling team to ensure our choice of measurements and methodologies (e.g., tissue sample choice, strain rates of measurement) are most applicable to their models.

A freshly harvested liver will be flushed with cold veterinary lactated ringer's solution before transporting to the room where the liver will be perfused and tested. The schematic of the perfusion system is shown in Figure 1. Six liters of a specific kind of perfusate (5L Dextrose 5% Lactated Ringers Solution and 1 L 6% Hetastarch solution[1]) will be pumped to two hydro-statically elevated reservoirs. The organ will be stabilized on a sturdy surface without submerging the organ. The temperature of the perfusate will be maintained at 39ºC which is the core temperature of a pig.

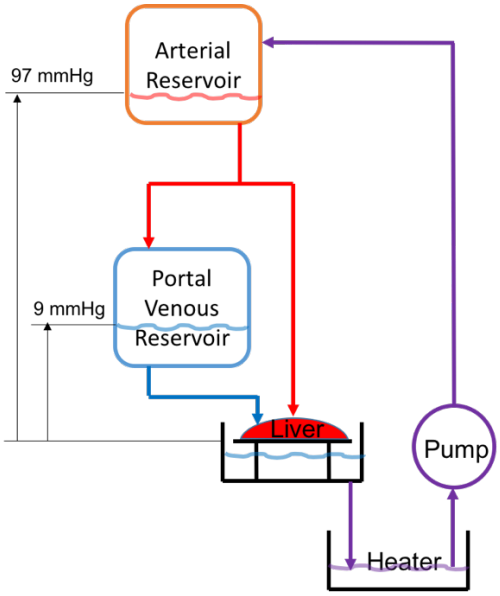

Figure 1 Schematic of the perfusion system.

The same testing instrument (300C Dual Mode Muscle Lever system, Aurora Scientific Inc., Canada) as mentioned in the Y1Q4 report was used to apply a compression force on the liver surface. The diameters of the probes were selected based on the statement from Zhang et al.[2]. The diameters were selected to be 5 mm and 6 mm for the indentation tests and stress relaxation/creep tests. The surface of the probe will be covered by fine grit sand paper to prevent relative motion at the interface.

Quasi-static indentation, indentation at different loading rates, stress relaxation and creep tests will be conducted on different lobes of the perfused liver. The surface of each lobe will be meshed to 25 mm x 25 mm grid and testing points are located in the center of each square (as shown in Figure 2). The natural thickness of each testing point will be measured and recorded before testing.

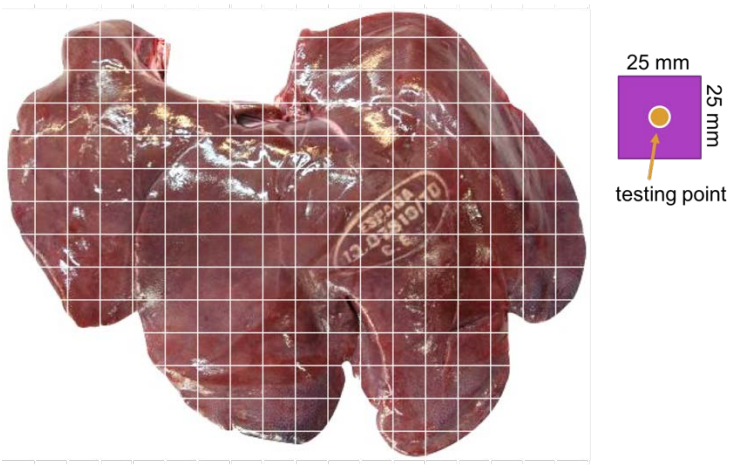

Figure 2 Testing points are shown on the surface of a porcine liver.

For quasi-static indentation tests conducted on one lobe of the perfused liver, the maximum strain will be 0.05 and the loading/unloading rate is 0.2 mm/s. The sample will be immediately unloaded once the displacement reaches the maximum value. Each testing points will be tested for three times and it will be allowed to recovery for 1 hour before the next measurement.
For indentation test at different loading rates conducted on another lobe of the perfused liver, the maximum strain will be 0.15 and the loading/unloading rates will be 1, 2, 5, 10, 20 and 50 mm/s. Three testing points, which are only located in the middle part of the lobe, are loaded at each rate only for one time.

For stress relaxation test conducted on another lobe of the perfused liver, the maximum strain will be 0.2 and the loading rate is 10 mm/s. For creep tests conducted on the same lobe of the perfused liver, the loading rate is the same and the maximum load will be chosen from 0.1, 0.2, 0.5, 0.7, 1, 1.25, 1.5, 2, 2.5 and 3 N based on the force data measured in the previous tests to prevent the liver from damage. The waiting time for both tests will be 300 sec. And three testing points from the middle and edge part of the lobe will be tested in each kind of experiment.

After all the tests are done on the perfused liver, the liver will be sectioned into small cubes along the lines of the 25 mm x 25 mm grid. So same testing points are tested after the perfusion system is removed from the liver. The procedures of those four kinds of tests mentioned above for sectioned liver tissue samples are the same as above. According to the opinions from our modeling group, we will submerge the tissue sample in the perfusate to take the possible poroelasticity of the liver into consideration. And the schematic of that experiment setup is shown in Figure 3. We will also explore the anisotropic properties of parenchyma by removing the Gibson capsule and conduct indentation tests in all three directions.

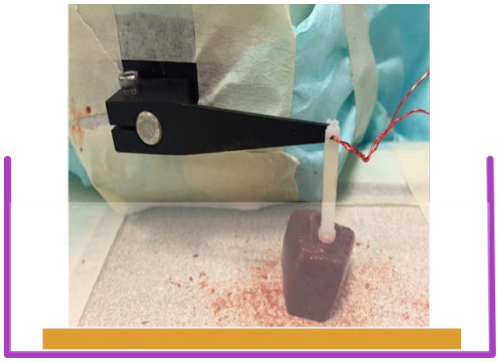

Figure 3 Schematic of experiment setup used for sectioned liver samples.

During Q2 of Y2, our work focused on conducting quasi-static indentation tests on perfused and sectioned liver tissue. We are in regular contact with the modeling team to ensure our choice of measurements and methodologies (e.g., tissue sample choice, strain rates of measurement) are most applicable to their models.

A liver, which weighed 918 g, was perfused with 5 liters of 39ºC normal saline solution within 2 hours of removal from a female pig (as shown in Figure 1).

Figure 1 Picture of the liver used in our experiment.

The experiment setup of the perfusion system is shown in Figure 2.

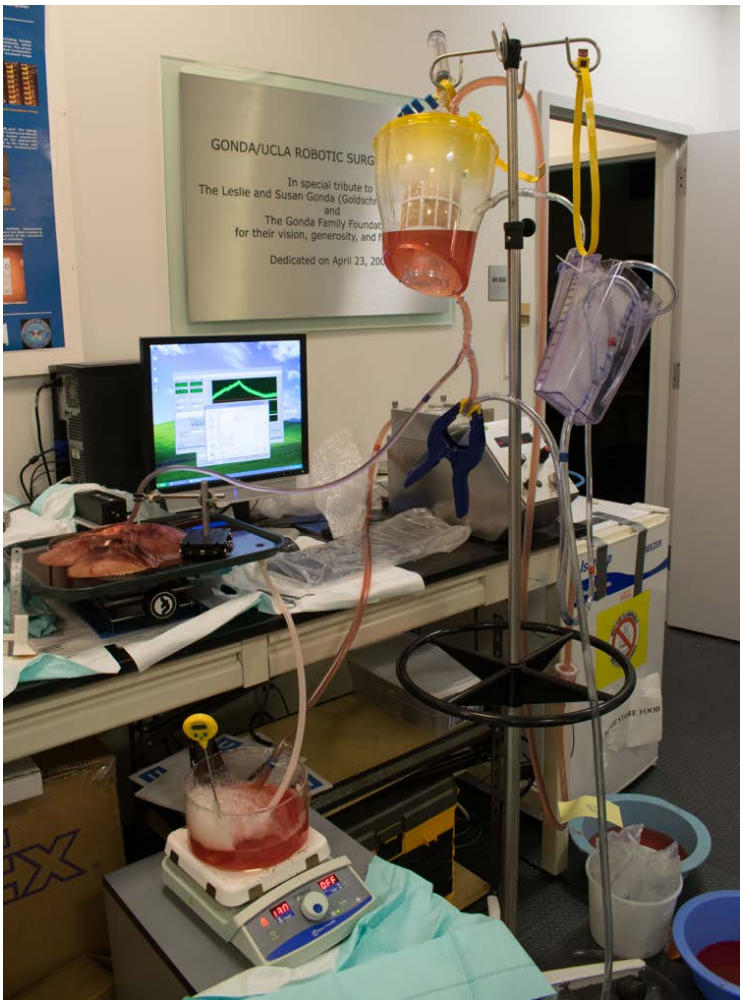

Figure 2 Picture of the perfusion system.

After all quasi-static indentation tests were done on the perfused liver, the perfusion system was removed from the liver. The liver was stored in a fridge at 4 ºC for 16 hours before further action was taken. All tests were conducted on the right lobe of the liver shown in Figure 1. That lobe was sectioned to small cubes along the lines of 25 mm x 25 mm grid. The sectioned liver samples are shown in Figure 3.

During the experiment, all samples are submerged in the normal saline The experiment setup of the sectioned liver sample is shown in Figure 4.

Figure 3 Picture of the sectioned liver tissue samples. Samples are label as (i, j) where i is the row number and j is the column number.

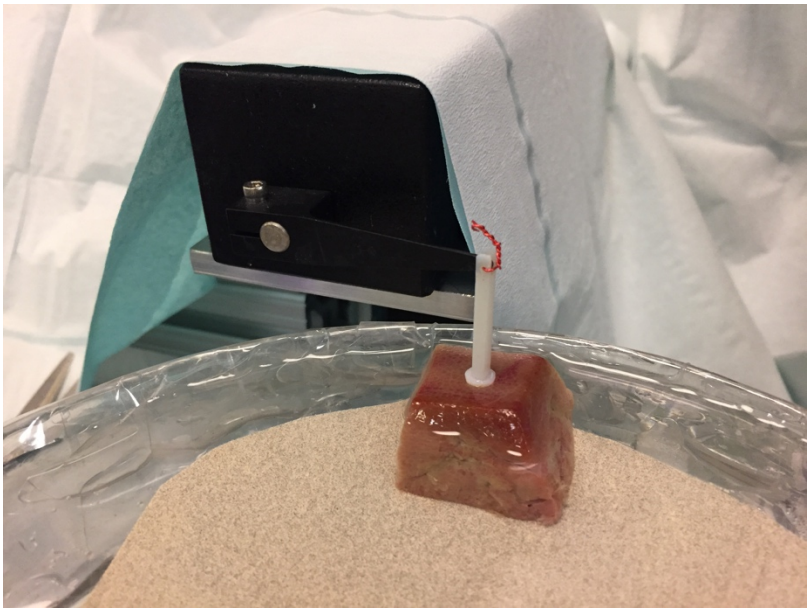

Figure 4 Picture of the experiment setup of sectioned liver samples.

In quasi-static indentation tests, the maximum strain was 0.05 and the loading/unloading rate was 0.2 mm/s. The sample was immediately unloaded once the displacement reached the maximum value. Each testing points were tested for 2 times when the liver was perfused and 3 times for sectioned liver samples. All testing points was allowed to recovery for 1 hour before the next measurement.

The hysteretic force-displacement curves of each testing point of perfused liver and sectioned liver are shown in Figure 5 and Figure 6 respectively. We can see that the sectioned liver tissue became stiffer as the number of test time went up because the liquid inside the sample was squeezed out and tissue was stick to each other during the tests. We inspected and recorded the diameters of the maximum vessels in the samples. And one thing to note is that all sectioned tissue samples had vessels inside the parenchyma. However, changes in mechanical properties cannot be easily told from those curves of the perfused liver tissue.

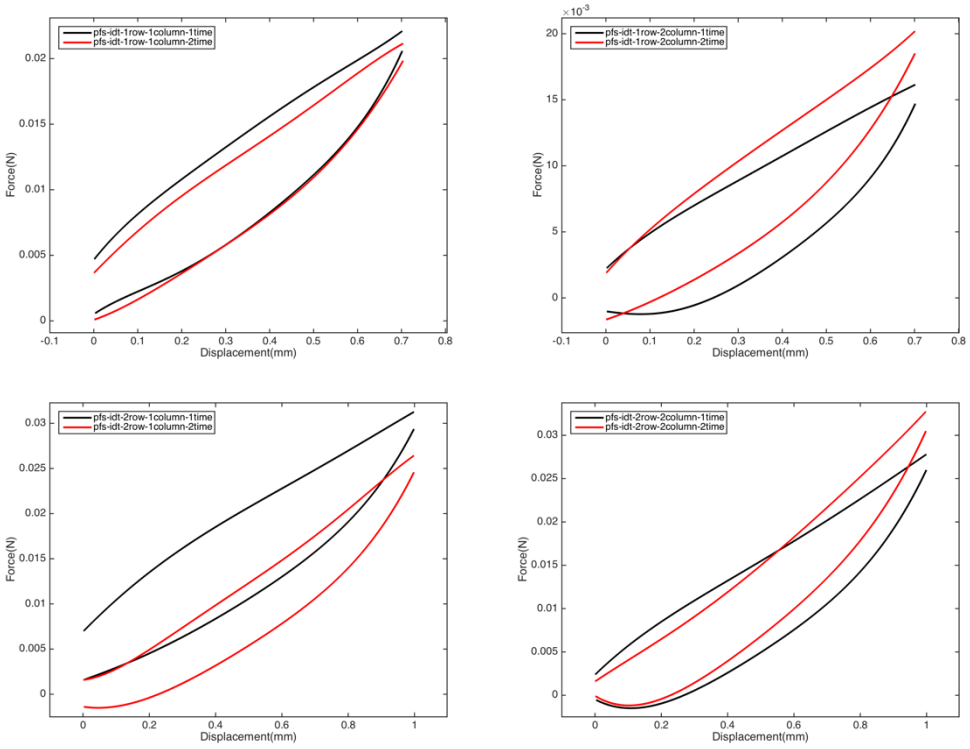

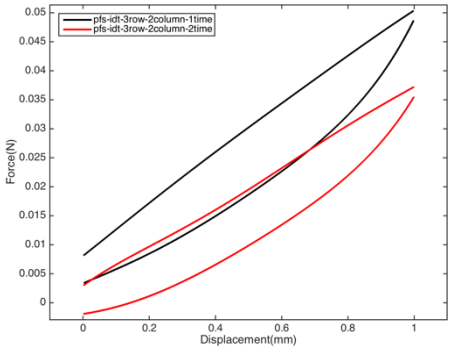
pfs-idt-3row-2column-1time
pfs-idt-3row-2column-2time
Force(N)
Displacement(mm)

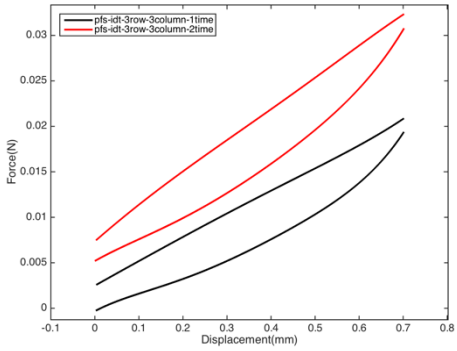
pfs-idt-3row-3column-1time
pfs-idt-3row-3column-2time
Force(N)
Displacement(mm)

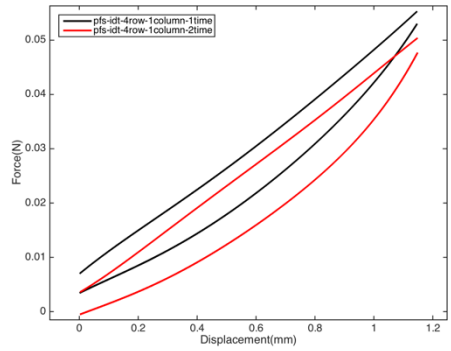
pfs-idt-4row-1column-1time
pfs-idt-4row-1column-2time
Force(N)
Displacement(mm)

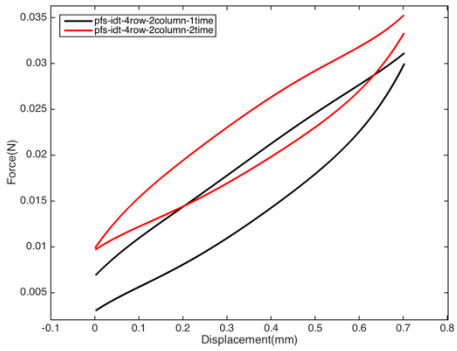
pfs-idt-4row-2column-1time
pfs-idt-4row-2column-2time
Force(N)
Displacement(mm)

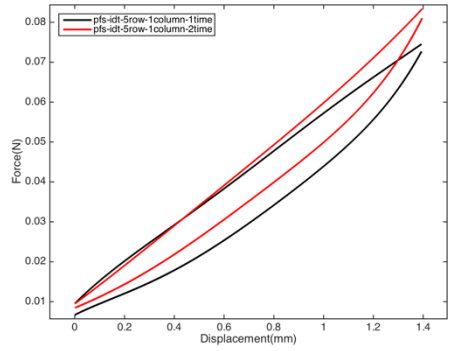
pfs-idt-5row-1column-1time
pfs-idt-5row-1column-2time
Force(N)
Displacement(mm)

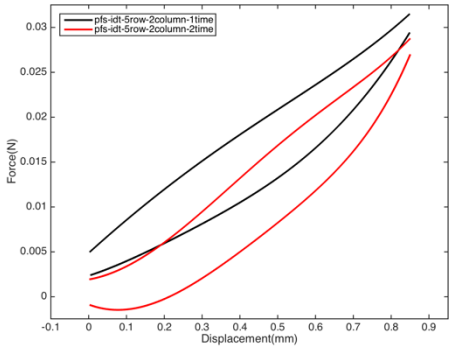
pfs-idt-5row-2column-1time
pfs-idt-5row-2column-2time
Force(N)
Displacement(mm)

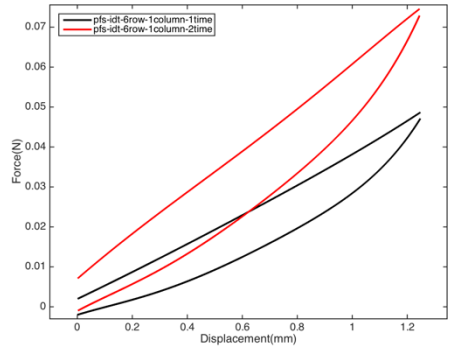
pfs-idt-6row-1column-1time
pfs-idt-6row-1column-2time
Force(N)
Displacement(mm)

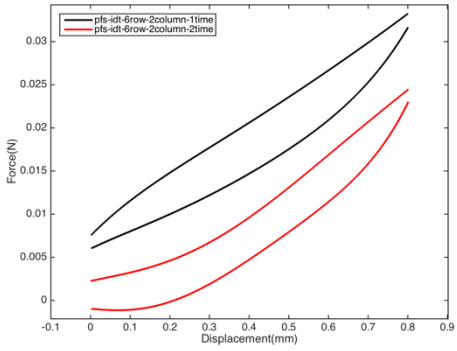
pfs-idt-6row-2column-1time
pfs-idt-6row-2column-2time
Force(N)
Displacement(mm)

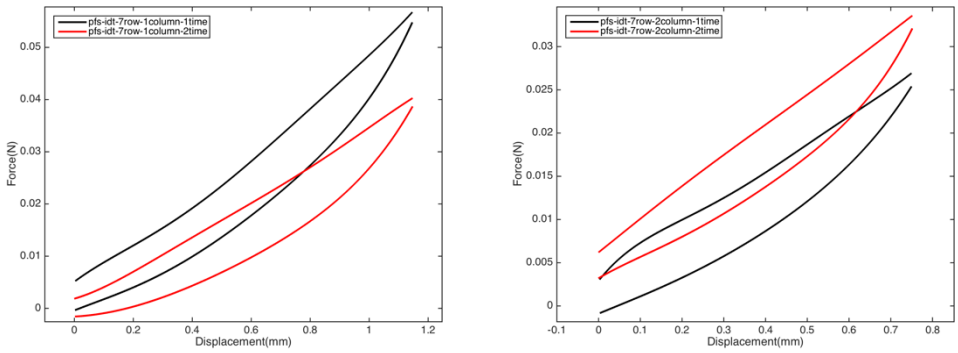

Figure 5 Hysteretic force-displacement curves of indentation tests on the perfused liver.

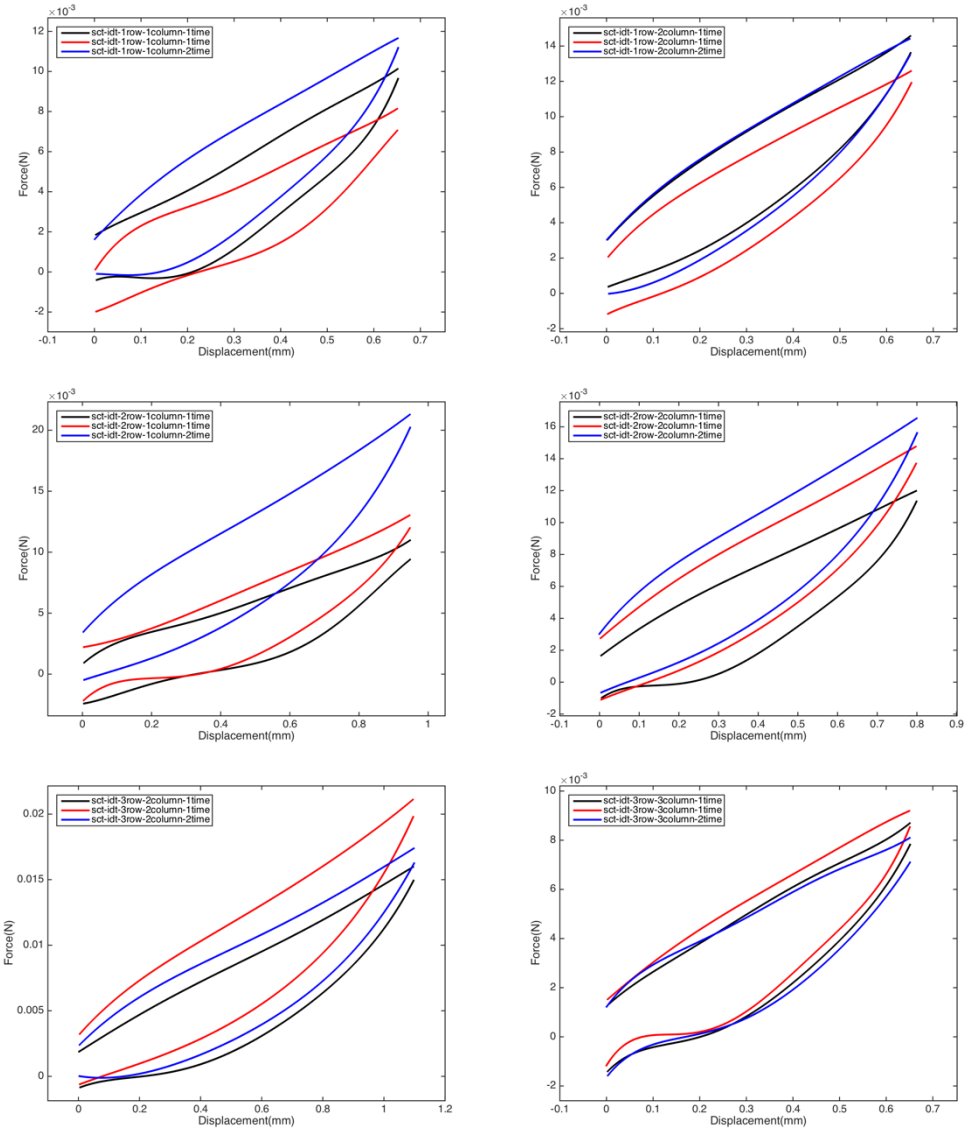

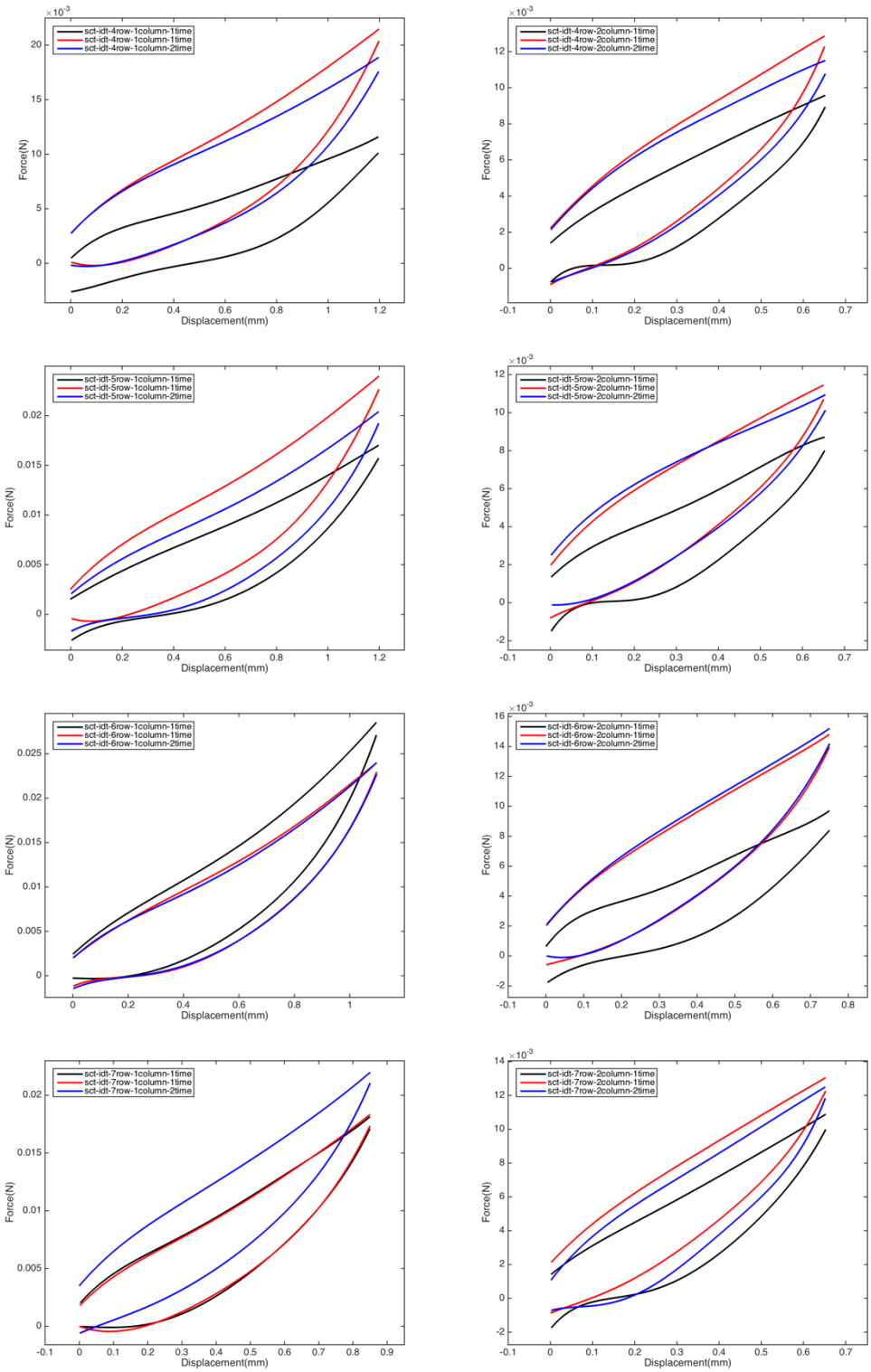

Figure 6 Hysteretic force-displacement curves of indentation tests on the sectioned liver samples.

We took the average value of the data collected from the 2 or 3 times measurements and summarized them in Figure 7 and Figure 8. We can see that perfused tissue was much stiffer and more linear than sectioned tissue.

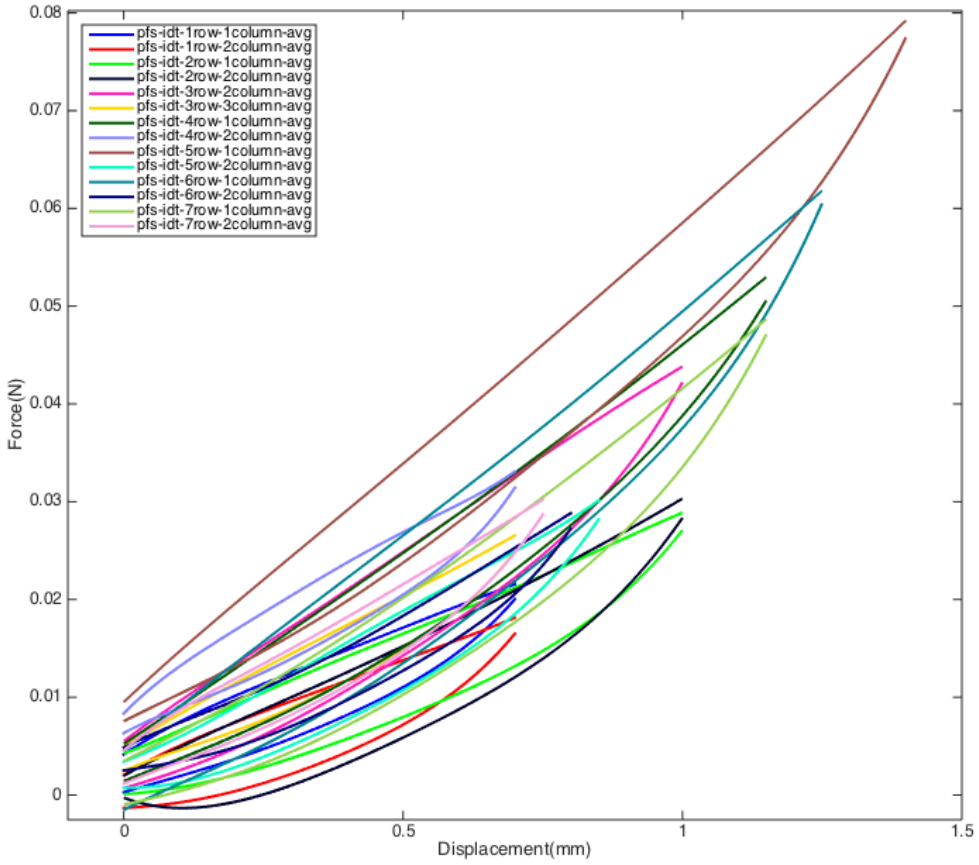

Figure 7 Hysteretic force-displacement curves of indentation tests at all testing points on the perfused liver.

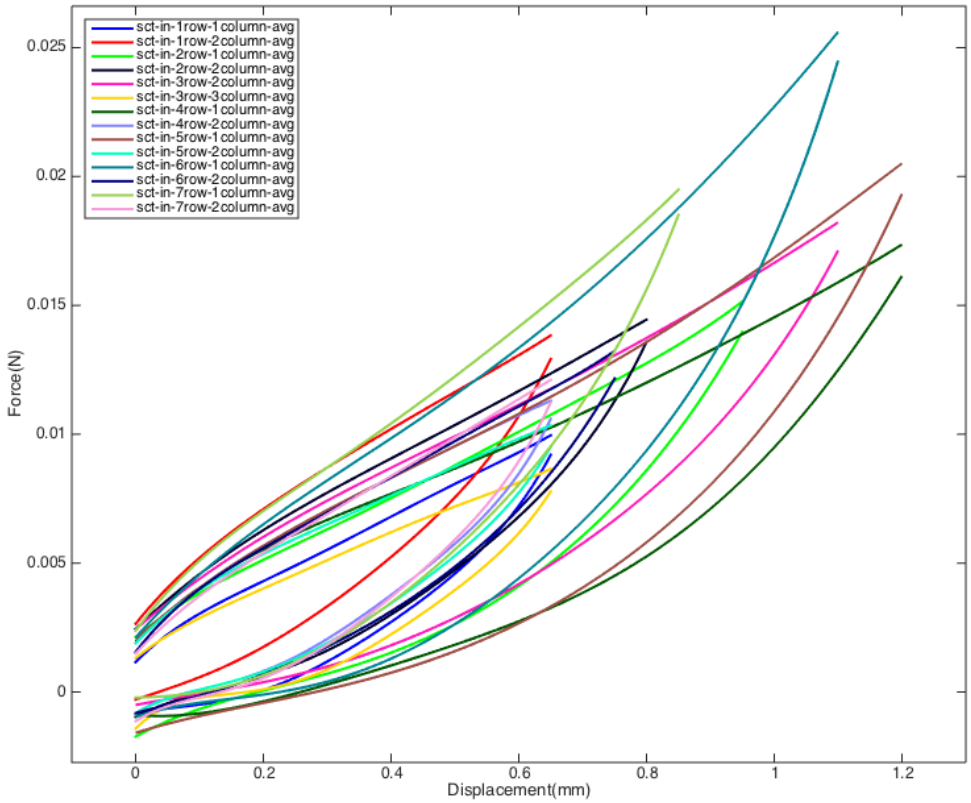

Figure 8 Hysteretic force-displacement curves of indentation tests at all testing points on the sectioned liver samples.

During the experiment, the diameter of the probe was 5mm. And by dividing the displacement by the natural thickness measured before each test, the hysteretic stress-strain curves of all testing points are summarized in Figure 9 and Figure 10. As it was mentioned before, the maximum strain for all tests was 0.05 and the loading and unloading processes were quasi-static. We can see from those figures that the tissue from the middle part of the liver is much stiffer than those from the edge part of the liver.

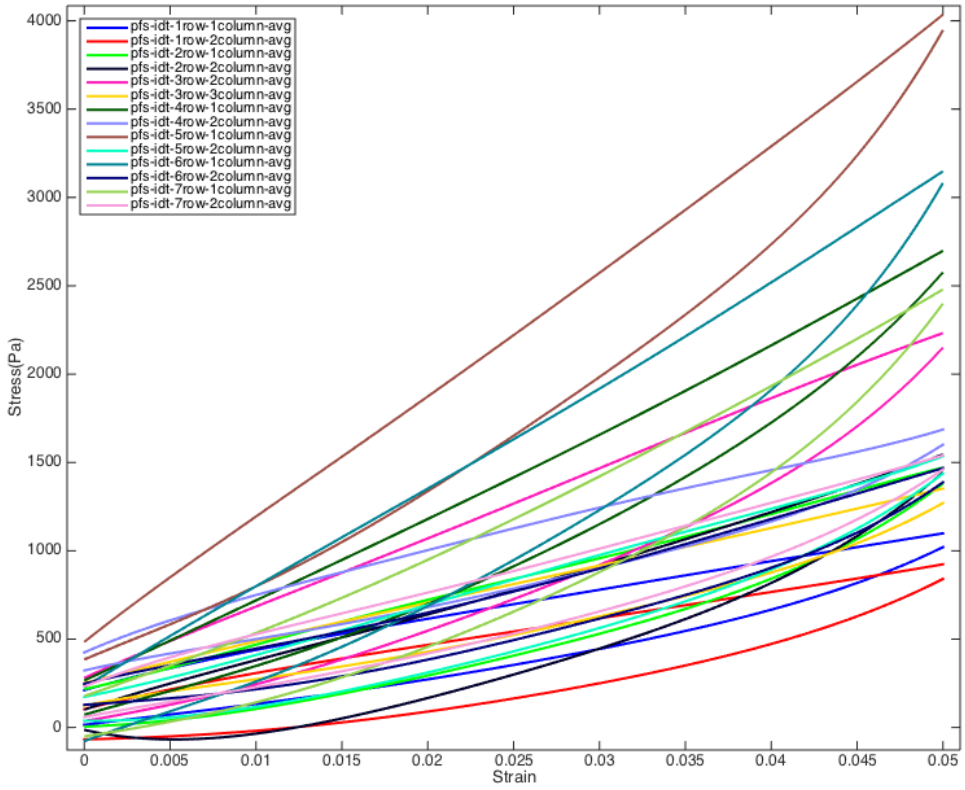

Figure 9 Hysteretic stress-strain curves of indentation tests at all testing points on the perfused liver.

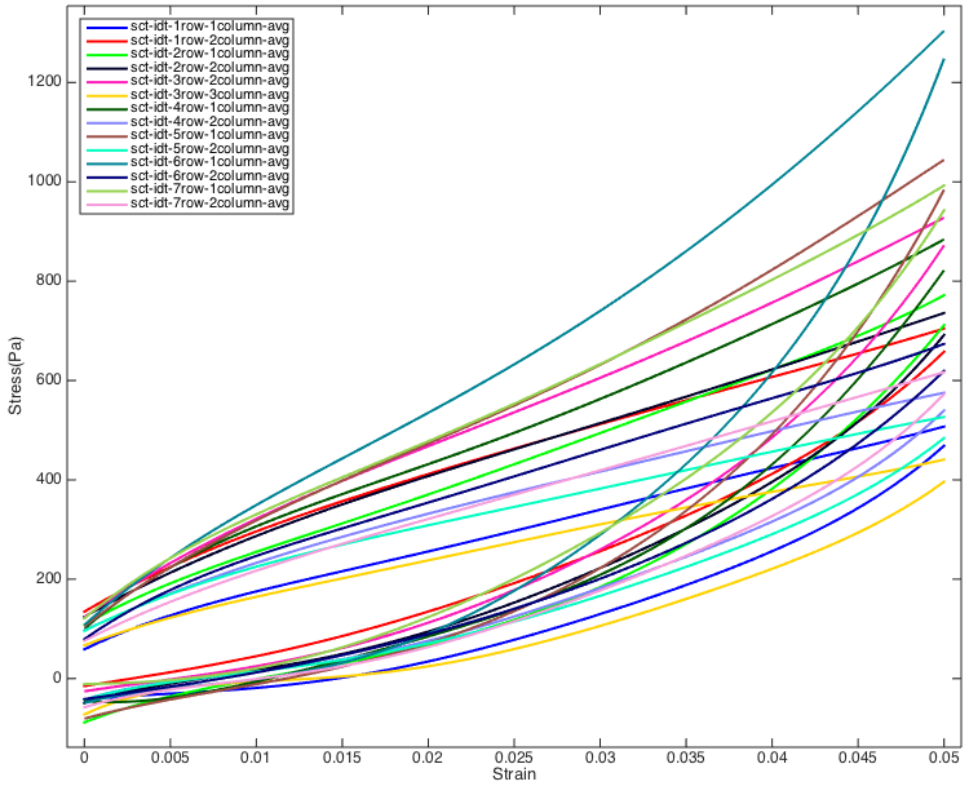

Figure 10 Hysteretic stress-strain curves of indentation tests at all testing points on the sectioned liver samples.

During Q3 of Y2, our work focused on conducting dynamic indentation tests on perfused and sectioned liver tissue. We are in regular contact with the modeling team to ensure our choice of measurements and methodologies (e.g., tissue sample choice, strain rates, relaxation, etc.) satisfies the requirements of the model development team.

A second liver, which weighed 1.05 kg, was perfused with 5 liters of 39 ºC normal Plasma-Lyte A Injection solution within 2 hours of removal from a female pig (as shown in Figure 1).

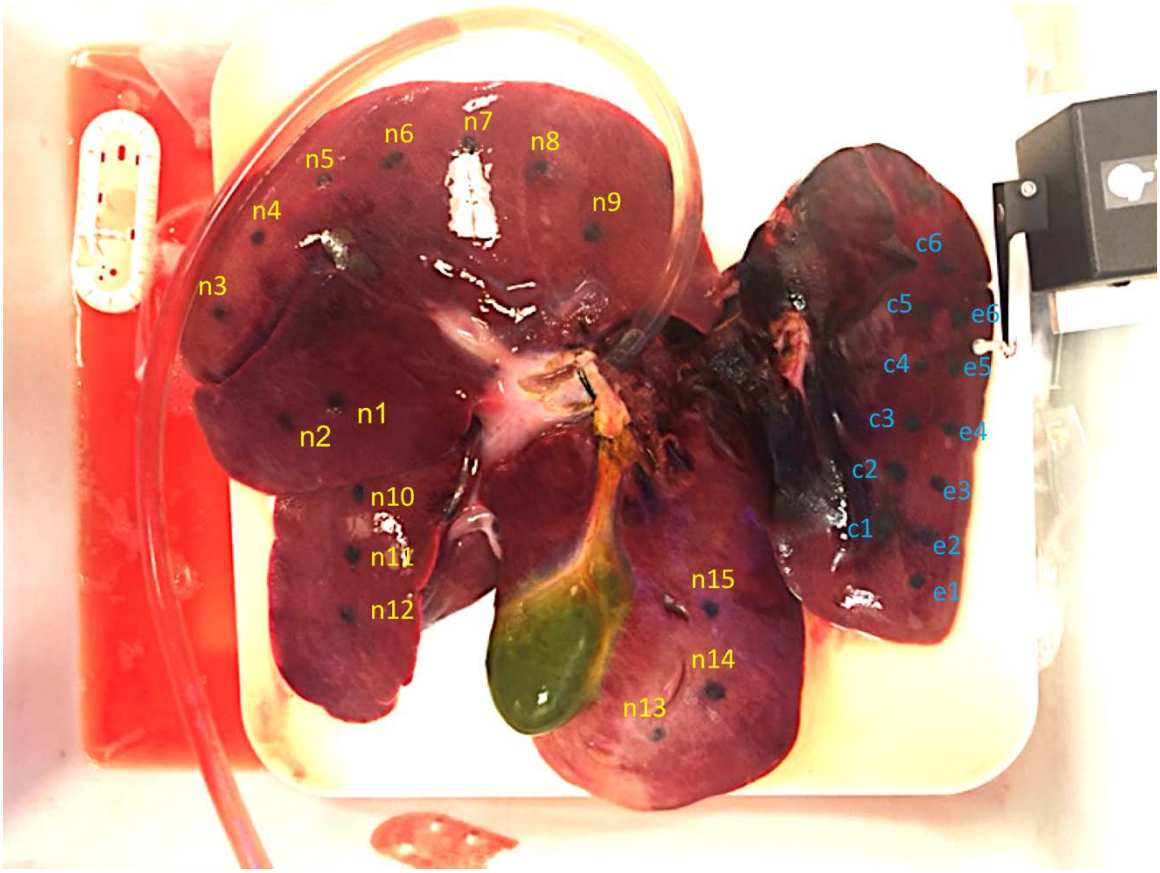

Figure 1 Picture of the perfused liver used in our experiment. Testing points used in indentation tests at different loading rates are labeled with yellow texts. And testing points used in stress relaxation and creep tests are labeled with blue texts.

The experiment setup of the perfusion system is shown in Figure 2. A probe with 5 mm in diameter was used in all measurements.

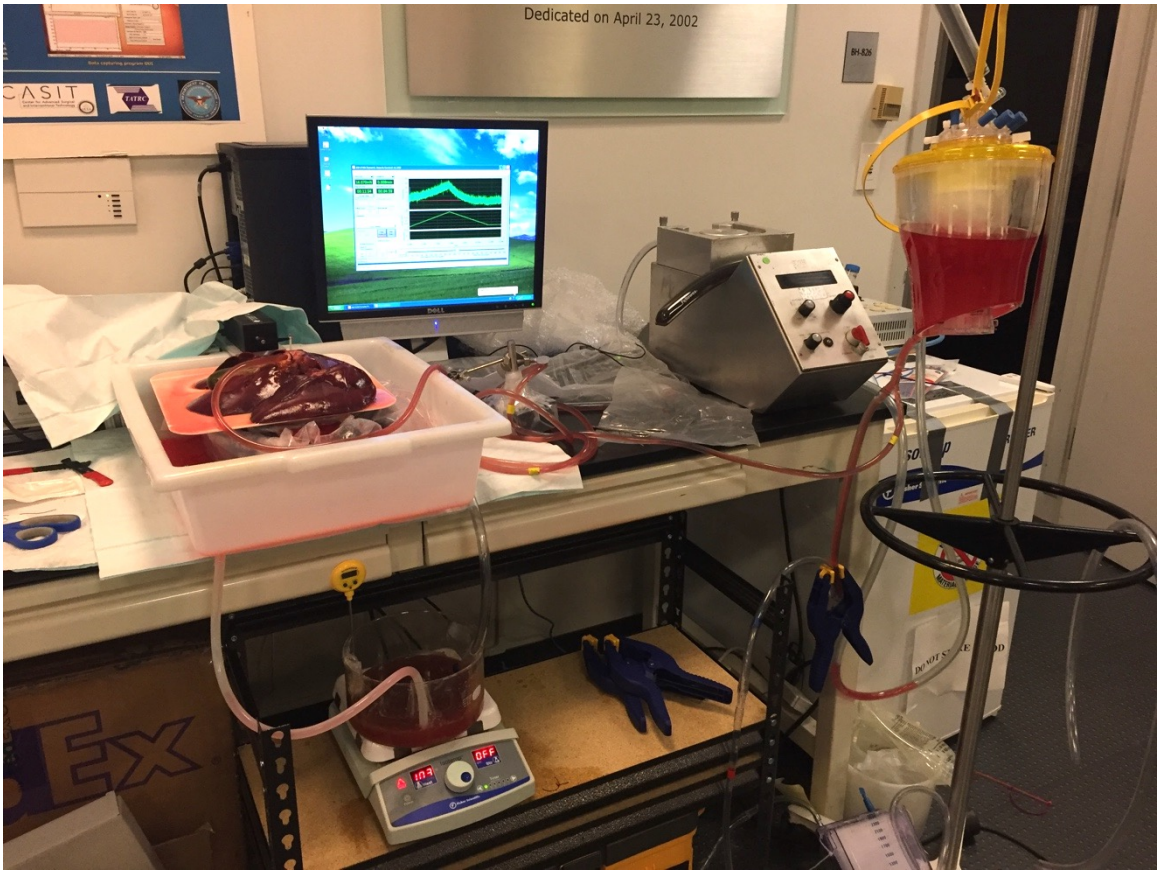

Figure 2 Picture of the perfusion system. The portal venous reservoir was elevated at 122 mm (9 mm Hg) above the top surface of the liver.

After all dynamic indentation tests were done on the perfused liver, the perfusion system was removed from the liver. The liver was stored in a refrigerator at 4 ºC for 12 hours prior to any additional experiments. All testing points are shown in Figure 1. Testing points for indentation, and relaxation and creep testing were sectioned into small cubes with a top surface area of 25 x 25 mm^2 and 10 x 10 mm^2, respectively.

During the experiment, all samples were submerged into normal Plasma-Lyte A Injection solution at room temperature. The experiment setup of the sectioned liver sample is the same as that used in quasi-static indentation tests at different locations as shown in the Year1 Quarter 6 report.

In indentation tests at different loading rates, the maximum strain was 0.3. Three testing points from n1 to n15 were loaded/unloaded at 1, 2, 5, 10, and 20 mm/s respectively. The sample was immediately unloaded once the displacement reached the maximum value. Each testing point was tested for 3 times when the liver was perfused and was tested for 3 times again when that location was sectioned. All testing points were allowed to recovery for 30 minutes before the next measurement.

We took the average of all measurements of all three testing points with the same loading/unloading rates and fitted them to the following Ogden model (two constants) with R^2>0.95,

$$\sigma^{eng} = \mu\left((1-\varepsilon)^{\alpha-1} - (1-\varepsilon)^{-\frac{1}{2}\alpha-1}\right) \quad (1)$$

where σ^{eng} is engineering stress, ε is engineering strain, μ and α are material constants. The hysteretic stress-strain curves of different loading rates of the perfused and sectioned liver samples are shown in Figure 3 and Figure 4 respectively. The material constants and energy lost density of each curve are summarized in Table 1. We can see that the liver tissue became stiffer as the loading rate went up because of its viscoelastic properties. We inspected and recorded the diameters of the maximum vessels in the samples. And one thing to note is that all sectioned tissue samples had vessels inside the parenchyma.

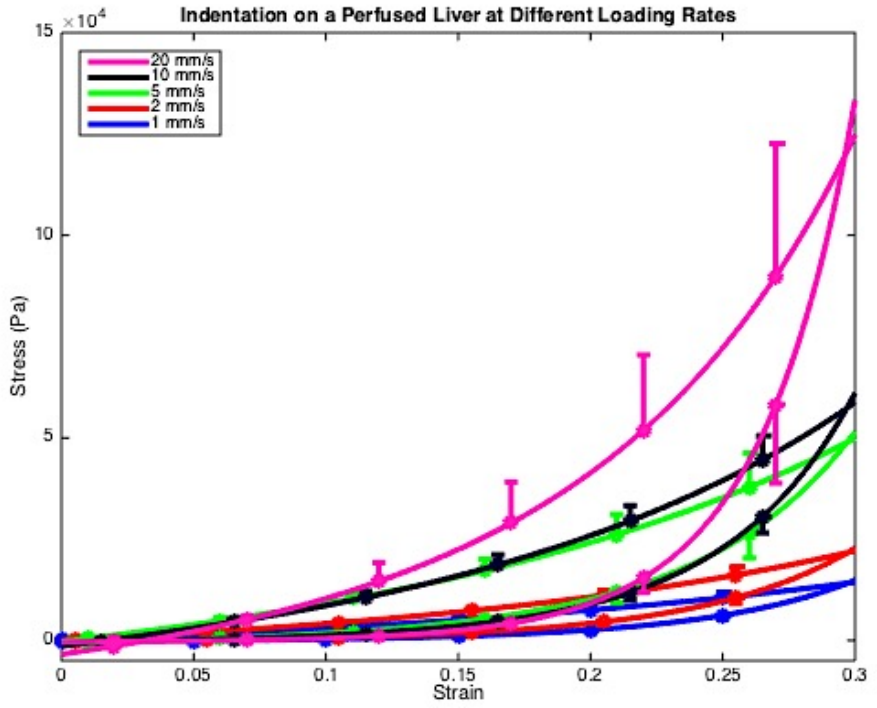

Figure 3 Hysteretic stress-strain curves of indentation tests at different loading rates on the perfused liver.

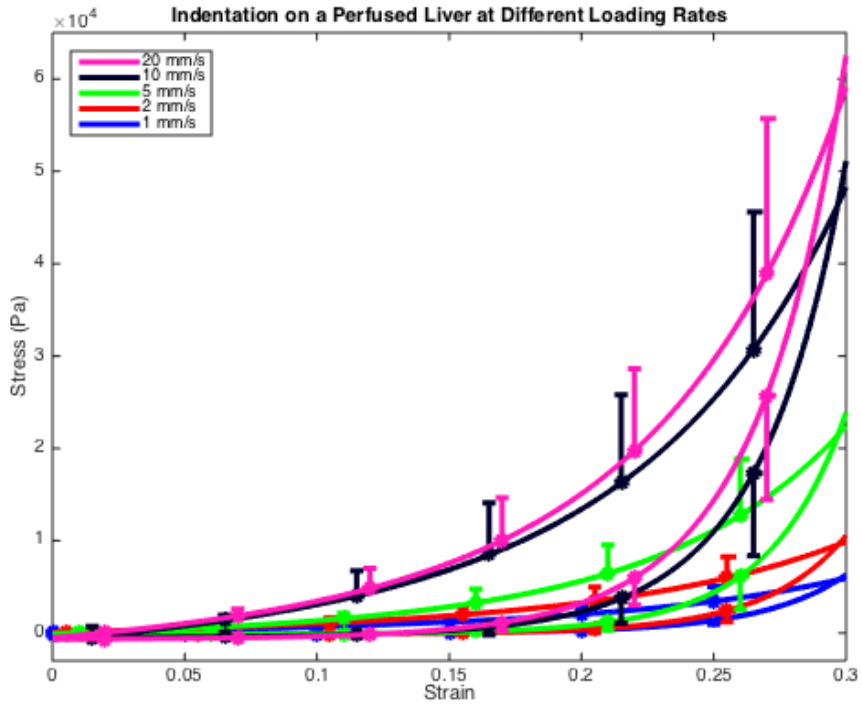

Figure 4 Hysteretic stress-strain curves of indentation tests at different loading rates on the sectioned liver samples.

Table 1 Parameters of the Ogden model representing indentation experimental data and energy lost density of each hysteresis curve.

Loading/ Unloading Rate (mm/s)	Perfused Liver					Sectioned Liver Samples				
	Loading		Unloading		Energy Lost Density (J/m^3)	Loading		Unloading		Energy Lost Density (J/m^3)
	$\overline{\mu}$	$\overline{\alpha}$	$\overline{\mu}$	$\overline{\alpha}$		$\overline{\mu}$	$\overline{\alpha}$	$\overline{\mu}$	$\overline{\alpha}$	
1	1.19e4	-1.36	-199.42	22.33	801.95	374.86	-6.77	-2.84	41.26	261.85
2	8.81e3	-2.45	-332.37	21.84	1.04e3	613.66	-6.84	-2.96	43.92	420.27
5	2.16e4	-2.32	-845.97	21.14	2.17e3	659.21	-8.92	-4.50	46.11	646.78
10	1.54e4	-3.33	-417.23	26.01	2.41e3	2.11e3	-7.86	-21.54	41.63	1.47e3
20	1.05e4	-6.13	-119.16	37.39	4.13e3	1.89e3	-8.70	-38.12	39.57	1.61e3

From Table 1, the relationships between parameters ($\overline{\mu, \alpha}$) and loading/unloading rates are hard to tell (Figure 5).

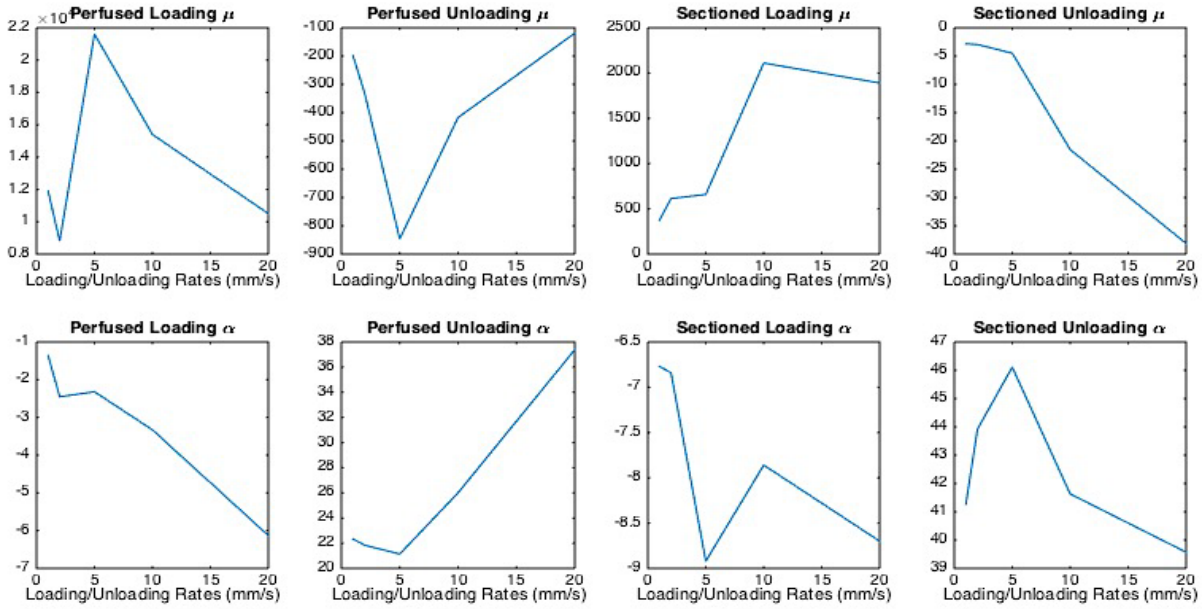

Figure 5 Relationships between parameters (μ, α) and loading/unloading rates on the perfused and sectioned liver samples.

However, we notice from Equation (1) that $\mu \times \alpha$ becomes a new parameter when we take the first derivative of ε and $\alpha \gg 1$. Therefore, we fitted $\mu \times \alpha$ with loading/unloading rate to a quadratic function (Equation (2)) and the results are shown in Figure 6 and Table 2.

$$y = a_2 x^2 + a_1 x + a_0 \qquad (2)$$

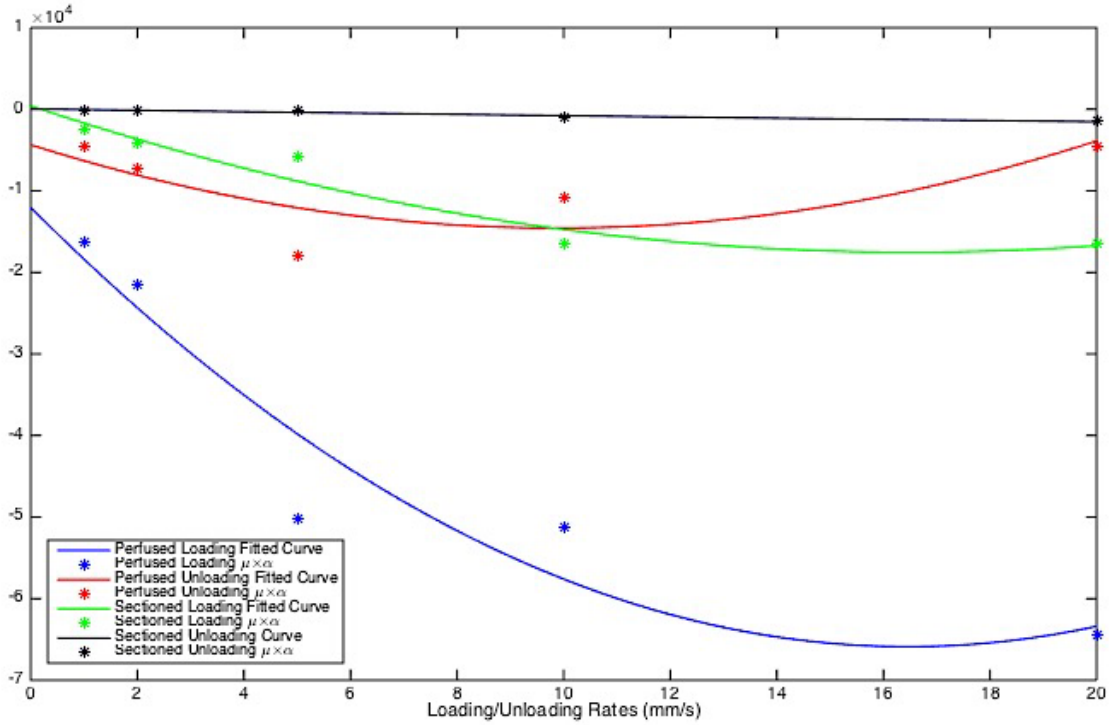

Figure 6 Relationships between the product $(\mu \times \alpha)$ and loading/unloading rates on the perfused and sectioned liver samples.

Table 2 Coefficients in Equation (2) representing the relationships between the product $(\mu \times \alpha)$ and loading/unloading rates on the perfused and sectioned liver samples

Coefficients	Perfused Liver		Sectioned Liver	
	Loading	Unloading	Loading	Unloading
a_2	198.89	104.46	65.78	0.41
a_1	-6545.37	-2065.26	-2172.67	-86.60
a_0	-12042.77	-4357.74	410.55	43.18

Since a limit of energy lost density mush exist for a given loading process, we fitted the energy lost density with loading/unloading rate to a logarithmic function (Equation (3)) and results are shown in Figure 7 and Table 3.

$$y = b_1 \log x + b_0 \quad (3)$$

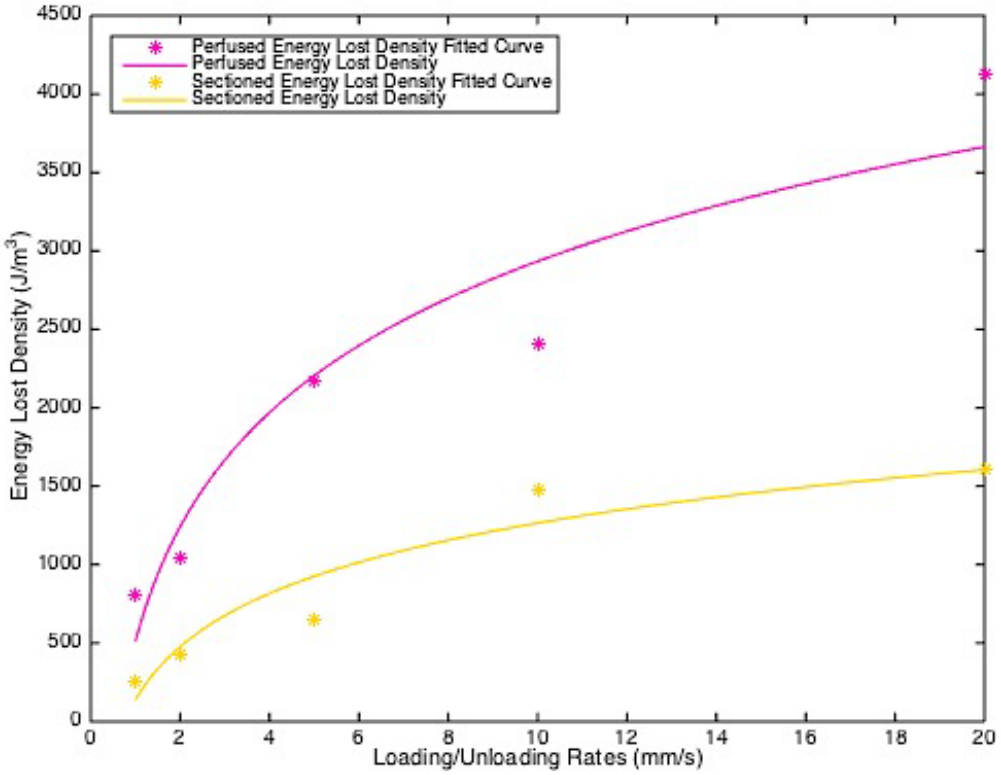

Figure 7 Relationships between the energy lost density and loading/unloading rates on the perfused and sectioned liver samples.

Table 3 Coefficients in Equation (3) representing the relationships between the energy lost density and loading/unloading rates on the perfused and sectioned liver samples.

Coefficients	Perfused Liver	Sectioned Liver
b_1	1052.0	489.9
b_0	511.0	137.0

In stress relaxation testing, the maximum strain was kept at 0.3. Three testing points (e1, e3, and e5) from the edge part of a lobe and three testing points (c1, c3, and c5) from the center part of a lobe (Figure 1) were loaded at 10 mm/s and the change of force was measured for 300 sec. Each testing point was only tested for one time when the liver was perfused and sectioned.

The experimental data of stress relaxation tests of the perfused liver and sectioned liver samples are shown in Figure 8. One thing to note is that some sectioned samples, especially the samples in the center part of the lobe, were too thick (30 mm verses the length of top surface which is 10 mm) to stand stably during the 300-sec measurement period. For this reason, we failed to collect data from those samples.

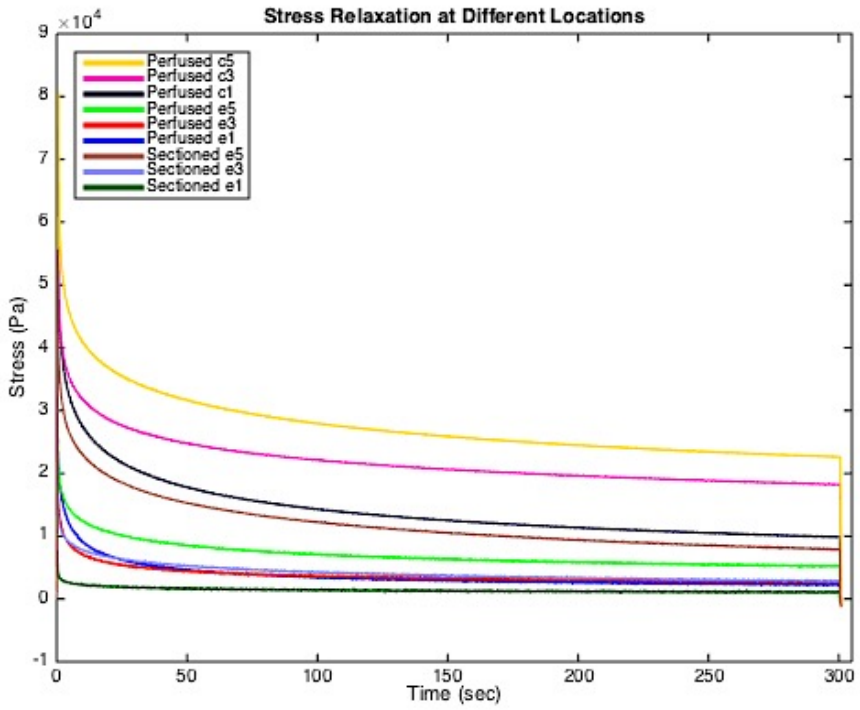

Figure 8 Experimental data of stress relaxation tests at testing points from the center and edge parts of a lobe when the liver was perfused and sectioned.

In creep testing, the maximum force was kept at 0.3 N. Three testing points (e2, e4, and e6) from the edge part of a lobe and three testing points (c2, c4, and c6) from the center part of a lobe (Figure 1) were loaded at 10 mm/s and the change of displacement to maintain the maximum force was

measured for 300 sec. Each testing points was only tested for one time when the liver was perfused and sectioned.

The experimental data of creep tests of the perfused liver and sectioned liver samples are shown in Figure 9. However, some testing points, especially those in the center part of the lobe, were too slippery to hold the probe during the 300-sec period of measurement. Therefore, we failed to collect data from those testing points.

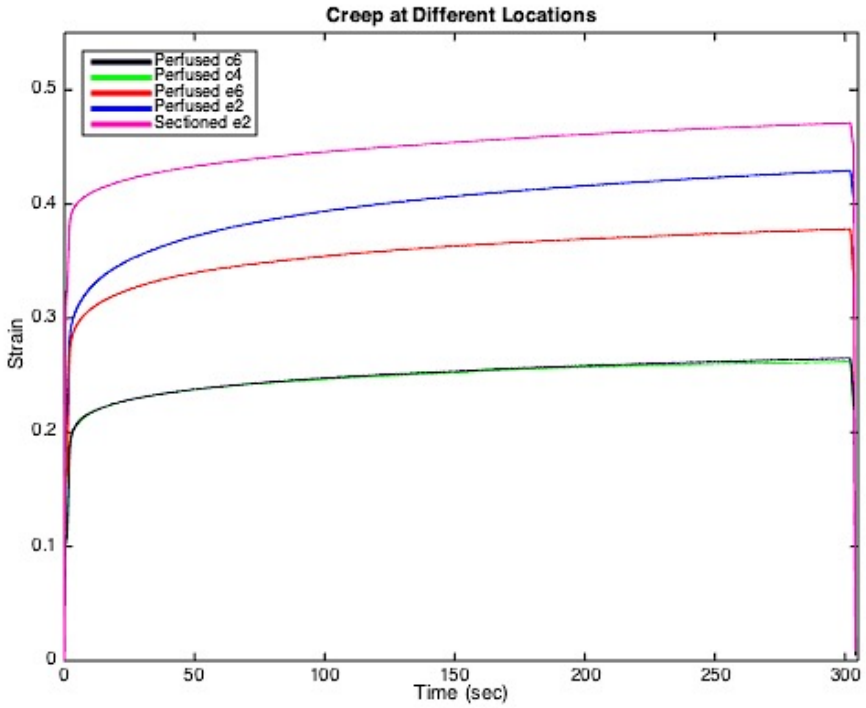

Figure 9 Experimental data of creep tests at testing points from the center and edge parts of a lobe when the liver was perfused and sectioned.

During Q4 of Y2, our work focused on conducting dynamic indentation tests on perfused liver tissue to figure out differences in mechanical properties between different lobes. We are in regular contact with the modeling team to ensure our choice of measurements and methodologies (e.g., tissue sample choice, fixing method, confinement, etc.) satisfy the requirements of the model development team.

A porcine liver consists of 5 lobes (as shown in Figure 1): four large lobes (right lateral lobe, right medial lobe, left medial lobe, and left lateral lobe) and one small lobe (caudate lobe). However, differences in mechanical properties between different lobes of a liver have been rarely reported. To the best of our knowledge, only Mattei et al. mentioned that the bulk compressive modulus (λ) of porcine fresh liver does not change significantly with the sample harvesting site (i.e. different liver lobes) nor between animals from the same slaughterhouse[1]. But they did not show in detail how

they get this conclusion. So, it is still an important factor that should be seriously taken into consideration before any other tests are done on different lobes.

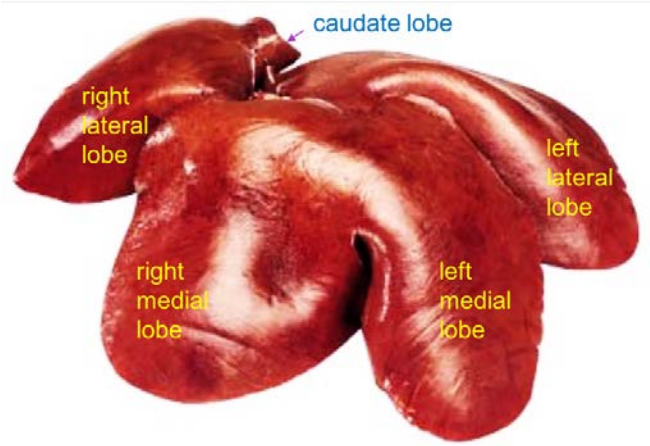

Figure 1 Picture of a porcine liver[2]

A liver, which weighed 0.91 kg, was perfused with 5 liters of 39 ºC normal Plasma-Lyte A Injection solution within 2 hours of removal from a female pig (as shown in Figure 2).

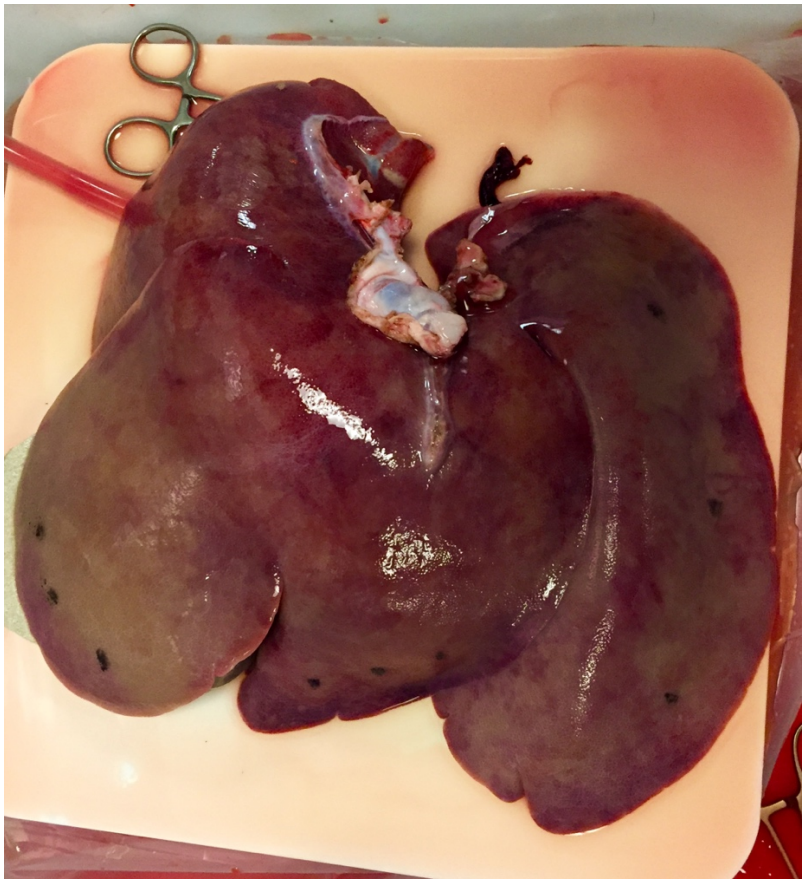

Figure 2 Picture of the perfused liver used in this experiment. Testing points used in indentation tests on different lobes are labeled with black points.

The experiment setup of the perfusion system is the same as we mentioned in the Year 2 Quarter 7 report. A cylindrical indenter with 5 mm diameter was used in all measurements.

In indentation tests on different lobes, the maximum strain was 0.3. Three points were tested at the edge and center part of each lobe. All testing points were loaded/unloaded at 1 mm/s. The sample was immediately unloaded once the displacement reached the maximum value. Each testing location was tested 3 times while the liver was perfused. All testing locations were allowed to recovery for 1 minute before the next measurement.

We took the average of all measurements of all three testing locations on the same part of the same lobe and fitted them to the Ogden model (two constants) (see Year2 Quarter 7 report Equation (1)) with $R^2>0.95$.

The hysteretic stress-strain curves of different lobes of the perfused liver are shown in Figure 3. The material constants and lost energy density of each curve are summarized in Table 1. We can see that the mechanical properties of the edge parts of a liver do not vary much with different lobes. However, mechanical properties of the center parts of a liver do vary a lot between different lobes

since the structures, dimensions, and quantities of vessels varied a lot in the center part of different lobes.

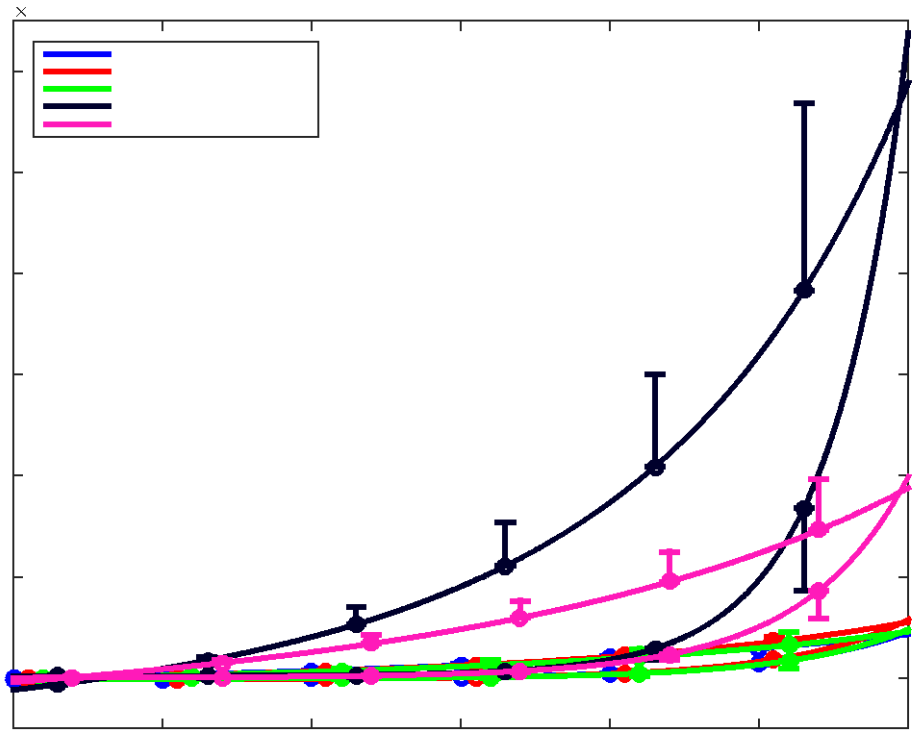

Figure 3 Hysteretic stress-strain curves of indentation tests at different parts of different lobes of a perfused porcine liver.

Table 1 Parameters of the Ogden model representing indentation experimental data and energy lost density of each hysteresis curve.

	Lost Energy Density (J/m^3)	μ	α	$\mu \times \alpha$	c	R^2
Right Medial Lobe, Edge (Loading)	4.76E+02	2.47E+03	-3.12	-7.70E+03	-8.33E+01	1.0000
Right Medial Lobe, Edge (Unloading)		-31.69	29.87	-9.47E+02	-2.86E+02	1.0000
Left Medial Lobe, Edge	4.97E+02	1.34E+03	-5.15	-6.88E+03	-1.58E+02	1.0000

(Loading)						
Left Medial Lobe, Edge (Unloading)		-21.96	33.30	-7.31E+02	-3.32E+02	1.0000
Left Lateral Lobe, Edge (Loading)	4.49E+02	1.56E+03	-4.30	-6.71E+03	-1.39E+02	1.0000
Left Lateral Lobe, Edge (Unloading)		-16.03	34.00	-5.45E+02	-2.20E+02	1.0000
Right Medial Lobe, Center (Loading)	3.90E+03	6.42E+03	-7.27	-4.67E+04	-2.38E+03	1.0000
Right Medial Lobe, Center (Unloading)		-6.94	53.04	-3.68E+02	3.76E+02	1.0000
Left Lateral Lobe, Center (Loading)	1.78E+03	7.89E+03	-3.82	-3.02E+04	-8.39E+02	1.0000
Left Lateral Lobe, Center (Unloading)		-33.10	37.77	-1.25E+03	1.93E+01	1.0000

At the end of the experiment, we measured the liquid volume fraction of the porcine liver, which is required by the modeling team and is useful for developing biphasic constitutive models of liver tissue. The liquid volume fraction is the ratio of the volume of liquid and whole liver (volume of blood and solid liver tissue). We first measured the weight (910 g) of the liver w/o liquid inside when it came. Next, we used surgical clamps to block all main vessels at the end of the perfusion experiment and measured the weight (1640 g) and volume (1500 cc) of the liver w/ liquid and clamps. We loosened the clamps and drained the liquid out of the liver. Then we measured the weight (1208 g) and volume (1250 cc) of liver w/o liquid. The weight of clamps was 79 g. By using all the information mentioned above, we calculated the liquid volume fraction of our porcine liver to be about 44%. One thing to note is that we cannot let the solution inside the innumerable small vessels completely drain without damaging the cells and preventing the liquid inside cells going out. So, the value of the liquid volume fraction is only a rough number.

During Q9, our work focused on conducting compression and tensile tests in a full loading-unloading cycle on perfused liver tissue to characterize viscoelastic properties of liver tissue from hysteretic stress-strain curves. We are in regular contact with the modeling team to ensure our

choice of measurements and methodologies (e.g., tissue sample choice, fixing method, confinement, etc.) satisfy the requirements of the model development team.

The testing instrument (300C Dual Mode Muscle Lever system, Aurora Scientific Inc., Canada) we used in Q3-Q8 reports is only capable of compression with limited load. Thus, we decided to rent an Instron 5544 (ITW Test & Measurement, IL) from Prof. Ajit Mal (Department of Mechanical Engineering, UCLA) to see how liver tissue would behave in a full loading cycle. The Instron 5544 can provide up to 50 N force and its maximum speed reaches 1000 mm/min.

The most challenging part of conducting tensile test on liver tissue is how to properly attach liver tissue to the gripper. For a perfused liver, if the tissue is glued, hooked, or sutured to the gripper, the tissue will rupture when the gripper is removed and the liver is not intact anymore for perfusion. Therefore, we developed vacuum heads, which can be easily removed by turning off the pump, as the connector between tissue and the gripper. We designed cylindrical heads with different internal geometries (as shown in Figure 1) and outer diameters (5, 7, and 10 mm).

Type	Cross		Cylindrical		Modified Cylindrical		Conical	
Outer Diameter (mm)	Max Force (N)	Max Pressure (Pa)	Max Force (N)	Max Pressure (Pa)	Max Force (N)	Max Pressure (Pa)	Max Force (N)	Max Pressure (Pa)
5	0.25	1.0e4	0.70	3.0e4	\	\	0.15	0.7e4
7	0.55	1.4e4	1.20	3.0e4	1.00	2.6e4	\	\
10	1.30	1.6e4	1.30	1.6e4	1.50	1.9e4	\	\

Figure 1 Cylindrical vacuum heads with different internal geometries and outer diameters were tested. The maximum force/pressure they could provide are recorded.

Those vacuum heads were connected to a pump and tested on liver tissue to get the maximum force they could provide by using a force gauge (as shown in Figure 2). The results are shown in Figure 1 and we could see that vacuum heads in “Cross” and “Modified Cylindrical” shapes were good candidates for tensile tests.

To determine which one would be used in the real tests, we developed the lower vacuum head and tested those vacuum heads using the Instron 5544 as shown in Figure 3. Since both the “Cross” and “Modified Cylindrical” heads with 7 mm in diameter are capable of performing tensile tests with 0.3 maximum strain, we finally chose the 7 mm “Cross” head because its suction creates less surface deformation than the other designs.

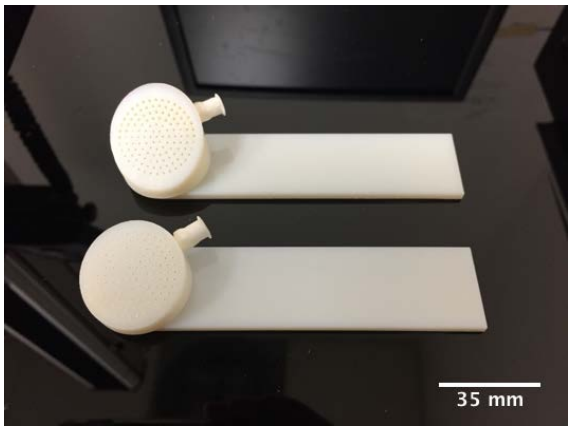

A liver was perfused with 5 liters of 39 ºC normal Plasma-Lyte A Injection solution within 2 hours of removal from a pig. The experimental setup of the perfusion system is the same as described in the Year 3 Quarter 7 report.

Compression and tensile tests were conducted in a full loading-unloading cycle on *ex vivo* perfused liver tissue (subsequently referred to as “perfused”), *ex vivo* sectioned liver tissue immersing in saline solution at room temperature (“wet”), and *ex vivo* sectioned liver which was taken out from saline solution and standing in air for exact 1 minute (“dry”) as shown in Figure 4. Details of experimental methods are shown in Figure 5.

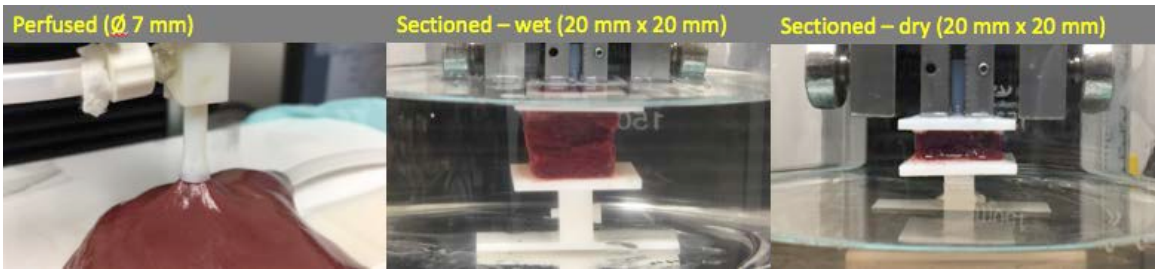

(a) (b) (c)

Figure 4 Pictures of testing setups on (a)perfused, (b)wet, and (c)dry liver tissue.

group	Loading rate (mm/s)	Max strain	Goal	
1	0.2	0.05	Different strain	
2		0.10		
3		0.20		
4		0.30	Different loading rates	
5	1			
6	2			
7	5			
8	10			

Figure 5 Details of experimental methods of a full loading-unloading cycle includes compression and tensile tests in sequence.

The nominal stress is defined as the ratio of the force applied on tissue and the contacted area between tissue and the fixture (the upper vacuum head for “perfused” tissue and rectangular hard plates for “wet” and “dry” tissue). The nominal strain is defined as the ratio of the stretched/compressed thickness and the natural thickness of tissue. The hysteretic stress-strain curves of liver tissue under in all three situations are shown in Figure 6-11.

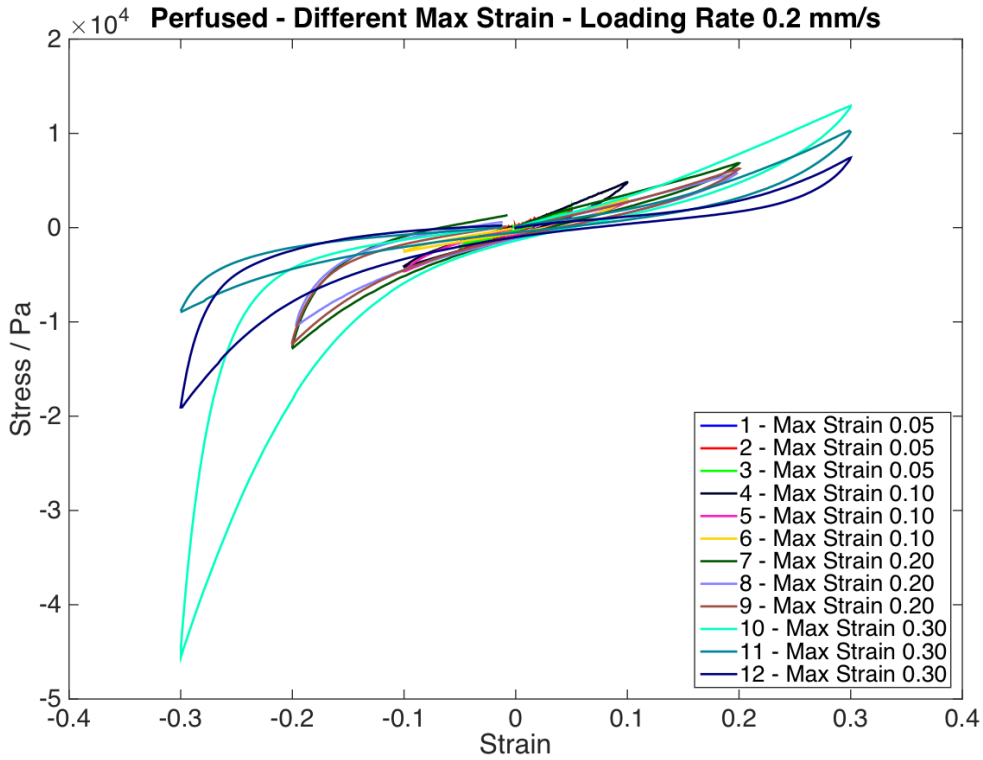

Figure 6 Hysteretic stress-strain curves of perfused liver tissue at different maximum strains.
In Figure 6, curves with the same maximum strain look very different and are not consistent. One reason could be that liver is not perfectly suctioned by the lower head so the edge of liver was swinging up during the stretching process and swinging down when it was compressed.

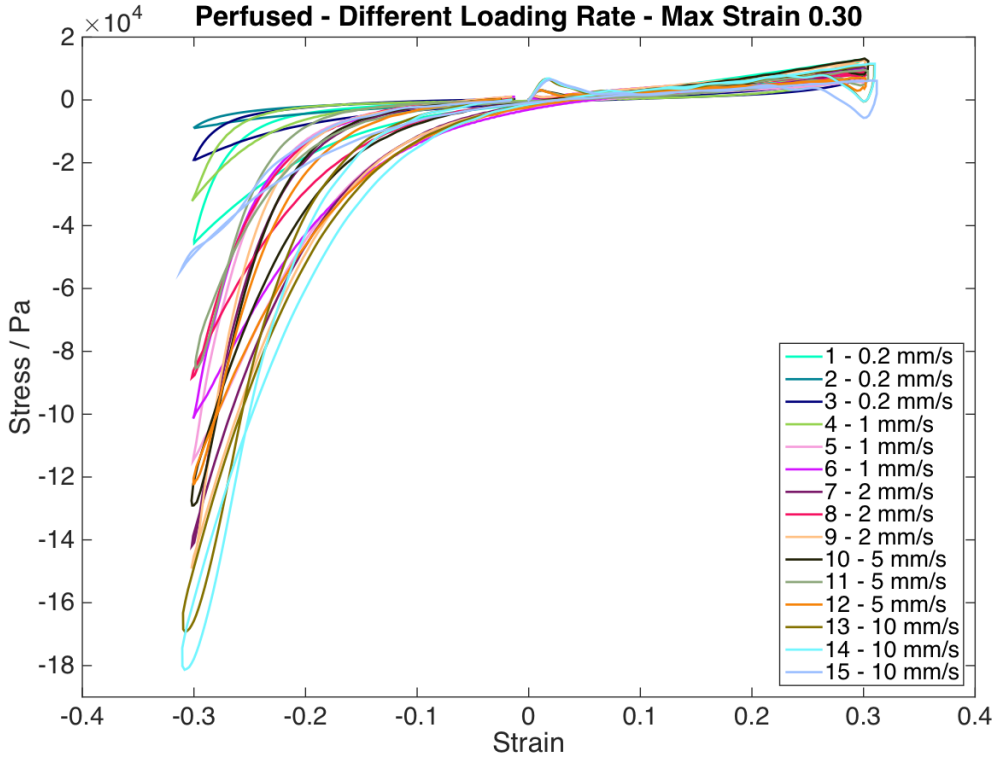

Figure 7 Hysteretic stress-strain curves of perfused liver tissue at different loading rates.
In Figure 7, we can see that curves are still suffering from the same swinging issue as that in Figure 6. A possible solution is to only test center part of the liver lobe which mitigates the motion of thin edges.

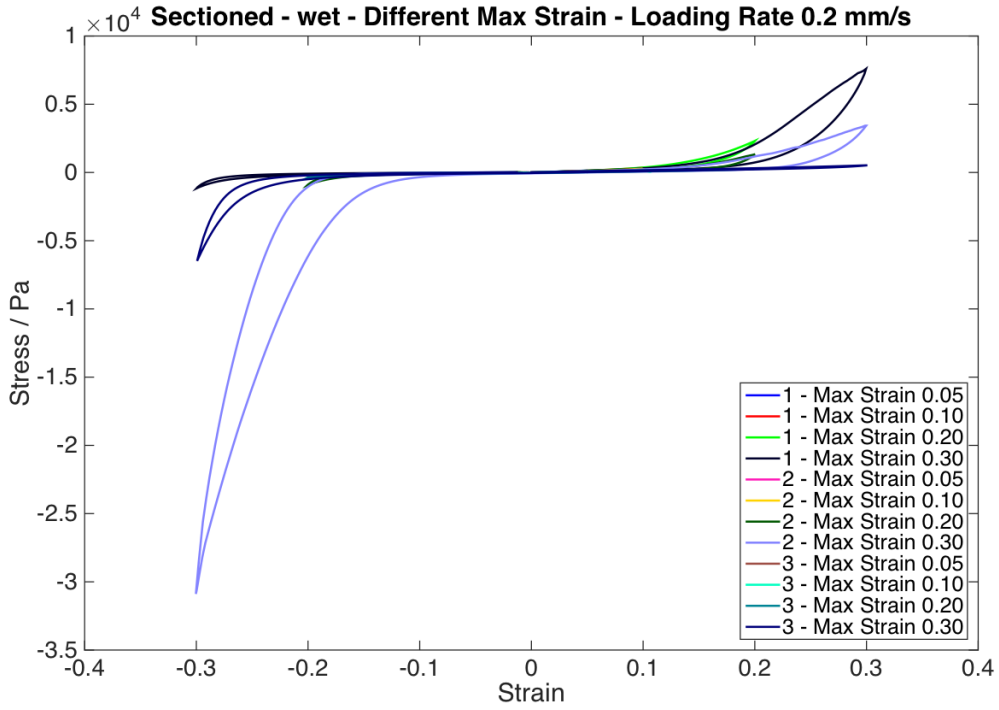

Figure 8 Hysteretic stress-strain curves of sectioned-wet liver tissue at different maximum strains.

In Figure 8, we measured the wet natural thickness of tissue when it was immersing in the saline solution. The inconsistency of the curves among different samples was caused by different stretching state of tissue in liquid due to their different biological structure. Those tissue with larger internal vessels were stretched more in their natural wet state, which means more tension and less compression forces were required during the loading/unloading process. However, results are consistent for each sample and larger strain provided larger stress.

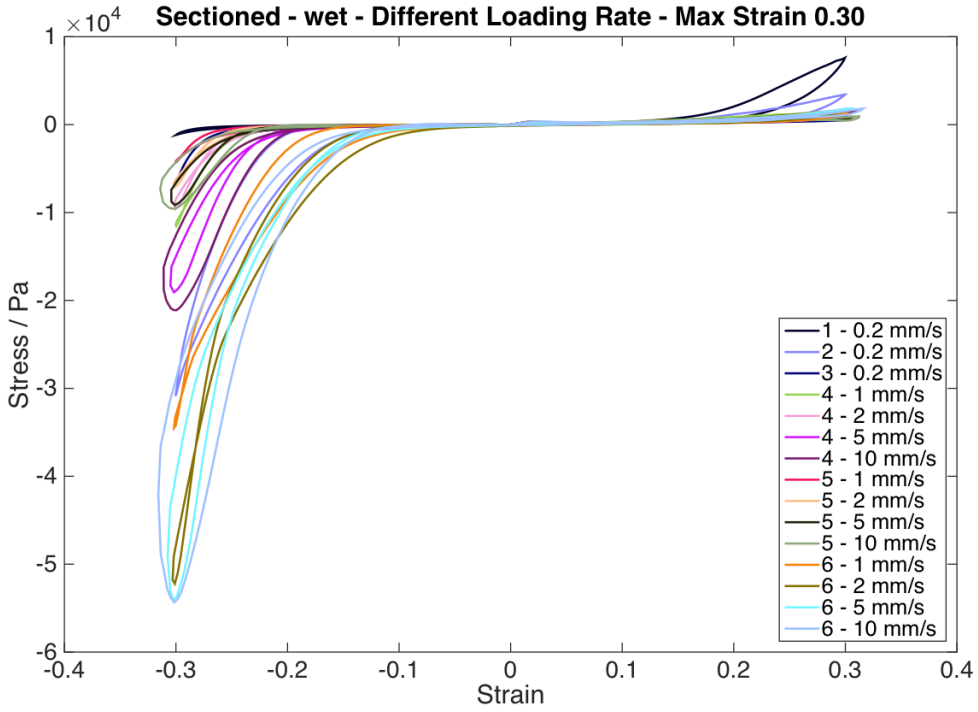

Figure 9 Hysteretic stress-strain curves of sectioned-wet liver tissue at different loading rates.

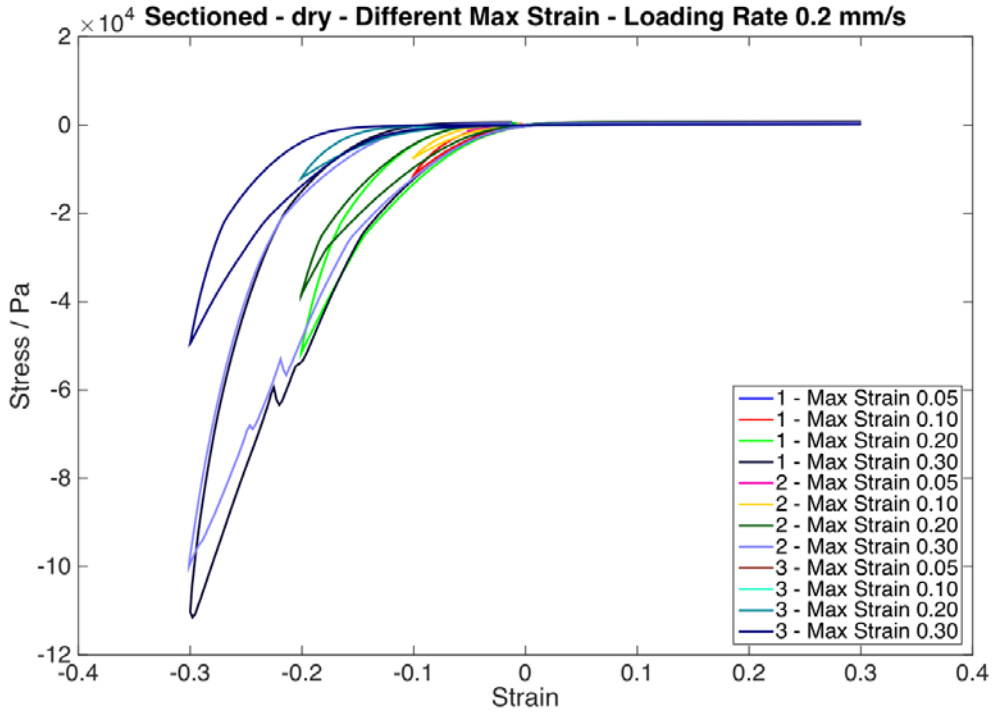

Figure 10 Hysteretic stress-strain curves of sectioned-dry liver tissue at different maximum strains.

In Figure 10, the inconsistency of curves among different samples are also shown here. One thing to note is that some curves are not smooth due to bubbles coming out during the tests. These curves are as expected in that the loading curves of different maximum strains are overlapping.

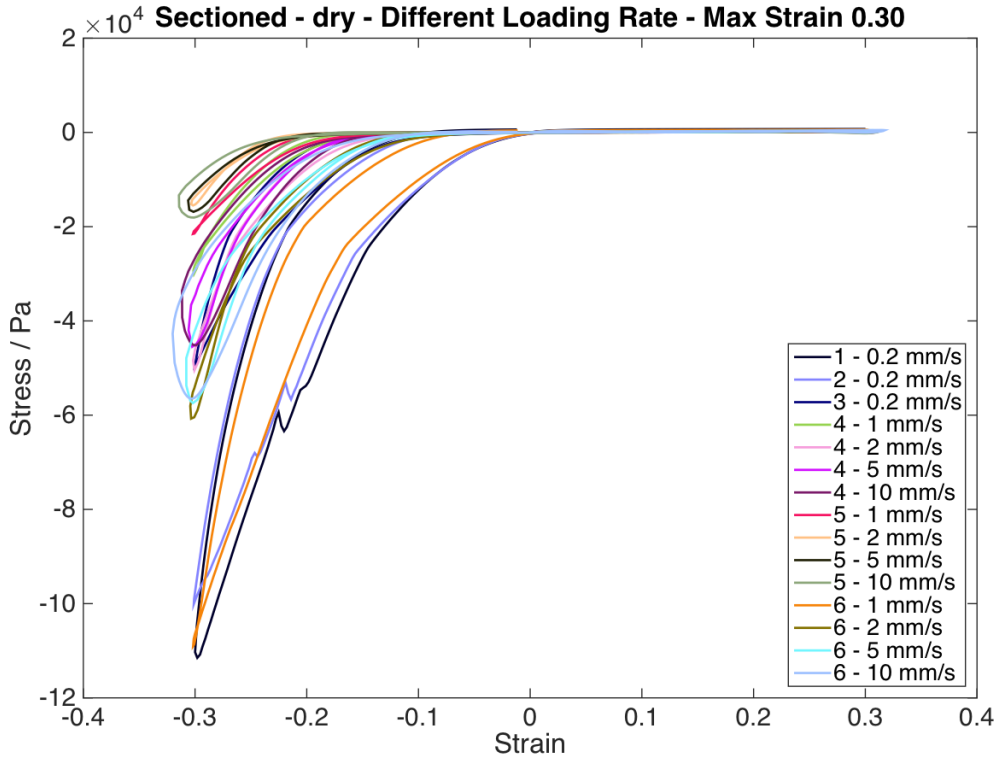

Figure 11 Hysteretic stress-strain curves of sectioned-dry liver tissue at different loading rates.

During Q10, our work focused on developing visco-hyperelastic constitutive models to describe experimental data in Year 1 Quarter 6 Report. We are in regular contact with the entire team to ensure our proposed model, methodologies, and results satisfy the requirements of publishing a paper in Journal of the Mechanical Behavior of Biomedical Materials.

For uniaxial compression tests, the true elastic moduli E is directly calculated from stress $\sigma = \frac{F}{A}$ and strain ε data, where F is the tensile or compressive load and A is the cross-sectional area of the sample. For indentation test, the "effective" (or "reduced") modulus E^* is obtained from load F_{ind} and displacement x_{ind} data with the assistance of the Sneddon model [1, 2], which has been reported to demonstrate satisfactory performance under both small strain (2.5 - 7.5%) and large strain (15 - 20%) range by Delaine-Smith et al. The relationship of load-displacement and equivalent stress-strain is defined as

$$E^* = \frac{d\sigma}{d\varepsilon} = \frac{1}{\beta} \times \frac{dF_{ind}}{dx_{ind}} \times \frac{1}{2} \times \frac{\sqrt{\pi}}{\sqrt{A_{contact}}} \qquad (1)$$

where β is a geometrical constant of the indenter and is 1 for a flat-ended type, $A_{contact} = \pi r^2$ is the contacted area for a flat circular head with radius of r. Therefore Eq. (1) is simplified to

$$\frac{d\sigma}{d\varepsilon} = \frac{1}{2r} \times \frac{dF_{ind}}{dx_{ind}} \tag{2}$$

One of the well-known hyperelastic constitutive models is the Ogden model [4] which has been widely applied to nonlinear rubber-like tissue modeling for a large range of deformations. Its strain energy function W is written as

$$W = \sum_{i=1}^{N} \frac{\mu_i}{\alpha_i} \left(\lambda_1^{\alpha_i} + \lambda_2^{\alpha_i} + \lambda_3^{\alpha_i} - 3 \right) \tag{3}$$

where μ and α_i are experimentally defined material constants and $\lambda_i = \alpha_i + 1$ is the stretch ratio in the same direction of the principal strain ε_i.

Another widely used hyperelastic model is the Mooney-Rivlin model [5, 6] which predicts the behavior of non-linear incompressible isotropic materials, including soft biological tissues such as liver, spleen, kidney, brain, and eye. The two-constant version of the Mooney-Rivlin strain energy function W can be written as

$$W = C_{10}(I_1 - 3) + C_{01}(I_2 - 3) \tag{4}$$

where C_{10} and C_{01} are two non-negative material constants, I_1 and I_2 are invariants of the Cauchy-Green deformation tensor.

$$\begin{aligned} I_1 &= \lambda_1^2 + \lambda_2^2 + \lambda_3^2 \\ I_2 &= \lambda_1^2\lambda_2^2 + \lambda_2^2\lambda_3^2 + \lambda_3^2\lambda_1^2 \end{aligned} \tag{5}$$

When $C_{01} = 0$, Eq. (4) becomes a neo-Hookean model.

$$W = C_{10}(I_1 - 3) \tag{6}$$

In fact, the Mooney-Rivlin model and the neo-Hookean model can be derived from the Ogden model. Eq. (4) and Eq. (6) can be obtained from Eq. (3) by substituting Eq. (5) and setting $N = 2, \alpha_1 = 2, \alpha_2 = -2$ and $N = 1, \alpha_1 = 2$ correspondingly.

The engineering stress s_i (force per underformed area) of incompressible material in the tensile or compressive direction [7] can be calculated by

$$s_i = \frac{\sigma_i}{\lambda_i} = -\frac{p}{\lambda_i} + \frac{\partial W}{\partial \lambda_i} \tag{7}$$

where p is the hydrostatic pressure and $\lambda_1\lambda_2\lambda_3 = 1$ for incompressible materials. By comparing the experimentally obtained stress-strain curves with theoretical curves from Eq. (7) implementing Eq. (3)(4)(6), we can determine the strain energy function that best describes the mechanical properties of porcine liver tissue. Thus the stress-strain relationships for the Ogden, Mooney-Rivlin, and neo-Hookean models describing uniaxial compression ($\lambda_1 = \lambda, \lambda_2 = \lambda_3 = \lambda^{-1/2}, \sigma_2 = \sigma_3 = 0$) are given by Eq. (8)(9)(10) respectively. N = 1 is used for the Ogden model in the following part of this article.

$$s_1 = \sum_{i=1}^{N} \mu_i \left((1+\varepsilon)^{\alpha_i - 1} - (1+\varepsilon)^{-\frac{1}{2}\alpha_i - 1} \right) \tag{8}$$

$$s_1 = 2C_{10}\left[(1+\varepsilon) - \frac{1}{(1+\varepsilon)^2} \right] + 2C_{01}\left[1 - \frac{1}{(1+\varepsilon)^3} \right] \tag{9}$$

$$s_1 = 2C_{10}\left[(1+\varepsilon) - \frac{1}{(1+\varepsilon)^2} \right] \tag{10}$$

1.1.1 Linear viscoelastic constitutive models

To estimate the impact of time/rate-dependency on tissue behavior, viscoelastic constitutive models should be considered. The viscoelastic properties of soft tissue can be explained by three mechanisms [8]: 1) the significant flow of fluid goes through the fibrous solid matrix during deformation; 2) the existence of temporary matrix connections between large molecules (such as protein, sugar, and collagen) that varies between loading and unloading conditions; 3) the intrinsic time-dependent nature of solid matrix.

The most widely used linear viscoelastic models are the Maxwell model and the Kelvin-Voigt model as shown in Figure 1. Both of them consist of combinations of linear springs with spring constant μ and dashpots with viscosity constant η. The governing equations of those models are [9]

$$
\begin{aligned}
Maxwell\ model: &\qquad \dot{\varepsilon} = \frac{\dot{\sigma}}{\mu} + \frac{\sigma}{\eta}, \\
Kelvin - Voigt\ model: &\qquad \sigma = \mu\varepsilon + \eta\dot{\varepsilon},
\end{aligned}
\tag{11}
$$

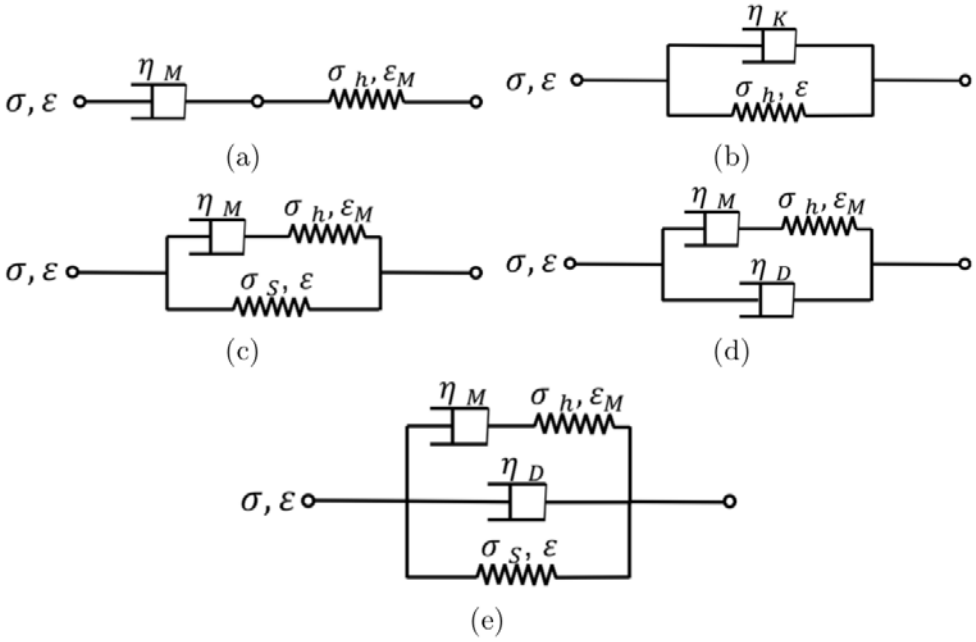

Figure 1: Schematics of visco-hyperelastic constitute models. (a) Maxwell, (b) Kelvin-Voigt, (c) Maxwell/Spring, (d) Maxwell/Damper, (e) Maxwell/Kelvin.

1.1.2 Visco-hyperelastic constitutive models

For uniaxial finite deformation (ε>0.2%) which is common for soft tissue, those linear viscoelastic models are no more applicable. To solve this problem, we substituted all linear springs in linear viscoelastic models described in section 1.1.3 with hyperelastic models in section 1.1.2. Those models are referred to as "visco-hyperelastic constitutive models" and the governing equations of those models are

$$
\begin{aligned}
Viscohyper\ Maxwell\ model: &\qquad \dot{\varepsilon} = \dot{\varepsilon}_M + \frac{\sigma_M(\varepsilon_M)}{\eta_M}, \\
Viscohyper\ Kelvin - Voigt\ model: &\qquad \sigma = \sigma_K(\varepsilon) + \eta_K\dot{\varepsilon},
\end{aligned}
\tag{12}
$$

where ε_M is the strain of hyperelastic spring in Maxwell model and $\sigma_X(\varepsilon_Y)$ is the stress of hyperelastic spring in viscoelastic model *X* with strain ε_Y. Similarly, other visco-hyperelastic models (as shown in Figure 1) can be obtained by putting a hyperelastic spring or/and a damper in parallel with a Maxwell model. And the total stress σ caused by uniaxial compression/tension can be written as

$$
\begin{aligned}
Viscohyper\ Maxwell\ model: &\quad \sigma = \sigma_M(\varepsilon_M), \\
Viscohyper\ Kelvin-Voigt\ model: &\quad \sigma = \sigma_K(\varepsilon) + \eta_K\dot{\varepsilon}, \\
Viscohyper\ Maxwell/Spring\ model: &\quad \sigma = \sigma_M(\varepsilon_M) + \sigma_S(\varepsilon), \\
Viscohyper\ Maxwell/Damper\ model: &\quad \sigma = \sigma_M(\varepsilon_M) + \eta_D\dot{\varepsilon}, \\
Viscohyper\ Maxwell/Kelvin\ model: &\quad \sigma = \sigma_M(\varepsilon_M) + \sigma_K(\varepsilon) + \eta_K\dot{\varepsilon},
\end{aligned}
\tag{13}
$$

1.2. Results

Indentations with larger maximum strains resulted in more nonlinear force -displacement curves with larger energy loss. Thus, fitting to data obtained from dynamic indentation tests was more challenging compared to that of quasi-linear tests. In section 1.1, 15 visco-hyperelastic models from the combination of 5 viscoelastic models and 3 hyperelastic models were introduced. To determine which model fits the experimental data best, the average converted stress-strain curve of all three dynamic perfused indentations at a testing point and its fitted curves using all 15 visco-hyperelastic models. Implementing the Ogden model into the Maxwell/
Kelvin model (Figure 1(e)) turns out to fit the hysteretic stress-strain curves best as shown in the Figure 2. Thus, M/K(O) model is chosen to describe the mechanical properties of a perfused liver in dynamic indentation tests (max strain = 0.30). Likewise, M/K(O) model is also the most appropriate model for sectioned liver samples with large maximum strain (0.30) and quasi-static indentation tests (with or without perfusion, max strain = 0.05).

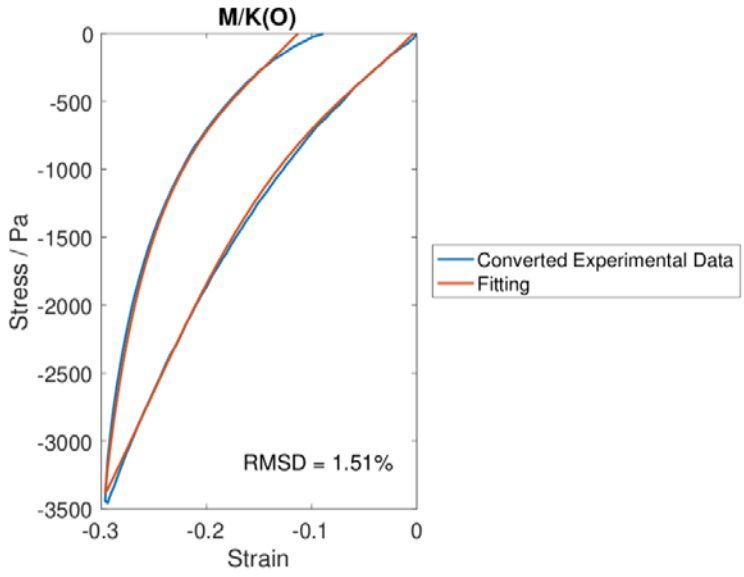

Figure 2: The nominal stress-strain experimental data and the fitted curve of the Maxwell/Kelvin visco-hyperelastic constitutive model (Figure 1(e)) at a certain testing point of a perfused liver. M - Maxwell model. K - Kelvin-Voigt model. "/" - in parallel. O - Ogden model. RMSD - Root-mean-square standard deviation.

1.2.1 Indentation at Different Locations w/ Maximum Strain = 0.05

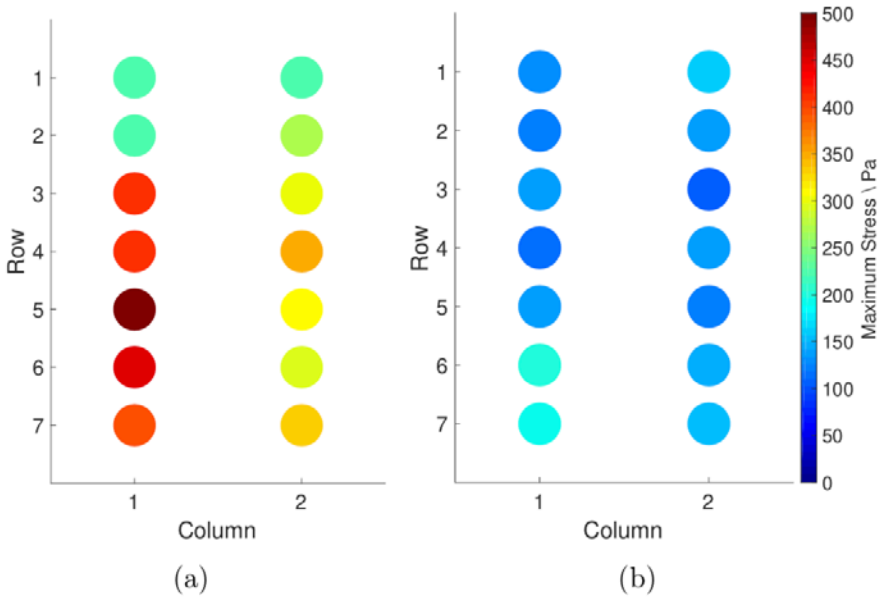

Figure 3: The maximum stress of indentation tests at different locations on (a) a perfused liver and (b) sectioned liver samples.

As shown in Figure 3, liver tissue with perfusion has larger maximum stress and was stiffer than unperfused liver tissue. Liver tissue consists of hepatic lobules, which is typically a hexagonal block of hepatocytes around a center portal vein and its capillary branches separated by portal triads and connective tissue. All vessels of a perfused liver were filled with incompressible fluid which made the tissue stiffer. Figure 4 shows the average percentages of the recovered and dissipated energy density (J/m^3) as shown by the left and right parts of each bar and the whole energy density as described by the color of each bar. The percentages of dissipated energy of perfused tissue are smaller than that of unperfused liver. Thus, the unperfused liver tissue is more viscous than tissue with perfusion. Significant differences of the total energy stored during the loading process between different locations are likely caused by variable vascularity of liver tissue at different locations.

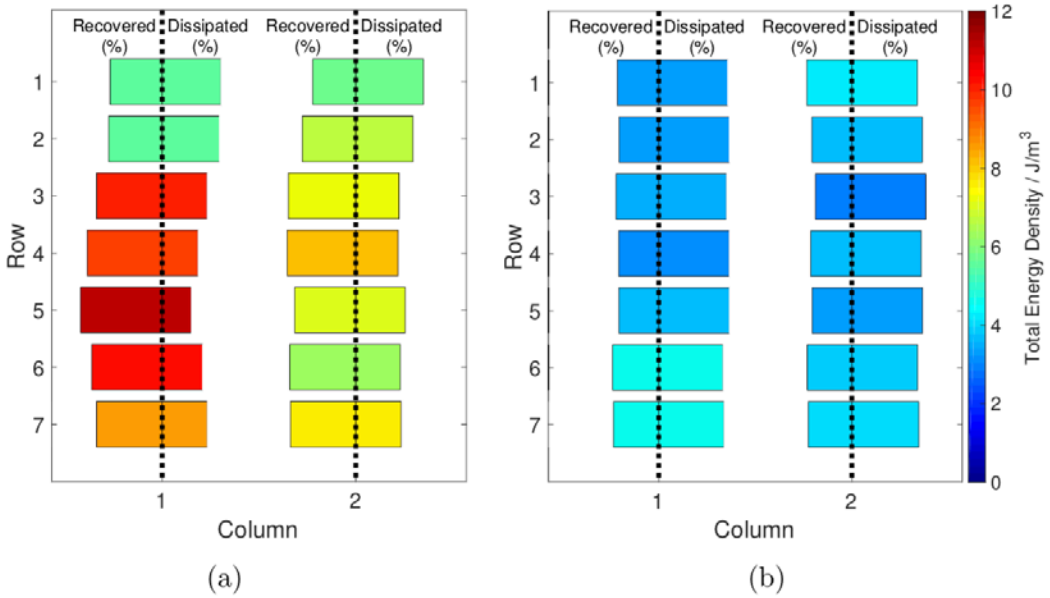

Figure 4: The energy density applied in indentation tests at different locations on (a) a perfused liver and (b) sectioned liver samples. The left and right parts of each bar indicate the percentages of the recovered and dissipated energy of liver tissue, respectively, in the indentation tests. The color of each bar describes the total energy stored during the loading process.

1.2.2 Indentation at Different Strain Rates w/ Maximum Strain = 0.30

Fitted curves of the average results of indentation tests at different loading rates on a liver lobe in two conditions are shown in Figure 5 (a) and (b). In both cases, RMSD is less than 4% for all curves.

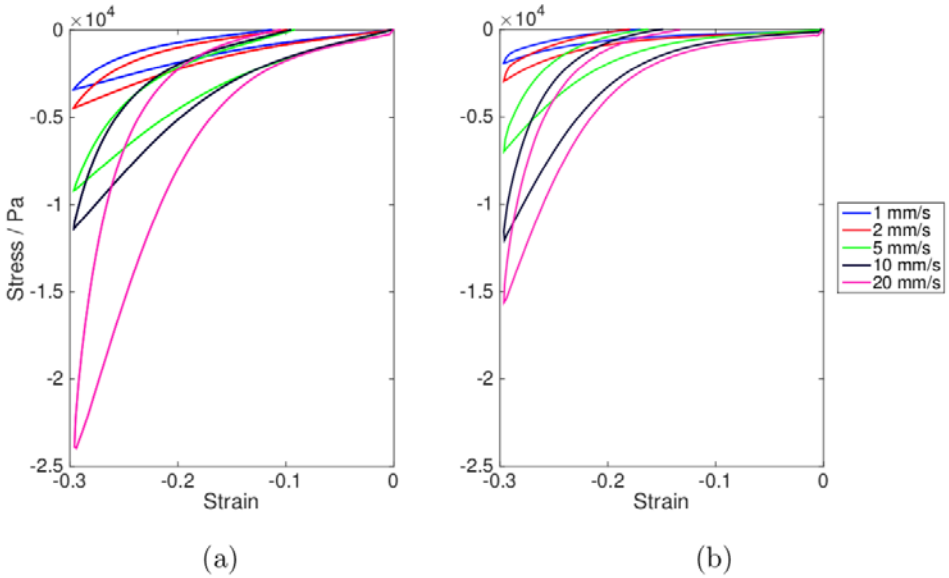

Figure 5: The fitted nominal stress-strain curves of indentation tests at different loading/unloading rates on (a) a perfused liver and (b) sectioned liver samples.

As shown in Figure 5, higher loading/unloading rate makes the liver tissue stiffer and more viscous. It demonstrated the viscous nature of the liver tissue (i.e., it can be significantly affected by different loading rates).

During Q11, our work focused on revising the manuscript based on the feedbacks from the reviewers of Journal of the Mechanical Behavior of Biomedical Materials. We are in regular contact with the entire team to ensure we considered the reviewers' comments carefully.

Selected questions and their answers are listed below.

Q1: "***In the literature, more advanced models describing both viscoelastic and hyperelastic behavior (in a wider viscoelastic spectrum) were already characterized using the same material constants for all measurements (not different set of material coefficients for each curve) was done in Ayyildiz et al. So, what is the research problem (gap in the literature) that the author attack in this study? In other words, what are the novelty and the technical contribution in this study considering that there are already many studies investigated the visco-hyperelastic behavior of the liver***?"

A1: The research problems (gap in the literature) that we tried to attack in this study are: 1) "all of the visco-hyperelastic models mentioned above were characterized on *ex vivo* sectioned liver samples due to the requirements and limitations of using a rheometer or performing uniaxial compression tests" and "it has been shown that mechanical properties of the liver, following harvesting from the abdominal cavity, changed dramatically when perfusion ceased" [1]; 2) "while prior studies have described the behavior of liver tissue during the loading status (in elongation, compression, or indentation tests) or unloading status (in stress relaxation or creep tests), a hysteresis curve with both loading and unloading processes was incompletely defined" as shown in Figure 1.

The novelty and the technical contribution in this study are: 1) we seek to use a single material model to characterize the mechanical properties of liver tissue in a FULL indentation cycle; 2) based on indentation measurements taken from ex-vivo PERFUSED porcine livers, we converted force-displacement curves to stress-strain curves and developed a visco-hyperelastic constitutive model to characterize the liver's mechanical behavior at different locations under various rates of indentation (1, 2, 5, 10, and 20 mm/s).

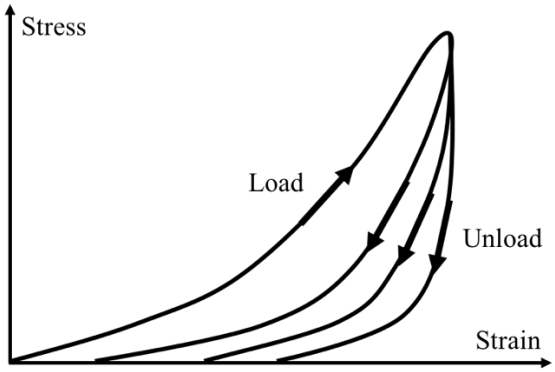

Figure 1 Representative hysteresis curves of different soft biological materials with the same loading behavior but different unloading behaviors.

Q2: "***In the modeling, why the same set of material coefficients are not sufficient to characterize all material behavior obtained at different loading rates?***"

A2: After thinking through the question carefully, I think there are three main reasons: 1) liver tissue is strain-stiffening (or strain-hardening) and moduli are much higher when loading rate increases or liver is perfused; 2) using the same set of material coefficients are sufficient when ONLY loading or unloading process is described or the large error is acceptable at large loading rates; 3) the material coefficients themselves should vary with time like the model proposed by Vemaganti and Roan [2].

In our study, the perfused liver tissue is 1.5 times stiffer than the sectioned liver tissue at a loading rate of 20 mm/s. And BOTH the loading and unloading processes were described simultaneously using a single model. We tried to shrink the number of variables and let the least number (2 of 6) of material parameters change with time/strain rate.

It is worth noting that the M/K(O) model uses the most complicated model among the viscoelastic models shown in Figure 1 in Year 3 Quarter 10 Report and it has 6 material parameters. Those 6 model coefficients cannot be uniquely obtained by numerically fitting the model to the experimental data sets, which means different sets of coefficients can fit the measured stress-strain hysteresis curve with comparable errors when the numerical fitting started at predefined different sets of initial values (as shown in Table 1). Thus, a strategy was proposed to find the reasonable sets of initial values: 1) uniquely locate the α_{K0} and μ_{K0} of the K(O) by numerical fitting and letting $\eta_{K0} = 0$ (Figure 2 (a)); 2) use α_{K0} and μ_{K0} as initial values in the fitting to obtain the α_{K1}, μ_{K1}, and η_{K1} (Figure 2 (b)); 3) use the numbers from the previous step as initial values and find two of M(O) parameter set α_{K2}, μ_{K2}, and η_{K2} by letting the third one as a constant (Figure 2 (c). The K(O) was chosen in step (1) as a base for the following fitting steps because M/K(O) consists of K(O) and M(O) in parallel and K(O) has a more similar shape than M(O).

Table 1: Two sets of coefficients (1e3) of the M/K(O) model for dynamic indentation tests at different loading/unloading rates show comparable errors (RMSD).

Rate (mm/s)	Perfused Set #1						
	α_M	μ_M	η_M	α_K	μ_K	η_K	RMSD(%)
1	0.010	1.000	7.069	0.010	0.409	3.000	3.09%
2	0.010	1.000	2.022	0.010	0.577	3.000	2.47%
5	0.010	1.000	1.171	0.010	1.168	3.000	2.87%
10	0.010	1.000	0.045	0.010	1.450	3.000	5.10%
20	0.010	1.000	0.022	0.010	2.634	3.000	8.03%

Rate (mm/s)	Perfused Set #2						
	α_M	μ_M	η_M	α_K	μ_K	η_K	RMSD(%)
1	0.005	1.000	66.000	0.015	0.075	1.500	4.97%
2	0.005	1.000	35.881	0.015	0.131	1.500	3.92%
5	0.005	1.000	14.858	0.015	0.399	1.500	4.90%
10	0.005	1.000	12.252	0.015	0.470	1.500	4.61%
20	0.005	1.000	0.450	0.015	1.113	1.500	6.37%

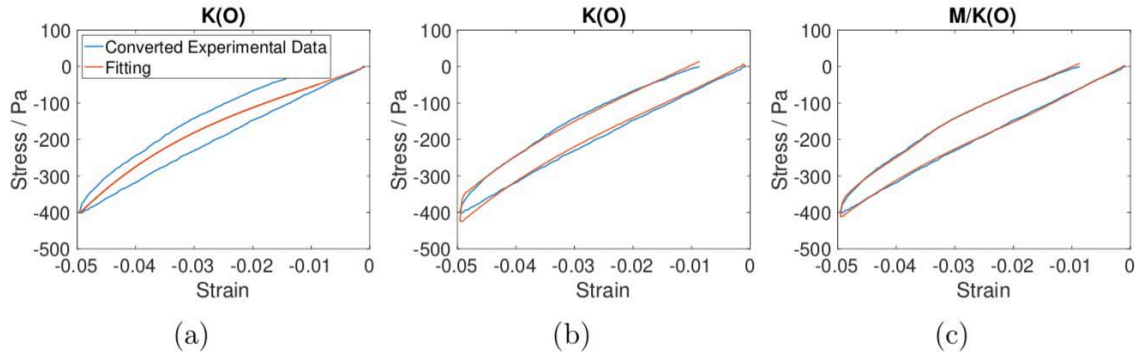

(a) (b) (c)

Figure 2: A strategy to find the 6 coefficients of the M/K(O) model to fit the nominal stress-strain experimental data. M - Maxwell model. K - Kelvin-Voigt model. "/" - in parallel. O - Ogden model. (a) let ηK0 = 0, obtained αK0 = 71.5, μK0 = 63.1; (b) fitted αK1 = 52.7, μK1 = 112.6, and ηK1 = 4067.1; (c) let μM = 1.0, fitted αK2 = 53.0, μK2 = 102.4, ηK2 = 2374.2, αM = 543.5, and ηM = 2526.3.

And the fitted coefficients of all experimental data reported in Year 3 Quarter 10 report are listed in Table 2 and 3.

Table 2: Coefficients (1e3) of the M/K(O) model for dynamic indentation tests at different loading/unloading rates.

Perfused, x - Strain Rate $(/s)$							
Set#	α_M	μ_M	η_M	α_K	μ_K	η_K	RMSD(%)
1	0.01	1	$0.0224x^{-2.036}$, $R^2 = 0.93$	0.01	$2.254x+0.391$, $R^2 = 0.98$	3	<9%
2	0.01	1	$0.0217x^{-2.079}$, $R^2 = 0.94$	$0.004ln(x)+0.016$, $R^2 = 0.98$	1	3	<7%
3	0.01	1	1	$0.003ln(x)+0.015$, $R^2 = 0.96$	1	$1.358x^{-0.582}$, $R^2 = 0.90$	<6%
4	$0.0001x^{-2.457}$, $R^2 = 0.89$	1	1	$0.004ln(x)+0.016$, $R^2 = 0.97$	1	3	<10%
5	0.01	$0.013x^{-2.359}$, $R^2 = 0.84$	1	$0.004ln(x)+0.016$, $R^2 = 0.97$	1	3	<10%

Sectioned, x - Strain Rate $(/s)$							
Set#	α_M	μ_M	η_M	α_K	μ_K	η_K	RMSD(%)
1	$-0.0183x^2$ $+0.0344x$ $+0.0392$, $R^2 = 0.94$	$-0.0041x^2$ $+0.0075x$ $+0.0002$, $R^2 = 0.99$	0.002	20	0.001	$-4.754x^2$ $+10.932x$ -0.144, $R^2 = 1.00$	1	<7%
2	0.05			$-0.0015x^2$ $+0.0036x$ -0.0001, $R^2 = 1.00$		3	1	<7%
3	0.05	0.002	$-22.417x^2$ $+50.236x$ $+6.787$, $R^2 = 0.98$	$-0.0018x^2$ $+0.004x$ -0.0001, $R^2 = 1.00$		3	1	<6%
4	0.05	0.002	20	$-0.0027x^2$ $+0.0057x$ -0.0005, $R^2 = 1.00$		3	$-2.600x^2$ $+4.349x$ -0.324, $R^2 = 0.92$	<8%
5	0.05	0.002	20	0.001	$-7.547x^2$ $+16.193x$ -1.372, $R^2 = 1.00$	$-2.609x^2$ $+4.364x$ -0.323, $R^2 = 0.92$		<8%

Table 3: Coefficients (×1e3) of the M/K(O) model for quasi-static indentation tests at different locations.

Thickness (mm)	Strain Rate (/s)	Location	Perfused						
			α_M	μ_M	η_M	α_K	μ_K	η_K	RMSD(%)
28	0.007	(5,1)	0.6	0.001	3.186	0.05	0.131	2.22	1.43%
25	0.008	(6,1)	0.6	0.001	5.002	0.05	0.114	2.22	1.56%
23	0.009	(4,1)	0.6	0.001	2.756	0.05	0.109	2.22	1.04%
23	0.009	(7,1)	0.6	0.001	3.428	0.05	0.097	2.22	2.85%
20	0.010	(2,1)	0.6	0.001	1.994	0.05	0.065	2.22	1.45%
20	0.010	(2,2)	0.6	0.001	2.559	0.05	0.072	2.22	2.21%
20	0.010	(3,2)	0.6	0.001	3.226	0.05	0.101	2.22	1.58%
17	0.012	(5,2)	0.6	0.001	1.632	0.05	0.085	2.22	1.68%
16	0.013	(6,2)	0.6	0.001	0.536	0.05	0.082	2.22	2.24%
15	0.013	(7,2)	0.6	0.001	1.086	0.05	0.097	2.22	2.13%
14	0.014	(1,1)	0.6	0.001	0.950	0.05	0.074	2.22	3.98%
14	0.014	(1,2)	0.6	0.001	1.329	0.05	0.067	2.22	4.40%
14	0.014	(3,3)	0.6	0.001	0.344	0.05	0.090	2.22	2.61%
14	0.014	(4,2)	0.6	0.001	0.648	0.05	0.101	2.22	3.86%
l_0	$x = 0.2/l_0$		$\eta_M = -461.44x + 7.232$, $R^2 = 0.78$				$\mu_K = -4.061x + 0.137$, $R^2 = 0.31$		

Thickness (mm)	Strain Rate (/s)	Location	Sectioned						
			α_M	μ_M	η_M	α_K	μ_K	η_K	RMSD(%)
24	0.008	(4,1)	0.67	0.001	2.447	0.05	0.0289	1	2.82%
24	0.008	(5,1)	0.67	0.001	3.005	0.05	0.0331	1	3.69%
22	0.009	(3,2)	0.67	0.001	2.394	0.05	0.0332	1	2.20%
22	0.009	(6,1)	0.67	0.001	3.602	0.05	0.0444	1	4.66%
19	0.011	(2,1)	0.67	0.001	1.911	0.05	0.0324	1	3.07%
17	0.012	(7,1)	0.67	0.001	2.388	0.05	0.0469	1	2.71%
16	0.013	(2,2)	0.67	0.001	1.833	0.05	0.0369	1	2.46%
15	0.013	(6,2)	0.67	0.001	1.506	0.05	0.0401	1	3.07%
13	0.015	(1,1)	0.67	0.001	1.001	0.05	0.0373	1	3.67%
13	0.015	(1,2)	0.67	0.001	1.484	0.05	0.0456	1	3.55%
13	0.015	(3,3)	0.67	0.001	0.868	0.05	0.0323	1	4.57%
13	0.015	(4,2)	0.67	0.001	1.240	0.05	0.0382	1	3.19%
13	0.015	(5,2)	0.67	0.001	1.072	0.05	0.0361	1	4.52%
13	0.015	(7,2)	0.67	0.001	1.345	0.05	0.0434	1	3.00%
l_0	$x = 0.2/l_0$		$\eta_M = -245.41x + 4.936$, R^2 220.80				$\mu_K = 0.649x + 0.0296$, $R^2 = 0.12$		

5. Body habitus graphical and physical modeling

During Q1 of Y1, activity was coordinated with Tao Zhou and Chenfanfu Jiang.

During Q2 of Y1, the group further coordinated modeling activity and integration planning.

During Q3 of Y1, the group further coordinated modeling activity and integration planning.

During Q4 of Y1, the group further coordinated modeling activity and integration planning.

Starting from Y2 this group is integrated with the group, numerical methods for real-time modeling, working on modeling jointly.

6. Medical requirements and assessment

During Q1 of Y1, an extensive review of existing literature has been performed in order to understand the knowns and the needs for a liver injury model. At a basic level, blunt and penetrating liver injuries are suggested as the two key mechanisms of injury to be modeled by the project. Utilizing existing physical characteristics, including elasticity, capsular puncture resistance, the engineering team will create a 3D model of the liver. This model will need to have portal, arterial, and venous blood supplies in addition to the biliary tree. The model will also need to have fixation points akin to the suspensory ligaments and the vena cava.

Using an expert team of cardiovascular and liver surgeons, response of the model to an external injury will be assessed. The realism of the response will be graded and feedback given to fine tune the model.

Finally, the liver must respond to external forces such as suturing and packing with physical deformation and changes in the respective rates of hemorrhage.

During Q2 of Y1, the team developed an animal protocol for submission both internally at UCLA and to the military.

During Q3 of Y1, the team developed an animal protocol for submission both internally at UCLA and to the military. We received approval from IACUC and are awaiting approval from ACURO.

During Q4 of Y1, the internal UCLA veterinarians under IACUC suggested harvest of discarded fresh animal tissues from other experiments being performed at the UCLA animal facility. Our group has developed the technical expertise to harvest the liver once other experiments are complete. This will reduce or obviate the need for use of live animals.

During Q1 of Y2, the group had nothing to report.

During Q2 of Y2, we evaluated existing perfusion models and coordinated activity with the UCLA Department of Laboratory and Animal Medicine in order to utilize discarded animal tissue immediately after sacrifice. The team was able to harvest sample porcine livers successfully along with the hilum of the liver containing individual vessels. The group has now reconfigured a perfusion pump and static pressure bags of saline with osmotic additives in order to perfuse the liver in the short term and measure its mechanical properties with the systems delineated above. We have

successfully cannulated the hepatic artery and the portal veins and have an additional pump that returns the egress of the effluent back to a temperature-controlled reservoir.

During Q3 of Y2, two porcine liver harvest procedures were performed. The group also finalized the ex-vivo perfusion system design and completed construction of prototype.

During Q4 of Y2, two fresh porcine livers were harvested, and elastic properties were characterized along with Dr. Candler's group. The group made a contribution to a novel manuscript on the description of liver mechanical properties.

During Q9, we optimized the perfusion protocol of explanted porcine livers, in coordination with the UCLA Department of Laboratory and Animal Medicine. We were able to utilize the explanted livers from discarded tissue from other animal experiments. Surgical residents worked with bioengineering graduate students to harvest the liver including the hilar vessels to be applied to a modified perfusion setup. The system previously developed in Year 2 of the funding utilized a perfusion pump with static pressure bags with optimized perfusate. The osmotic composition of the perfusate allowed for rapid preservation while maintain the native tissue properties to allow for testing of physical forces with deformation. The research team also mastered technical methods of hepatic artery and portal vein cannulation. Using the described perfusion protocol, three additional livers were extracted and tested to help with characterization of deformation forces and to facilitate the work of Dr. Eldredge and Dr. Candler's teams.

During Q10, no further animal experiments were required. As Dr. Eldredge and Dr. Candler's team continued to provide further analyses on deformation forces and principles of hysteresis associated with liver compression, medical consultation was provided regarding physiologic parameters associated with liver injury. These goals were accomplished during this quarter with intention to advance basic modeling to scenarios of blunt and penetrating trauma to various hepatic segments during Q11.

During Q11, our bioengineering colleagues presented various modeling scenarios with representation of native fixation points of the liver such as the falciform and triangular ligaments. Based on clinical knowledge, feedback was provided to bioengineering team in modifications to modeling to reflect fixation forces present in both blunt and penetrating injuries of the liver. These modeling refinements were achieved and goals for Q12 are to continue tissue modeling, acquire additional patient-based data for machine learning training, and build open current models with physiologic parameters associated with hemorrhage.

During Q12, our primary goals were to optimize the addition of feedback to models of hepatic trauma that replicate physiologic reflexes to hemorrhage such as vasoconstriction. As medical consultants we reviewed the modeling by Mr. Canuto and Dr. Eldredge of large and small vessel vascular tree. We also aided in identifying fallacies in mathematical modeling that were not consistent with what is clinically known of the autonomic nervous system. These goals were achieved and plans for additional flow modeling with patient data were established. Based on the success of liver tissue deformation modeling paired with physiologic derangements, future directions were proposed to adopt similar modeling methods to the other circulatory organs, such as the lungs.

During Q13, the goal was to continue ongoing evaluation of physiologic parameters in the present mathematical models. No additional animal experiments were planned at this time. Proof-of concept completion was completed with plan for prototype testing in the upcoming year.

During Q14, our goals were to complete analysis of preliminary results and finalize proof-of concept. We also continued discussions and preliminary mathematical modeling for additional physiologic parameters such as the respiratory cycle and intrathoracic pressure variation to current simulation. No other updates to provide from this quarter.

7. Open standards development for virtual anatomic models

During Q1 of Year 1, there was nothing to report.

During Q2 of Year 1, the group began to plan GPU based open-standard work.

During Q3 of Year 1, the group furthered planning in GPU based open-standard work.

During Q4 of Year 1, We integrated a generic liver model with patient specific geometry to first study the model rendering complexity. We then integrated a C++ based in-house developed mass-spring approach for simulating the liver deformations. Our observations showed that while the SimTK platform was able to render the liver geometry in real-time as a surface shell, rendering the entire liver volume was limited. This is because of the limitation in the platform's ability to use the graphical processing units for a better rendering. An in-house developed rendering module showed that SimTK can be improved with such a rendering capability. In addition, our deformation capability also showed that while simple displacements limited the frame rate to <2 frames per second, instabilities caused by bone and other movements rendered even the most-simplistic mass-spring approach not compatible with SimTK for real-time purposes. Future studies will focus on approaches to use GPUs for further improving the deformation frame rates.

During Q1 of Y2, Virtual liver models are essential in simulation platforms dealing with virtual surgery and training. The complexity inherent in the liver functionality, which stems from the blood flow as well as complex liver movements render the deformations to be high in computational complexity. Integrating the comprehensive model requires a novel approach to the open standards prescribed for the medical simulation purposes. Conventional simulation platforms that support simulations with a generic computing setup (using Central Processing Unit) needs to be accommodated.

Our focus is on the medical applications related to surgical simulations, where the greatest importance is given to (a) the accuracy of the soft tissue deformation response, (b) the real-time nature of the computations, and (c) the usage of patient-specific geometry. There are many potential applications for such models, and have been investigated for application domains such as the virtual surgery simulation. Physics-based methods, such as finite element and mass-spring, allow for a broad array of simulations, from gross posture changes to subtle day-to-day deformations like tumor regression. Mass-spring systems typically employ a linear elastic material model, providing fast, stable deformations. However, biological tissues exhibit a hyper-elastic response beyond small

deformations. Finite element models can provide physiologically realistic deformations, but they can be computationally expensive and typically apply a tetrahedral meshing which may lower model resolution.

Our initial observation: We performed initial studies using SimTK, an NIH support open simulation platform, for better understanding the steps involved in such a development. We integrated a generic liver model with patient specific geometry to first study the model rendering complexity. We then integrated a C++ based in-house developed mass-spring approach for simulating the liver deformations. Our observations showed that while the SimTK platform was able to render the liver geometry in real-time as a surface shell, rendering the entire liver volume was limited. This is because of the limitation in the platform's ability to use the graphical processing units for a better rendering. An in-house developed rendering module showed that SimTK can be improved with such a rendering capability. In addition, our deformation capability also showed that while simple displacements limited the frame rate to <2 frames per second, instabilities caused by bone and other movements rendered even the most-simplistic mass-spring approach not compatible with SimTK for real-time purposes. Future studies will focus on approaches to use GPUs for further improving the deformation frame rates.

GPU based biomechanical modeling and integration with a opensim platform:

As a first step towards improving the computing time, we developed an open source mass spring GPU based approach for integrating with the simtk standards. The model mechanics were maintained to be simplistic enough to account for a generic tissue perturbation. Our analysis showed that the framerate can be improved from 2 to ~10 frames per second. The bottleneck was observed to be the interaction of the data from the CPU to the GPU.

During Q2 of Y2, Virtual liver models are essential in simulation platforms dealing with virtual surgery and training. The complexity inherent in the liver functionality, which stems from the blood flow as well as complex liver movements render the deformations to be high in computational complexity. Integrating the comprehensive model requires a novel approach to the open standards required for the medical simulation purposes. Conventional simulation platforms that support simulations with a generic computing setup (using Central Processing Unit) needs to be accommodated.

Our focus is to develop a simplistic machine learning platform that can learn liver deformations. Since the correlation between the observed voxel deformation and the YM distribution is not explicit, it can be construed that a direct correlation might not exist. To account for this, we developed a deep neural network model to transform the individual voxel deformations into the corresponding YM distributions. The deep neural network employed in this work is a fully connected seven-layer network. As inputs, we used the voxel’s Hounsfield intensity, 3D location, and deformations that were calculated from the virtual liver phantom. The output of the network was the YM associated with each voxel. The number of neurons in the hidden layer were optimized for the best result, ultimately settling at 200. A simple schematic of the network is shown in figure 2(a). Annotated data was then split between a training set and a test set as 25% to 75%, respectively. As the training data was fed through the DNN, a series of weights and biases were optimized to minimize a loss function. Currently, the most widely used approach for neural network training is

stochastic gradient descent (Bottou 2010). Stochastic gradient descent (SGD) trains on smaller batches of training data, called epochs. Within an epoch, the training batch is iterated through several times, randomly choosing data points to estimate the gradient. An adaptive sub-gradient method, with dynamic learning rates was employed for network training (Zeiler 2012).

The accuracy of the network was continually monitored by inferring an output from the test data, and comparing to the ground truth expectations. Figure 2(b) illustrates the flow of data for the full network architecture. The seven input values were sent through the hidden and output layers, while the known expectations (ground-truth YM values) were sent to the loss and accuracy functions. The result of the output layer was then sent to the loss function, accuracy function, and training algorithm, which updated the weights and biases of the hidden and output layers and were used to compute the network accuracy (further discussed in section 2.2.3).

Neuron activation function. The neurons of the hidden layer took the data from each neuron of the input layer, apply a matrix multiplication with weighting factors, add a bias, and then apply a non-linear activation function. These weights and biases are the values adjusted during training and allows the network to learn. Converting this to a non-linear response is important because a composition of linear functions remains a linear function, so the network abstraction is limited no matter its depth. The activation function chosen for this network was the sigmoid function (eq. 6) (Neilsen 2015). The sigmoid function is essentially a smoothed out step function that was chosen because there was no loss of data for negative values, which is typical for other activation functions, such as hyperbolic tangent and rectified linear unit function.

Loss and accuracy measures. The loss function was applied during training to calculate the error between the output of the feed-forward neural network YM inference and the ground truth YM values. Since the output of the network was intended to be a physical quantity, quadratic cost was implemented as the loss function (Kline and Berardi 2005, Neilsen 2015). The accuracy was calculated (in equation 8) as an absolute percent error between the estimated YM values and the ground truth YM values, with a target of 0.1 mm accuracy.

The accuracy reported was also averaged over the number of samples in the test data during training, and the number of samples in the independent data when inferred results with the fully trained network.

Supervised learning using the virtual phantom: the virtual liver phantom geometry was obtained from anonymized liver CT geometry of both a right and left liver. Each liver phantom voxel was assigned a normal ground-truth Young's modulus based upon the HU value of the source CT, with elasticity values ranging between 1 and 20 kPa—an extended approximation of the range of elastic modulus values for normal and fibrotic liver tissue (Santhanam, Min et al. 2010, Hinz 2012). This resulted in a locally heterogeneous elasticity distribution, which was further modified to represent different diseased tissue that might be seen in liver radiotherapy cases as described in section 3.2.3. The virtual liver phantom was deformed from the initial source geometry to a target geometry based on the boundary constraints derived from the 4DCT data while the displacement of each voxel of the virtual liver phantom was taken for the learning process.

During Q3 of Y2, we focused on developing a simplistic machine learning platform that can learn liver deformations. Virtual liver models are essential in simulation platforms dealing with virtual surgery and training. The complexity inherent in the liver functionality, which stems from the blood flow as well as complex liver movements render the deformations to be high in computational complexity. Integrating the comprehensive model requires a novel approach to the open standards required for the medical simulation purposes. Conventional simulation platforms that support simulations with a generic computing setup (using Central Processing Unit) needs to be accommodated.

We present a machine learning approach for estimating liver displacement measurements at a voxel-by-voxel level. Our approach employs a constrained Generalized Adversarial Neural Network (cGAN) that learns the liver tissue displacement distributions in a supervised manner. For generating the training data, we employed an inverse elasticity estimation process for a 4DCT dataset. A linear elastic biomechanical model was employed to estimate the liver tissue's displacement distribution for known deformation during a given breathing cycle as acquired by the 4DCT. The voxel-by-voxel elastic distribution was then taken as a label while the end-exhalation 4DCT geometry was taken as data for the learning process. Once trained, the cGAN generated the label (or elasticity) for given data (liver geometry) images. The estimated elasticity was then validated using (a) direct comparison with the ground truth elasticity data using an L2-norm, (b) comparison of the deformation vector fields generated using the cGAN estimated elasticity with ground truth deformation vector fields, and (c) regenerating synthetic 4DCT and comparing with the ground-truth 4DCTs using 3 image similarity metrics: Mutual Information (MI), Structured Similarity Index (SSIM), and Normalized Cross Correlation (NCC).

Since the correlation between the observed voxel geometry and the YM distribution is not explicit, it can be construed that a direct correlation might not exist. To account for this, we developed a deep neural network model to transform the individual voxel geometry into the corresponding YM distributions. The deep neural network employed in this work was a constrained Generalized Adversarial Network [24]. This network consisted of two neural networks, Generalizer and Discriminator networks. The generalizer network was focused on generating the label images that matched the training data. The matching process was performed by the discriminator network. The adversarial nature of the two networks enabled both the networks to be developed simultaneously. As inputs, we used the voxel's Hounsfield intensity while the output of the generator network was the YM associated with each voxel.

The generalizer network consisted of a 5-layer neural network, of which the first 3 layers were convolutional neural networks and the last 2 layers were regular fully connected neural networks. As the training data were fed through the generator, each layer of the neural networks worked as follows: The neurons of the hidden layer took the data from each neuron of the input layer, applied a matrix multiplication with weighting factors, added a bias, and then applied a non-linear activation function. Converting this to a non-linear response was important because a composition of linear functions remained a linear function, so the network abstraction was limited no matter its depth. The activation function chosen for this network was the sigmoid function [25]. The sigmoid function is essentially a smoothed-out step function that was chosen because there was no loss of data for negative values, which is typical of other activation functions, such as hyperbolic tangent

and rectified linear unit function. During the optimization process, the series of weights and biases associated with the generator network were optimized.

The discriminator network consisted of a 4-layer neural network of which the first 2 layers were convolutional neural networks and the last 2 layers were regular fully connected neural networks. The accuracy of the network was continually monitored by inferring an output from the discriminator. The input values for the discriminator came from the generator neural network and the ground truth labels. To compute the accuracy, the inputs were sent through the hidden and output layers. The result of the output layer was then sent to the loss function, accuracy function, and training algorithm. The loss function was applied during training to calculate the error between the output of the feed-forward neural network YM inference and the ground truth YM values. Since the output of the network was intended to be a distribution of a physical quantity, quadratic cost was implemented as the loss function [25, 26]. The weights and biases of the hidden and output layers associated with the discriminator network were updated to enable refining the discriminator network and ultimately the generator network.

Currently, the most widely used approach for neural network training is an ADAM optimizer, which is efficient in addressing large datasets. The method aims at updating the neural network weights based on the moments of the gradients. The approach is more suitable for the learning setup [27], where the gradients are sparse and invariant to re-scaling. Unlike conventional neural networks, the update for the network weights is performed for both the discriminator as well as generator deep neural networks. For scenarios where the discriminator does not effectively discriminate the generated YM values, the optimizer is performed to update the discriminator weights accordingly.

The virtual liver phantom geometry was obtained from anonymized liver CT geometry of both a right and left liver. Each liver phantom voxel was assigned a normal ground-truth Young's modulus based upon the HU value of the source CT, with elasticity values ranging between 1 and 20 kPa—an extended approximation of the range of elastic modulus values for normal and fibrotic liver tissue (Santhanam, Min et al. 2010, Hinz 2012). This resulted in a locally heterogeneous elasticity distribution, which was further modified to represent different diseased tissue that might be seen in liver radiotherapy cases as described in section 3.2.3. The virtual liver phantom was deformed from the initial source geometry to a target geometry based on the boundary constraints derived from the 4DCT data while the displacement of each voxel of the virtual liver phantom was taken for the learning process. Plans for the next quarter
Development of a simplistic machine learning platform for enabling even a simplistic CPU based simulation platform to compute deformations in real-time.

During Q4 of Y2, we focused on code development.

Code development for Training study*:* the lung geometry was obtained from anonymized lung 5DCT end-exhalation scans of both a right and left lung. The DVFs associated with the end-exhalation to end-inhalation CTs (generated from the 5DCTs [1]) were computed using an in-house optical flow registration and then used as the ground-truth displacement for the inverse elasticity estimation process [2, 3]. Each lung phantom voxel was assigned an initial ground-truth Young's modulus based upon the HU value of the source CT, with elasticity values ranging between 1 and

20 kPa—an extended approximation of the range of elastic moduli values for normal and fibrotic lung tissues [4, 5]. The resulting elasticity distribution and the source geometry were assigned the label and the data for the learning process, respectively. To this end, each lung anatomy was separated into left and right lungs and was resliced into 2D axial slices at 1 mm resolution. The elasticity was also represented in the same input format. The training process iterated for a fixed number of generator and discriminator updates.

Code development for Validation study: three different validation approaches were investigated. In the first approach, we compared the ground-truth with the cGAN generatd elasticity using an L2-Norm difference. From a clinical perspective, a systematic validation would include not only the elasticity distribution results but also the results obtained from its clinical usage. For this purpose, we integrated the estimated elasticity distribution and the source geometry with the biomechanical model. Once integrated, the biomechanical model generated 4D lung deformations for given boundary conditions. For our validation study, we compared the deformations obtained from the integrated model with the deformation vector fields of the ground-truth 4DCT datasets. Let $|d_{a,0}$ and $|d_a$ refer to the ground-truth and model generated displacements of voxel $|a$, respectively. A L2-norm difference was applied to quantitate the displacement differences on a voxel-by-voxel basis. The number of voxels that converged within a certain epsilon value of ground-truth was characterized as the error quantification for the GAN estimated lung elasticity distribution. It is formulated as follows:

$$|c_a = \begin{cases} 1: & \| |d_a| - |d_{a,0}| \| < \epsilon \\ 0: & otherwise \end{cases} \qquad (3)$$

$$|p(\epsilon) = \frac{\sum_1^n c_a}{n} \qquad (4)$$

In (3) above, $|(\epsilon)$ represents the threshold for the L2-norm of the deformation vector for each voxel $|a$ within the lung volume $|V$, and $|c_a$ represents the error for each voxel. Two different epsilon values were investigated. First, we looked at $|\epsilon_1 = 1$, or the percent of voxels that converged within 1 mm of the ground-truth deformation, as the resolution of many CT images is around one cubic millimeter. Secondly, since lung deformation can vary widely between patients and breathing phases, we looked at the percent of voxels that converged within 10% of the maximum deformation, or $|\epsilon_2 = 0.1 * \max_a(|d_a|)$. The percent accuracy $|p(\epsilon)$ was then tabulated by summing the $|c_a$ over all $|n$ voxels in lung volume $|V$ using (3) and (4).

Code development for Validation of the cGAN displacement generated 4DCT: while the convergence criteria provided a quantitative way to assess the elasticity estimation accuracy, an additional metric was necessary to ensure the precision of the estimated elasticity. Specifically, we wanted to ensure that the cGAN generated elasticity coupled with the boundary constraints could be used to warp the end-exhalation image to closely represent the end-inhalation image. In addition, the usage of image similarity metrics could quantify the accuracy of the ground-truth data. For this purpose, three different image similarity metrics were utilized. For each of the metrics, we assumed *x* as the cGAN generated end-inhalation CT and *y* as the ground-truth end-inhalation CT.

Mutual Information: mutual information (MI) is a symmetric and nonnegative similarity measure of entropy between two images that takes high values for similar images. Maximization of MI indicates complete correspondence between two images. MI assumes no prior functional relationships between the images, but rather a statistical relationship that can be evaluated by analyzing the images' joint entropy [6]. Although MI is normally applied to multimodal registration, it is often commonly used for lung alignment [7].

The mutual information is computed by comparing the image entropy values (i.e. a measure of how well-structured the common histogram is) as follows:

$$MI(x,y) = H(x) + H(y) - H(x,y) \quad (5)$$

where $H(x,y)$ is the joint entropy

$$-\sum_{x,y} p_{xy}(x,y) \log p_{xy}(x,y) \quad (6)$$

and $H(x)$ and $H(y)$ are the individual entropies

$$-\sum_{x} p_{x}(x) \log p_{x}(x). \quad (7)$$

Structural Similarity Index Metric: the Structural Similarity Index Metric (SSIM) examines structural changes that more closely correlate with a visual evaluation rather than differences that do not contribute to perceived image quality, which is important for lung [8-10]. It is formulated as follows [11]:

$$SSIM(x,y) = \frac{(2\mu_x\mu_y + c_1)(2\sigma_{xy} + c_2)}{(\mu_x^2 + \mu_y^2 + c_1)(\sigma_x^2 + \sigma_y^2 + c_2)} \quad (8)$$

Where the terms (μ) and (σ) represents the mean and variance of the voxel intensities in x and y, respectively. The SSIM can vary between -1 and 1, where a score of 1 indicates perfect similarity.

Normalized Cross Correlation: another image similarity metric that was used to assess the results of our study was normalized cross-correlation (NCC). NCC is a simple but effective similarity measure that is invariant to brightness and contrast variations [12]. NCC is less sensitive to linear changes in amplitude of grayscale values [12], which enables us to examine for potential intensity differences caused by the estimated elasticity. Also, NCC was previously used to overcome intensity changes caused by tissue compression difference between different breathing phases [13]. Like SSIM, NCC values range from a perfect match of 1 to a completely anti-correlated match of -1. The equation for calculating the NCC is shown as

$$NCC(x,y) = C_{xy}(\hat{x},\hat{y}) = \sum_{i,j \in R} \hat{x}(i,j), \hat{y}(i,j), \quad (9)$$

where $\hat{x}$ and $\hat{y}$ are intensity normalized images (cGAN elasticity generated end-inhalation and the ground-truth end-inhalation CT).

During Q9, a machine learning based lung tissue elasticity estimation using the lung elasticity estimated from 4DCT datasets and a linear elastic biomechanical model as the training data. The

lung data in cohort with liver data was used in order to systematically study the source of normal liver deformations that are typically induced by the lung itself.

The methods presented in this section shows the feasibility of estimating the lung tissue elasticity in real-time. The input data employed for the learning process stem for a biomechanically-based inverse elasticity estimated process. The elasticity estimated from this process is considered to be ground truth as a direct elasticity estimation for each patient is not practical. Future work would focus on using direct elastography imaging techniques such as the MRE, where the lung elasticity can be measured directly and will lead to a more reliable data generation for the learning process. Since the machine learning process is agnostic to the underlying imaging modality, future work would employ such imaging innovations into the learning process.

From a biomechanics perspective, our current work focused on using a linear elastic approach, which was applicable for most of the scenarios within the lung radiotherapy. However, we envision that for more complex diffuse lung diseases, a hyper elastic approach would be required. Future work would also focus on characterizing the hyper-elastic nature of the lung tissue elasticity, which will provide more information on the hyper compliance of the diseased tissues.

An additional usage of CT based lung tissue elastography stems from diseases such as Chronic Obstructive Pulmonary Disease (COPD), where imaging protocols with high dosage are not conventionally prescribed. Enabling the ability to extract lung tissue elasticity information from a single CT (e.g. end-exhalation CT) will enable critical advancements in the treatment and management of such diseases, which forms the focus of this section. Future work would investigate the usage of low dosage CT imaging techniques, which will enable expanding the application of the lung elastography for imaging dose sensitive lung diseases.

Finally, the computational time for this approach was approximately 24 hours in a Nvidia GTX titan card. However, once trained, the network was able to predict the lung elasticity in near-real-time. Future work would focus on developing a multi-GPU approach for the learning process, where the learning time can be significantly reduced. First, we present the elasticity accuracy generated from the machine learning process. Fig 1 shows a comparison of the cGAN generated elasticity (fig 1a) and the ground truth elasticity (fig 1b). It can be seen that the distributions substantially match each other. Specific lung substructures that have a higher elasticity in the ground-truth also have a higher elasticity in the cGAN generated elasticity distribution. This supports the fact that the lung elasticity distribution can be predicted using a machine learning approach.

The elasticity distributions are known to vary from one subject to another as well as with the disease complexity. To demonstrate the ability of our learning process to account for such variations, we present the elasticity distribution for a lung cancer patient with severe COPD. Fig 2 shows a comparison of the cGAN generated elasticity and the ground truth elasticity for a subject with both lung tumor and severe COPD prevalence. As seen from the ground truth images, the elasticity range in this case was lower than that of the case when the patient only has the lung tumor. It can be seen that the elasticity distributions generated by the cGAN match that of the ground truth elasticity significantly. This supports the fact that variations in the patient geometry as well as the disease pathophysiology can be represented by the machine learning approach presented in this section.

Table 1 documents the accuracy in learning the elasticity distributions for the 15 lung datasets. Results show that for the training data set, we obtained a learning accuracy of 0.44+/- 0.2 KPa. For the validation dataset, consisting of 13 4D datasets, we were able to obtain an accuracy of 0.87+/- 0.4 KPa as tabulated in Table 2. These results show that the cGAN generated elasticity correlates well with that of the ground-truth elasticity.

To further quantitate the accuracy, we integrated the cGAN generated elasticity into the biomechanical model, in order to simulate the lung deformation for given boundary constraints. The displacement vectors generated from this setup were then compared with the displacement vectors generated using the deformable image registration of the 4DCT datasets. Specifically, the deformation vectors from the end-exhalation dataset to the end-inhalation dataset was compared. Table 2 summarizes the results for the two accuracy measures discussed in section 2.6. For each of the measures, the cGAN-generated elasticity facilitated an accuracy of ~89%.

The resulting deformed model was then transformed into lung 4DCT images and the Image Similarity Metrics (ISMs) were applied. Our results as documented in table 2 show that the DNN generated images were very similar to that of the original 4DCT. The average value of the MI is 1.77 indicating the high local symmetricity between the ground truth and the cGAN elasticity generated 4DCT data. The average value of the structural similarity for the 13 patients was observed to be 0.89 indicating the high structure integrity of the cGAN elasticity generated 4DCT. In addition, the average NCC value of 0.97 indicates that potential variations in the contrast and brightness of the cGAN elasticity generated 4DCT did not led to any differences from the ground-truth 4DCT. In summary, it can be seen the differences in the ISMs are quite low. This bolsters the fact the DNN generated lung tissue elasticity can be employed within acceptable numerical boundaries.

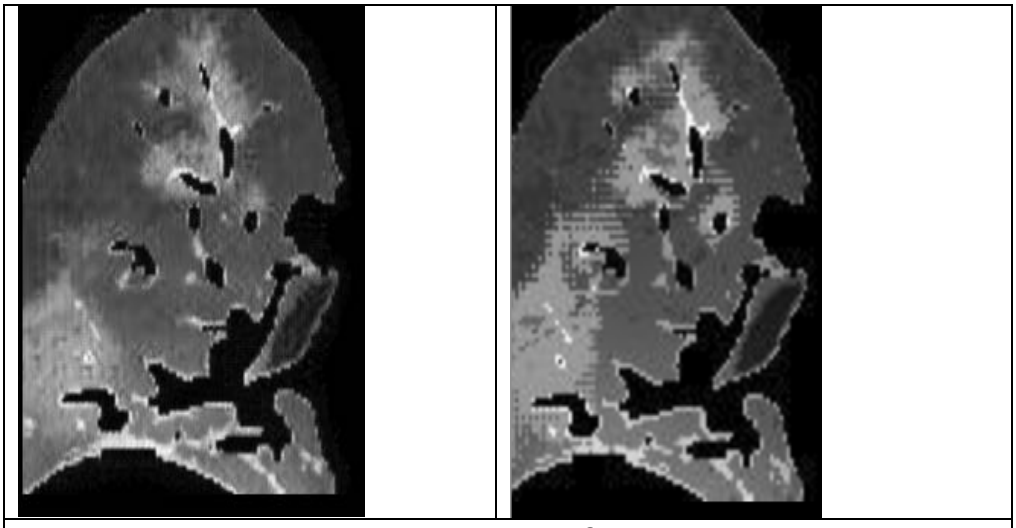

Fig 1. (a) Lung tissue elasticity estimated from the deep learning process. (b) Lung tissue elasticity distribution estimated from the model-guided elastography. The elasticity values range from < 1 KPa (grey) to 12 KPa (white) gray scale regions.

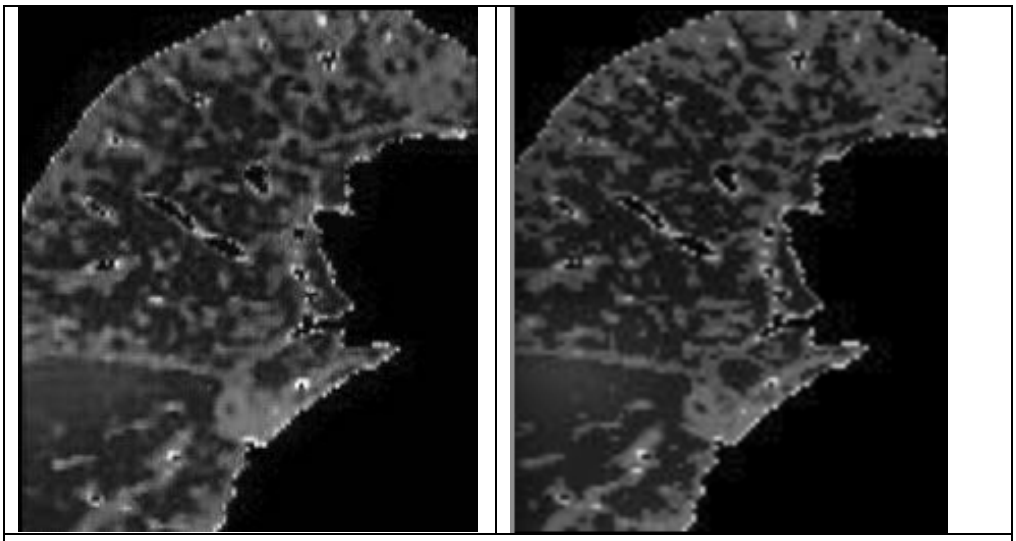

Fig 2. (a) Lung tissue elasticity estimated from the deep learning process. (b) Lung tissue elasticity distribution estimated from the model-guided elastography. The elasticity values range from < 1 KPa (grey) to 12 KPa (white) gray scale regions.

Table 1. Quantitative analysis of the lung elasticity estimation accuracy enabled by the deep learning framework

ID	**accuracy KPa**
1	0.3 ± 0.2
2	0.2 ± 0.1
3	0.4 ± 0.1
4	0.6 ± 0.2
5	0.3 ± 0.2
6	0.2 ± 0.1
7	0.2 ± 0.1
8	0.2 ± 0.1
9	0.4 ± 0.3
10	0.3 ± 0.3
11	0.2 ± 0.1
12	0.2 ± 0.1
13	0.3 ± 0.2
14	0.4 ± 0.4
15	0.2 ± 0.2
Average	0.4 ± 0.3

Table 2. Quantitative analysis of the 4DCT generated from the cGAN generated lung elasticity distribution

ID	Accuracy KPa	ϵ_1 accuracy (%)	ϵ_2 accuracy (%)	MI	SSIM	NCC
1	0.9 +/- 0.7	87.60	87.89	1.81	0.88	0.96
2	0.6 +/- 0.5	86.08	82.90	1.99	0.83	0.94
3	0.5 +/- 0.3	94.08	84.37	2.00	0.95	0.99
4	0.4 +/- 0.2	87.36	89.14	1.87	0.87	0.97
5	0.8 +/- 0.4	80.63	87.72	1.77	0.87	0.96
6	0.9 +/- 0.3	85.46	87.57	1.76	0.87	0.97
7	0.6 +/- 0.4	85.83	84.14	1.62	0.86	0.95
8	0.7 +/- 0.5	99.24	75.70	1.78	0.89	0.98
9	0.7 +/- 0.6	95.55	73.79	1.50	0.92	0.98
10	0.4 +/- 0.3	82.37	75.85	1.79	0.87	0.96
11	0.6 +/- 0.5	95.41	74.64	1.80	0.91	0.98
12	0.7 +/- 0.3	88.16	78.98	1.72	0.88	0.97
13	0.6 +/- 0.4	96.48	86.46	1.57	0.91	0.97
Average	**0.8 +/- 0.4**	**89.56**	**88.76**	**1.77**	**0.89**	**0.97**

During Q10, a machine learning based liver tissue elasticity estimation using the liver elasticity estimated from 4DCT datasets and a linear elastic biomechanical model as the training data. The liver data in cohort with liver data was used in order to systematically study the source of normal liver deformations that are typically induced by the liver itself.

Table 1. Quantitative analysis of the liver elasticity estimation accuracy enabled by the deep learning framework

LIVER ID	accuracy KPa
1	0.3 ± 0.2
2	0.2 ± 0.1
3	0.4 ± 0.1
4	0.6 ± 0.2
5	0.3 ± 0.2
6	0.2 ± 0.1
7	0.2 ± 0.1
8	0.2 ± 0.1

9	0.4 ± 0.3
10	0.3 ± 0.3
Average	0.4 ± 0.3

Table 2. Quantitative analysis of the 4DCT liver generated from the cGAN generated liver elasticity distribution

LIVER ID	**Accuracy KPa**	ϵ_1 **accuracy (%)**	ϵ_2 **accuracy (%)**	**MI**	**SSIM**	**NCC**
1	0.4 +/- 0.2	80.60	77.89	1.31	0.72	0.76
2	0.5 +/- 0.5	80.08	72.90	1.49	0.64	0.74
3	0.3 +/- 0.3	74.08	74.37	1.67	0.75	0.79
4	0.6 +/- 0.2	77.36	79.14	1.27	0.65	0.77
5	0.4 +/- 0.4	70.63	77.72	1.17	0.67	0.76
6	0.5 +/- 0.3	75.46	77.57	1.43	0.87	0.77
7	0.3 +/- 0.4	75.83	74.14	1.82	0.66	0.75
8	0.4 +/- 0.5	89.24	65.70	1.1	0.72	0.78
9	0.4 +/- 0.6	85.55	63.79	1.0	0.72	0.78
10	0.4 +/- 0.3	72.37	65.85	1.19	0.85	0.76
Average	**0.8 +/- 0.4**	**79.56**	**78.76**	**1.27**	**0.73**	**0.77**

During Q11, our major goals were as follows. Virtual liver models are essential in simulation platforms dealing with virtual surgery and training. The complexity inherent in the liver functionality, which stems from the blood flow as well as complex liver movements render the deformations to be high in computational complexity. Integrating the comprehensive model requires a novel approach to the open standards required for the medical simulation purposes. Conventional simulation platforms that support simulations with a generic computing setup (using Central Processing Unit) needs to be accommodated.
Our focus is to develop a simplistic machine learning platform that can learn liver deformations.

Variations in the machine learning optimization may lead to variations in the estimated liver tissue deformations. To systematically study this phenomenon, we implemented 4 different learning optimization algorithms, (a) gradient descent optimization, (b) ADAM optimization and (c) particle swarm optimization. Gradient descent optimization focused on following the gradients of the deformation accuracy until the minimum accuracy was achieved. ADAM optimizer focused on optimizing the elasticity based on the minimization of the moments. Finally, the Particle swarm optimization was employed as a way to address a multi-local minima optimization, where multiple elasticity distributions may provide the same deformation pattern observed in the 4DMR images. Our study showed that using the ADAM optimizer we were able to estimate the liver deformations consistently.

During Q12, our major goals were as follows. Virtual liver models are essential in simulation platforms dealing with virtual surgery and training. The complexity inherent in the liver functionality, which stems from the blood flow as well as complex liver movements render the deformations to be high in computational complexity. Integrating the comprehensive model requires a novel approach to the open standards required for the medical simulation purposes. Conventional simulation platforms that support simulations with a generic computing setup (using Central Processing Unit) needs to be accommodated.
Our focus is to develop a simplistic machine learning platform that can learn liver deformations.

We formulate hyperelasticity using a generalized Ogden material model, which defines a strain energy, *W*, in terms of principal stretches, λ_i, and a shear modulus, μ:

$$W = \sum_{p=1}^{N} \frac{\mu_p}{\alpha_p}\left(\lambda_1^{\alpha_p} + \lambda_2^{\alpha_p} + \lambda_3^{\alpha_p} - 3\right); where\ 2\mu = \sum_{p=1}^{N} \mu_p \alpha_p$$

where α_p is the hyperelastic model power term for parameter *p* of *N* parameters [41]. The principal stretches were be determined by solving for the image deformation tensor field eigenvectors. We employed the Ogden material model to experiment with a physically realistic range of strain-energy functions. The principal Cauchy stresses, σ_i, were be determined from the 2nd Piola-Kirchoff stress tensor, □□ which were itself be derived from the partial derivative of the strain energy *W* with respect to the principal stretches.

$$\sigma_i = \lambda_i \tau_i = 2\lambda_i \frac{\partial W}{\partial \lambda_i} = \sum_{p=1}^{N} \mu_p \lambda_i^{\alpha_p}$$

Machine learning for hyperelasticity*:* The Ogden model data inputs are: the FHFBCT images and associated deformation vector fields. Modeling the hyperelastic liver deformation associated with each liver voxel is a mathematically complex problem, mostly attributed to the size of hyperelasticity parameter search space and the fact that the hyperelasticity values may be degenerate, leading to multiple solutions for the same deformations. To this end, we employ the following two-step machine learning process to reduce the parameter search space and solve for the global minimum:

Step 1: Machine learning the initial hyperelasticity properties using a pseudo-direct hyperelasticity machine learning estimation procedure employing a Green's function model [18] and physics based airflow distribution.

Step 2: Refine the hyperelastic machine learning model employing a hyperelastic finite element deformation model that deforms the liver geometry for known actuation parameters and the hyperelasticity distribution estimated in step 1.

Our efforts in learning the hyperelastic liver deformations will lead to a first open sourced liver deformation setup that will be of high resolution and hyperelastic in nature (suitable for large deformations).

During Q13, our major goals were as follows. Virtual liver models are essential in simulation platforms dealing with virtual surgery and training. The complexity inherent in the liver functionality, which stems from the blood flow as well as complex liver movements render the deformations to be high in computational complexity. Integrating the comprehensive model requires a novel approach to the open standards required for the medical simulation purposes. Conventional simulation platforms that support simulations with a generic computing setup (using Central Processing Unit) needs to be accommodated. Our focus is to develop a simplistic machine learning platform that can learn liver deformations.

The two stages of a machine learning based open source liver deformation are (a) the learning process, and (b) the inferencing process. Learning the open source liver model with hyperelastic parameters is a more complex problem than estimating the linear elastic parameters. To this end, we need to employ a multi-GPU computing setup for learning the hyperelastic liver model. We developed an innovative parallelization algorithm that use a multitude of search directions for the hyperelastic parameters. A set of 52 GPUs were employed in this study to analyze the hyperelasticity of each liver anatomy. The ground-truth deformation was calculated from the 4DMR datasets using an optical flow based deformable registration algorithm. The computation time for this step was approximately 2 minutes. Once estimated, each of the GPUs were then loaded with the same patient dataset and ground truth deformations. A central GPU was assigned the task of integrating the search results and disseminating the results to the other GPUs. Each GPU was assigned the task of learning a single hyperelastic liver deformation at a given time step. At the end of 5 search iterations, the results were then transferred to single CPU that sorted the hyperelastic values based on the observed cost/error. The value with the minimum cost is set and the search process continued with that hyperelastic parameters as the starting point. The process continued until the learning process yielded a consistent result. Results, showed that we were able to converge quickly on the estimated liver deformation values. This enables a liver deformation hyperelastic model that enables open source liver deformations.
In our experiments, we investigated two learning processes for the open source liver deformations. First, we investigated a Constrained Generalized Adversarial Network. This network consisted of two deep neural networks, namely, a generator and the discriminator deep neural network. The generator network aimed at reproducing the liver deformations for given input force map computed for the required deformation. For instance, in the case of a projectile penetration, the force maps represent the projectile position. The discriminator deep neural network aimed at checking whether the reproduced liver deformations are accurate. To this end, each of the network consisted of 5 layers of convolution neural network followed by a 2 fully connected layers. An ADAM optimizer was employed for the learning process. The implementation was based on the Tensorflow ® machine learning interface. The result of this learning process is the generator deep neural network that can reproduce the liver deformations. The method had the benefit of being very accurate in representing the liver deformations. The method however required the force map to be accurate, which was complex. To address this, we further investigated the second approach, which consisted of a Recurrent Convolution Neural Networks (RCNN) approach. This framework consisted of a stack of convolution neural networks, where the output of one neural network is fed as input for the second neural network. The learning process was done in a supervised manner, where the output of the final neural network was compared with the observed simulation results. Ultimately, each of the convolution neural networks were optimized until the transient results closely matched that of the

simulation results. Thus, for any given initial projectile position, we computed the transient and final force maps using the RCNN and at each stage fed the output to the generator deep neural network for ultimately simulating the liver deformations.

The inferencing process forms the second part of the machine learning based open source liver deformations. Here, the learned deep neural network was employed for generating the liver deformations. Inherently, the neural networks are open source and so the matrix underlying in each of the neural networks can be implemented as required by the open source platform. For demonstration purposes, we employed a CUDA/C++ based inferencing process. The input to this framework consisted of the initial projectile position. The RCNN mapped the subsequent force maps, and for every force map, the generator computed the liver displacement. The implementation was only limited by the CPU/GPU and the memory. Using a Nvidia RTX 1070 GPU, we obtained real-time performance in the deformation.

During Q14, our major goals were as follows. Virtual liver models are essential in simulation platforms dealing with virtual surgery and training. The complexity inherent in the liver functionality, which stems from the blood flow as well as complex liver movements render the deformations to be high in computational complexity. Integrating the comprehensive model requires a novel approach to the open standards required for the medical simulation purposes. Conventional simulation platforms that support simulations with a generic computing setup (using Central Processing Unit) needs to be accommodated. Our focus is to develop a simplistic machine learning platform that can learn liver deformations.

We hypothesize that biomechanical modeling alone will be insufficient to characterize tissues for liver deformations. A goal of this aim is to also provide vessel maps that include vessels with sub-voxel cross sections. This is made possible by the quantitative nature of the imaging and the acquisition of numerous free-breathing images.

Reference Geometry: We first define a reference geometry, likely the geometry of the first MR scan. The selection of the specific reference condition is somewhat arbitrary except that it has to have unique spatial morphology and be able to be tied to the breathing amplitude and ultimately to the airflow model. The first helical CT scan meets both of these criteria.

We propose to take advantage of the quantitative nature of CT coupled with the multiple scan acquisition to map small bronchi and bronchi at sub-voxel resolutions. The justification for this is shown in Figure 7, where a bronchus has a sub-voxel diameter, but its impact on the voxel intensity can be measured as it transitions between two voxels.

Density-based subvoxel blood-vessel mapping: As also discussed in the biomechanical and graphical modeling, the voxel resolution of the FHFBCT scans are 1 x 1 x 1 mm^3, which corresponds to the diameter of the 6-10th bronchial generation. Further generations, such as bronchioles have sub-voxel diameters and might be considered to be undetectable. However, even sub-voxel bronchioles have an impact on the voxel density measurement. As the blood vessel moves between voxels, its impact on the MR voxel density can be predicted and mapped if there is a blood vessel tree (BT) map to guide vessel mapping.

Connectivity likelihood map using tubularity geometric features: Learning the *potential* existence of a bronchus is insufficient to develop the vessel map. We also connect the BT using a technique we recently developed for imaging and tracking the small bowel. We first generated a BT likelihood map over the imaged liver. Global geometric descriptors are challenging to identify the BT by themselves due to the variation of the BT shape between successive images. We employed both the global descriptor and density-based detection to characterize the chance of each pixel belonging to the BT. Our preliminary results of conducting this evaluation for the small bowel favored using a scale-optimized outward gradient flux[40-42], compared to alternatives such as Frangi[43] or bi-Gaussian filter[44].

Our initial results show that the open source liver model coupled with sub-voxel description of the liver blood vessel enables a high definition description of the liver deformations.

8. **Project Advisory Activity**

During Q1 of Year 1, meetings were initiated with Anders Larsson of Surgical Science, as well as Dr. Jeffrey Berkley of Mimic Technologies to discuss their level of involvement in the advisory panel.

One of the co-founders of Surgical Science, Anders Larsson is a pioneer in the medical training simulation industry. Beginning in 1997 with his simulated laparoscopic suturing tasks, continuing with the 2000 launch of LapSim and throughout the development of Surgical Science, Anders has been a catalyst for continued innovation in medical simulation throughout his career. In his current role as CTO, Anders leads the Surgical Science research and development team.

Dr. Jeff Berkley is the founder, Chairman and CEO of Mimic Technologies, which is both a pioneer and leader in Robotic Surgery Simulation. Jeff brings decades of experience in the mathematics, engineering and healthcare disciplines focused on technology and virtual reality applications. Jeff has applied his knowledge of haptic feedback and continuum mechanic-based tissue modeling to surgery simulation. He is well known as a leader in the fields of haptics, surgery simulation, and real-time finite element modeling. He has published numerous articles and has spoken at a wide variety of academic conferences. He has published and served as a reviewer for various journals such as IEEE Transactions on Visualization and Computer Modeling, Virtual Reality, and the Electronic Journal of Haptics Research and Medical Imaging.

During Q2 of Year 1, the group continued planning for advisory meetings.

During Q3 of Year 1, the group continued planning for advisory meetings.

During Q4 of Year 1, the medical team engaged with Drs. Plurad and Bricker, former military trauma surgeons, currently UCLA Harbor Trauma Department faculty. Discussions focused on various mechanisms of liver injury relevant to accurate physiological modeling of the tissues and fluids.

What opportunities for training and professional development has the project provided?
Professional development and training was provided to the following individuals:

Graduate Student Researchers:

- Daniel Canuto (Mechanical and Aerospace Engineering)
- Yi-Jui Chang (Mechanical and Aerospace Engineering)
- Qi Guo (Mathematics)
- Michael Reyes (Mechanical and Aerospace Engineering)
- Ling Li (Electrical Engineering)
- Ashkan Maccabi (Bioengineering)
- Ahmad Abiri (Bioengineering)
- Songping Sun (Bioengineering)
- Tao Zhou (Computer Science)
- Xuchen Han (Mathematics, Computer Science)
- Mengyuan Ding (Mathematics, Computer Science)
- Stephanie Wang (Mathematics, Computer Science)
- Omeed Paydar(Electrical Engineering)
- David Clyde (Mathematics)
- Gergely Klar (Computer Science)
- Steven Gagniere (Mathematics)

Postdoctoral Scholars:

- Dr. Kwitae Chong (Mechanical and Aerospace Engineering)
- Dr. Chenfanfu Jiang (Mathematics, Computer Science)
- Dr. Nathan Francis (Mechanical and Aerospace Engineering)
- Dr. George Saddik (Mechanical and Aerospace Engineering)
- Dr. Theodore Gast (Mathematics, Computer Science)

Surgical Resident Researchers:

- Yen-Yi Juo, M.D. (Surgery)
- Yas Sanaiha, M.D. (Surgery)

How were the results disseminated to communities of interest?
Journal paper on biomechanical organ modeling methodology published:

Hasse K, Neylon J, Santhanam A.P. *Feasibility and quantitative analysis of a biomechanical model-guided lung elastography for radiotherapy.* Journal of Biomedical Physics and Engineering (in press).

For *Numerical Methods for Real-Time Modeling,* we primarily published in the computer graphics and computational physics literature. This includes the prestigious ACM SIGGRAPH and ACM SIGGRAPH Asia editions of the journal ACM Transactions on Graphics.

For *Biomechanical and Graphical Modeling of Organs,* we published numerous articles detailed below.

For *Tissue Properties Measurement and Validation,* computer-aided minimally-invasive surgical procedures have rapidly increased in recent years. As a result, there is a high demand for realistic simulation models, both for use in virtual operative training platforms and for design of bioengineered liver tissue. However, one of the largest obstacles in achieving fidelity when developing virtual organ models is insufficient understanding of the mechanical behavior of soft tissues while interacting with surgical instruments. The liver is the largest solid organ in the abdominal cavity and represents one of the most commonly damaged organs during both blunt and penetrating injuries. Prior studies have described the mechanical properties of liver ex vivo without perfusion, ex vivo with perfusion, and in vivo. However, experimentation under in vivo conditions has proven challenging due to limited accessibility and unascertained boundary conditions in the abdomen. Ex vivo perfused livers presented very similar mechanical properties to those of in vivo livers. It has been shown that mechanical properties of a liver, following harvesting from the abdominal cavity, changed dramatically when perfusion ceased.

Currently there is a demand for a constitutive model of liver tissue, which can fully characterize its large spontaneous deformations during not only loading but also unloading processes (Figure 1). A variety of constitutive models have been proposed in the past with various levels of success: including hyperelastic, viscoelastic, and visco-hyperelastic (or hyper-viscoelastic) models. Hyperelastic models such as the Ogden, Mooney-Rivlin, and Neo-Hookean models can accurately characterize liver tissue behavior under large deformations (max strain >0.05) using at least 2 coefficients. However, they can only predict the loading process but cannot describe the unloading process which is not a simple reversal of the loading process due to energy dissipation. Viscoelastic models such as the Maxwell and Kelvin-Voigt models have simple formulae but they are only applicable to small deformations. Other viscoelastic models such as Quasi-linear viscoelastic, Viidik, and Holzapfel models are able to characterize hysteretic properties of liver tissue but they require heavy calculation which usually leads to an expensive computational process. Ayyildiz et al. developed a hyper-viscoelastic constitutive model combining a single parameter Neo-Hookean model in parallel with a twelve-parameter viscoelastic model to analyze the effect of the normal compression and strain rate on ex vivo sectioned bovine liver tissue. Although normal compression and torsional shear loading experiments were performed to optimally estimate the coefficient of the model using a rheometer, it can be hard to implement a model with 13 parameters in a real-time virtual tissue simulator. Marchesseau et al. proposed a model in consideration of the visco-hyperelasticity (based on the Arruda-Boyce material model and Prony series in series) and poroelasticity (with the assumption of the proportion of free-fluid the of liver as a constant fw = 0.8). The model was validated by conducting Dynamic Mechanical Analysis on ex vivo cylindrical porcine liver samples with a radius of 10 mm and height of 4 mm by using a rheometer. Vemaganti and Roan reported a visco-hyperelastic model by writing an exponential form of the hyperelastic strain energy function at time t as a convolution integral where the material parameter is time-dependent. Uniaxial compression tests on cylindrical bovine liver tissue ex vivo at a maximum

strain rate of 0.01 s-1 were conducted to obtain the coefficients. However, all of the visco-hyperelastic models mentioned above were characterized on ex vivo sectioned liver samples due to the requirements and limitations of using a rheometer or performing uniaxial compression tests. Besides, none of the studies mentioned above described both the loading and unloading processes of liver testing cases.

In this work, we first measured the force-displacement hysteresis curves of harvested porcine livers under indentation tests, both as a whole organ under physiologic perfusion conditions and as sectioned tissue segments immersed in saline solution. Quasi-static indentation tests at different locations on a liver lobe and dynamic indentation tests at different loading/unloading rates were conducted in both experimental settings. Then data of indentation tests were converted to stress-strain curves of equivalent unconfined compression tests. Visco-hyperelastic models with least number of coefficients (≤6 for mathematical simplicity) were used to fit the hysteretic curves.

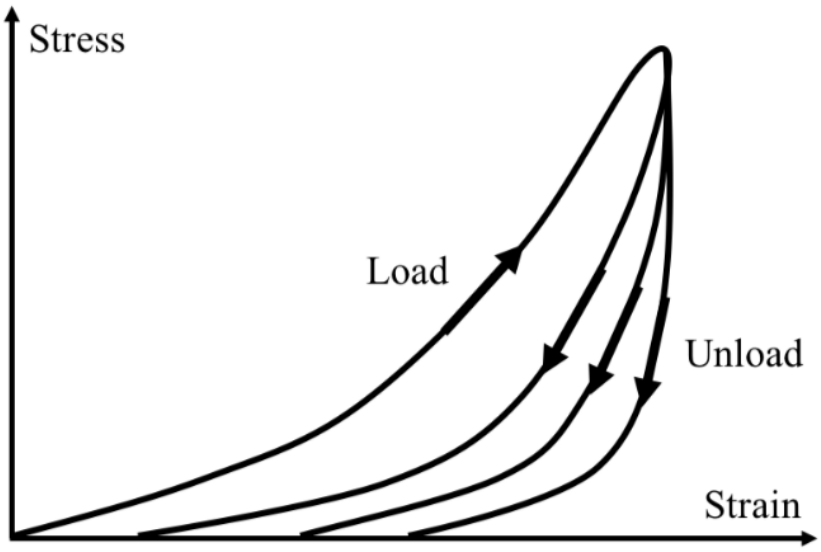

Figure 1: Representative hysteresis curves of different soft biological materials with the same loading behavior but different unloading behaviors.

For *Medical Requirements and Assessment*, results were disseminated to fluid dynamics and the medical community through peer-reviewed publications and presentations and national conferences.

What do you plan to do during the next reporting period to accomplish the goals?
Nothing to report

4. IMPACT:

What was the impact on the development of the principal discipline(s) of the project?
For *Numerical Methods for Real-Time Modeling*, we showed that machine learning is an effective tool for generating real-time simulation capabilities from large libraries of simulation data generated

in offline, high-detail simulation. Furthermore, we developed a new simulation technique for simulating and visualizing soft-tissue injuries from projectiles and other blunt force trauma that drastically improve the state-of-the-art.

For *Biomechanical and Graphical Modeling of Organs,* liver deformation is essential for enabling a quantitative understanding of the liver and the overall lower abdomen physiology. However, liver deformation for normal physiological conditions is complex to model while they can be quantitatively observed in the 4D Magnetic Resonance Imaging. UCLA Radiation Oncology and Radiology employs 4D MR imaging for liver cancer radiotherapy treatments. Liver elastography is a critical component for enabling the liver deformation model. Liver diseases, such as liver cancer and cirrhosis, are commonly associated with changes in the biomechanical properties of liver tissue. Functional imaging techniques such as elastography have shown great promise in measuring the biomechanical properties of liver tissue; however, current liver elastography techniques require additional equipment that is conventionally not available within the radiotherapy setup. We present a novel methodology for estimating liver elasticity derived from deformation observed during 0.35 T 4DMR ViewRay (MRIdian System™, ViewRay™, Cleveland, OH, USA) scans within a radiotherapy setup. Phase 1 and phase 8 datasets, categorized by diaphragm position, were first deformably registered. The resulting displacement maps were considered ground-truth. A GPU-based biomechanical model was then assembled from the segmented phase 8 liver dataset and, along with patient-specific boundary constraints, used to iteratively solve for the liver elasticity distribution. The liver elastography process presented here was performed for a set of 11 4DMR patients. Maximum liver deformation was observed to be between 3.99 and 9.04 mm. On average, 95% convergence within 1 mm was observed. A validation study using phase 4 liver datasets illustrated an accuracy of 86%. Normalized cross-correlation quantified high similarity between the results of the estimation and validation studies with their respective ground-truths. Overall, the results suggest that liver elasticity can be measured with approximately 95% convergence using 4DMR scans acquired within the radiotherapy workflow, indicating the potential for the implementation of liver elastography within the clinic.

Liver deformations and modeling is a complex computational task that cannot be achieved in real-time using low-end computing platforms. A machine learning approach where the normal behavior of the liver undergoing breathing induced deformations is ideal for simulation and modeling applications, which forms the focus of this paper. In our approach, we employed a 4DMR image dataset acquired for liver cancer patients undergoing radiotherapy treatment. The individual liver volumes were registered using a multi-resolution optical flow platform to compute the liver deformations range. We then employed an adversarial network-based learning approach to learn the liver deformations for known elastic distributions obtained using model guided elastography. The neural network generated (a) liver elastography results, and (b) liver deformations for given liver geometry and stimulus representing the lung breathing phase. Results showed that using conventional low-end computing platforms, real-time liver deformations can be obtained in real-time.

For *Medical Requirements and Assessment,* the impact of this project on the development of theoretical multiscale models of biologic tissues has been tremendous. We have for the first time perfused a complex organ, the liver, with various pressures and measured its viscoelastic properties.

Using complex algorithms, the group has been able to integrate such empiric parameters and produced highly realistic models for the bleeding liver.

What was the impact on other disciplines?

For *Numerical Methods for Real-Time Modeling,* our algorithmic developments will be useful to the greater computational mechanics literature. In particular, we have developed new techniques for simulated porous liver filled with blood. These techniques can be used for general porous media. Furthermore, our novel techniques for simulating and visualizing ductile failure in the liver can be used for ductile failure of general materials. Lastly, our machine learning advances for simulating tissues in real-time can be used for a wide range of materials whose dynamics are not overly driven by inertia.

For *Biomechanical and Graphical Modeling of Organs,* other disciplines were impacted in the following ways:

Impact on Liver Imaging: In this paper, we presented the results of a liver elastography process performed on 11 4DMR datasets. A physics-based biomechanical model was used to solve the inverse elasticity problem. Liver DVFs from the registration of phase 1 and phase 8 diaphragm positions were obtained using an in-house optical flow DIR algorithm. Liver boundary displacements were employed as boundary constraints, while the inner liver tissue voxels were allowed to deform according to linear elastic material properties.

On average, 95% of voxels for 11 patients converged within 1.0 mm of ground-truth deformation. Maximum deformation ranged from 3.73 to 9.04 mm for the estimation cohort. The average elasticity ranged from 2.69 to 6.42 kPa. The average values found here correspond well with those found in the current work in the field (Singh, Venkatesh et al. 2015, Venkatesh, Yin et al. 2015, Zeng, Cai et al. 2017). In addition, an image similarity metric showed high similarity between the phase 8 and warped phase 1 registration and experimental results, with values of 0.97 and 0.97 respectively. Overall, these results suggest that liver elastography can be performed using ViewRay 4DMR datasets for a wide range of patients.

The potential of 4DMR liver elastography to be used in the clinic requires extensive validation. Phase 4 datasets were obtained as a validation cohort so that the elasticity results could be validated in a clinically-relevant manner. The maximum deformation ranged from 2.59 to 7.88 mm for the validation cohort, and 86% of voxels converging within 1 mm of clinical ground-truth deformation. An image similarity metric again showed high similarity between phase 4 and warped phase 1 registration and validation model results, with values of 0.97 and 0.90 respectively. Future work will investigate obtaining MRE data for patients so the elasticity distributions can be more explicitly and quantitatively validated.

Impact on Liver Surgery/Radiotherapy: Hepatocellular carcinoma (HCC) is one of the most common malignancies, and the third most common cause of cancer-related death worldwide (Jung, Yoon et al. 2013, Jun, Kim et al. 2017). Surgical resection and liver transplantation are the primary treatment methodologies, however strict criteria limit the pool of eligible patients for both cases. HCC has a poor prognosis, with a 5-year survival rate of less than 12% due to a combination of late

diagnosis and lack of efficient therapies for advanced stages (Affo, Yu et al. 2017). Stereotactic body radiotherapy (SBRT) has been used to treat patients with HCC who are not eligible for other treatments (Feng, Suresh et al. 2017). SBRT uses advances in imaging and conformal radiotherapy to deliver ablative, high dose radiation in order to optimize local control.

Radiation-induced liver disease (RILD) is a significant limiting factor in the use of SBRT because there are no effective treatments or predictors (Jung, Yoon et al. 2013). Most patients with HCC have pre-existing cirrhosis or hepatitis, which increases their risk of RILD (Kim, Kim et al. 2015). Baseline liver function is thought to be the most important factor associated with risk of RILD (Jun, Kim et al. 2017). Pre-treatment visualization of liver function in vivo is necessary in order to expand the use of SBRT for HCC.

The liver plays a role in metabolism, synthesis, secretion, immunity, and many other functions (Luna, Cunha et al. 2014). Liver disease, including cirrhosis, fibrosis and tumors, can disrupt the functions of the liver by altering the biomechanical properties of the tissue, most notably by changing the tissue stiffness (Sandrasegaran 2014, Li, Min et al. 2015). Clinically, elastography provides a measurement of liver stiffness and is a predictor for HCC (Pepin, Chen et al. 2014). Magnetic resonance elastography (MRE) can noninvasively and quantitatively assess the elasticity characteristics of soft tissue (Li, Min et al. 2015). Liver stiffness measured by MRE has been shown to correlate well with histologic staging of fibrosis and differentiation of benign and malignant liver lesions (Venkatesh, Yin et al. 2015). However, current MRE techniques require equipment that is not typically available within a radiotherapy setup.

Our elastography process focuses on estimating the effective Young's modulus for each voxel of liver tissue using 4DMR liver data. Figure 1 shows a flow chart summarizing the elasticity estimation. First, phase 1 and phase 8 datasets from the 4DMR liver images were registered using an optical flow deformable image registration (DIR) algorithm (Min, Neylon et al. 2014). Liver deformation vectors (DVFs) were obtained for every voxel of liver tissue. The biomechanical model was then assembled using segmented phase 1 liver geometry and a randomly initialized elasticity distribution. Using the ground-truth liver DVFs, the elasticity distribution was optimized. The inverse elasticity problem was formulated as a parameter-optimization problem with an objective to determine the elasticity parameter that would minimize the difference between the ground-truth deformation and the deformation computed by a biomechanical model. The biomechanical model and inverse elasticity estimation were implemented on a GPU cluster, which allowed the elasticity estimation for each patient dataset to converge in around 2 hours. Spatial elasticity and displacement error distributions were then obtained and validated.

Impact on Artificial Intelligence: The liver geometry was obtained from anonymized lung 4DMR end-exhalation scans. The DVFs associated with the end-exhalation to end-inhalation CTs (generated from the 5DCTs 36) were computed using an in-house optical flow registration and then used as the ground-truth displacement for the inverse elasticity estimation process 37, 38. The resulting elasticity distribution, the deformation vector field, and the source geometry were assigned the label and the data for the learning process, respectively. The training process iterated for a fixed number of generator and discriminator updates. For our validation study, we compared the deformations obtained from the DNN generated model with the deformation vector fields of the ground-truth 4DMR datasets representing different breathing phases.

To demonstrate the impact of Artificial Intelligence in liver deformations, we applied the liver deformation models for a specific problem, where we required the CT electron density maps must be accurately estimated to achieve valid dose calculation in a MR-only radiotherapy. The goal of this study is to assess whether the conditional generative adversarial network (cGAN) can generate accurate abdominal synthetic CT (sCT) images from 0.35T MR images for MR-only liver radiotherapy. A retrospective study was performed using CT images and 0.35T MR images of 12 patients with liver (n = 8) and non-liver abdominal (n = 4) cancer. CT images were then deformably registered to the corresponding MR images to generate deformed CT (dCT) images for treatment planning. The cGAN was trained using both MR and dCT transverse slices. Four-fold cross-validation testing was conducted to generate sCT images for all patients. The HU prediction accuracy was evaluated by voxel-wise similarity metric between each dCT and sCT image for all 12 patients. dCT-based and sCT-based dose distributions were compared using gamma and dose-volume histogram (DVH) metric analysis for 8 liver patients. The cGAN achieved 89.8 HU. The average gamma passing rates within all volumes of interest were higher than 95% using a 2%, 2 mm criterion, and 99% using a 3%, 3 mm criterion. The average differences in the mean dose and DVH metrics were within ±0.6% for the planning target volume and within ±0.15% for evaluated organs in both models. Results: demonstrated that abdominal sCT images generated by the cGAN and achieved accurate dose calculation for 8 liver radiotherapy plans.

For *Medical Requirements and Assessment,* the work accomplished by the group has greatly advanced our understanding of the mechanics of liver tissue as it responds to surgical and non-surgical trauma. We are able to visualize bleeding injuries and create liver deformations with external pressure as is produced during surgery. The mathematical and hyperelastic models of the liver have been produced, a major leap in biologic modelling.

What was the impact on technology transfer?

For *Numerical Methods for Real-Time Modeling,* the worked supported by this effort resulted in 5 published papers, 1 submitted papers, and 1 in preparation paper.

For *Biomechanical and Graphical Modeling of Organs,* two disclosures are being prepared:

- 4DMR guided liver elastography
- Liver model for CT/MR calibration and commissioning

For *Medical Requirements and Assessment*, the numerical and empiric methods created during the course of this project are being made available to the public. We hope for the passive dissemination of our findings by interested parties.

What was the impact on society beyond science and technology?

For *Numerical Methods for Real-Time Modeling,* simulation of surgery will have a transformative effect on medicine and how surgeons are trained. Our efforts have helped to make these transformative techniques a reality.

For *Biomechanical and Graphical Modeling of Organs*, the impact will be further quantitatively known when the product will be commercialized.

For *Medical Requirements and Assessment*, the development of the visco-elastic model of liver deformations paired with physiologic, high-fidelity simulations of the autonomic system will impact society in numerous ways. Currently, medical simulation has limited capability in modeling tissue deformations and physiologic derangements such as hemorrhage realistically. This work will allow for improved medical training and patient management in emergency, combat scenarios as well as patient-centered care with models that will aid surgeons in surgical planning of routine major surgery.

5. CHANGES/PROBLEMS:

Changes in approach and reasons for change

Dr. William Klug, who was leading the effort on constitutive modeling of tissue in this project, tragically was killed on 1 June 2016. In his absence, Dr. Eldredge — with whom he collaborated closely — has assumed duties for leading this effort, in close consultation with Dr. Teran.

We conducted compression tests on ex vivo rat liver tissue. However, there were several issues that occurred during the measurements. First, the rat liver was too small and couldn't provide enough test samples for measurements. Second, the rat liver was too thin (3-mm-thick rat liver sample compared to 10-mm-porcine liver sample) which made the samples stickier to the probe. Each time when we detached the sample from the probe and replaced it on the stage, tissue was damaged and as a result the loading history was changed. Third, it was difficult to cut off the heterogeneous part from rat liver to make sample homogeneous and uniform due to the sample thickness. To get more reliable data, at least one more porcine liver is required in the future measurements.

For *Numerical Methods for Real-Time Modeling*, initially, we had intended to use a larger GPU based simulation component for simulating real-time surgery. We investigated this and while we did achieve a tenfold speed up over manycore level parallelism, we hoped we could achieve better rates. Machine learning has gained ground in a wide range of computational disciplines over the last few years and were able to adjust our approach to leverages this more than we had anticipated.

For *Biomechanical and Graphical Modeling of Organs,* changing from an open source deformation model to an AI based deformation model. Our initial approach is to develop GPU based implementations of hyper-elastic material point method. However, based on our analysis, we found it to be computationally complex. Thus, we developed an AI based platform for representing the biomechanical liver deformation.

Actual or anticipated problems or delays and actions or plans to resolve them

For *Numerical Methods for Real-Time Modeling*, we needed to no cost extension to wrap up the last aspects related to machine learning and ductile fracture simulation. This was enough time for us to wrap up the last few developments.

For *Biomechanical and Graphical Modeling of Organs***,** developing an AI based biomechanical model requires an extensive amount of data generation from biomechanical models, analysis using the AI platform. We have put in place, an inhouse GPU based cluster for developing and analyzing the AI biomechanical model.
We are now exploring 3D printing as a means to generate simple yet realistic mesh models of deformable constructs

Changes that had a significant impact on expenditures
Nothing to report

Significant changes in use or care of human subjects, vertebrate animals, biohazards, and/or select agents
Nothing to report

Significant changes in use or care of human subjects
Nothing to report

Significant changes in use or care of vertebrate animals
Nothing to report

Significant changes in use of biohazards and/or select agents
Nothing to report

6. PRODUCTS:

- **Publications, conference papers, and presentations**

  Journal publications.

Q. Guo, X. Han, C. Fu, T. Gast, R. Tamstorf, J. Teran, *A Material Point Method for Thin Shells with*
Frictional Contact, ACM Transactions on Graphics (SIGGRAPH 2018), 37(4), pp. 147:1-147:15, 2018.

C. Fu, Q. Guo, T. Gast, C. Jiang, J. Teran, *A Polynomial Particle-In-Cell Method*, ACM Transactions on
Graphics (SIGGRAPH Asia 2017), 36(6), pp. 222:1-222:12, 2017.

C. Jiang, T. Gast, J. Teran, *Anisotropic Elastoplasticity for Cloth, Knit and Hair Frictional Contact*, ACM Transactions on Graphics (SIGGRAPH 2017), 36(4), pp. 152:1-152:14, 2017.

A. Pradhana, T. Gast, G. Klar, C. Fu, J. Teran, C. Jiang, K. Museth, *Multi-species Simulation of Porous Sand and Water Mixtures*, ACM Transactions on Graphics (SIGGRAPH 2017), 36(4), pp. 105:1-105:12, 2017.

G. Klar, T. Gast, A. Pradhana, C. Fu, C. Schroeder, C. Jiang, J. Teran, *Drucker-Prager Elastoplasticity*
for Sand Animation, ACM Transactions on Graphics (SIGGRAPH 2016), 35(4), pp. 103:1-103:12, 2016.

Hasse K, Han F, Neylon J, Min Y, Hu P, Yang Y, and Santhanam A.P. 2018. *Estimation and validation of patient-specific liver elasticity distributions derived from 4DMR*. Biomedical Physics and Engineering Express 4(4).

Hasse K, Neylon J, and Santhanam A.P. 2017. *Feasibility and quantitative analysis of a biomechanical mode-guided lung elastography for radiotherapy*. Biomedical physics and engineering express 3(2).

Santhanam A.P., Hasse K, Stiehl B, and Low D. 2018. *A Generative Adversarial Network based biomechanical model of liver for model guided liver deformable image registration*, In Preparation

Santhanam A.P., Hasse K, Stiehl B, and Low D. 2018. *Simulating surgical procedures using an AI based liver deformation model*, In Preparation

Li, L., Maccabi, A., Abiri, A., Juo, Y.Y., Zhang, W., Chang, Y.J., Saddik, G.N., Jin, L., Grundfest, W.S., Dutson, E.P. and Eldredge, J.D., 2019. *Characterization of perfused and sectioned liver tissue in a full indentation cycle using a visco-hyperelastic model*. Journal of the mechanical behavior of biomedical materials, *90*, pp.591-603.

S. Wang, M. Ding, T. Gast, L. Zhu, S. Gagniere, C. Jiang, J. Teran, *Simulation and Visualization of Ductile Fracture with the Material Point Method* , Proc ACM on Computer Graphics and Interactive Techniques, 2(2) , pp. 18, 2019.

X. Han, T. Gast, Q. Guo, S. Wang, C. Jiang, J. Teran, *A Hybrid Material Point Method for Frictional Contact with Diverse Materials* , Proc ACM on Computer Graphics and Interactive Techniques, 2(2) , pp. 17, 2019.

Canuto, D., Pantoja, J.L., Han, J. et al. *An ensemble Kalman filter approach to parameter estimation for patient-specific cardiovascular flow modeling*. Theor. Comput. Fluid Dyn. 34, 521–544 (2020).

Books or other non-periodical, one-time publications.
Nothing to report

Other publications, conference papers and presentations.
Nothing to report

Website(s) or other Internet site(s)
Nothing to report

Technologies or techniques
Nothing to report

Inventions, patent applications, and/or licenses
Nothing to report

Other Products
Nothing to report

7. PARTICIPANTS & OTHER COLLABORATING ORGANIZATIONS

What individuals have worked on the project?
Provide the following information for: (1) PDs/PIs; and (2) each person who has worked at least one person month per year on the project during the reporting period, regardless of the source of compensation (a person month equals approximately 160 hours of effort). If information is unchanged from a previous submission, provide the name only and indicate "no change".

Example:

Name:	*Mary Smith*
Project Role:	*Graduate Student*
Researcher Identifier (e.g. ORCID ID): 1234567	
Nearest person month worked:	*5*
Contribution to Project:	*Ms. Smith has performed work in the area of combined error-control and constrained coding.*
Funding Support:	*The Ford Foundation (Complete only if the funding support is provided from other than this award.)*

Name:	Peyman Benharash
Project Role:	PD/PI
Researcher Identifier (e.g. ORCID ID):	
Nearest person month worked:	6

Contribution to Project: Provided guidance and oversight of the entire project, coordinated research efforts among investigators, provided specific guidance on tissue properties and clinical correlation as well as integration of cardiovascular model into the tissue one.
Funding Support:

Name: Joseph Teran
Project Role: Co-PD/PI
Researcher Identifier (e.g. ORCID ID):
Nearest person month worked: 5
Contribution to Project: Developed and supervised modeling and reanimation of physics based models to recreate organ response to injury using empiric parameters. Developed machine learning algorithms to reduce prohibitive computational burden of real-time calculations in order to render an accurate Virtual environment.
Funding Support:

Name: Jeff Eldredge
Project Role: Co-I
Research Identifier (ORCID): 0000-0002-2672-706X
Nearest person month worked: 12
Contribution to Project: Prof. Eldredge led the development of virtual fluid-tissue modeling methodology and implementation.

Name: Robert Candler
Project Role: Co-I
Researcher Identifier (e.g. ORCID ID):
Nearest person month worked: 2
Contribution to project: Provided guidance on tissue property measurements and data analysis.
Funding Support: Office of Naval Research
National Science Foundation

Name : Anand P Santhanam
Project Role: Co-Investigator
Researcher Identifier (e.g. ORCID ID):
Nearest person month worked: 14
Contribution to project: Development of a physiologically and anatomically accurate liver model with patient-specific elasticity measured using a novel 4D liver MRI protocol.
Funding Support:

Name: Ling Li
Project Role: Graduate Student
Researcher Identifier (e.g. ORCID ID):

Nearest person month worked: 16
Contribution to project: Designed experimental setup for measurement of tissue mechanical properties. Used this setup to perform measurements to determine mechanical properties of tissue. Developed a mathematical model to represent the tissue. Matched experimental data with mathematical data
Funding Support: Office of Naval Research

Name: Omeed Paydar
Project Role: Graduate Student
Researcher Identifier (e.g. ORCID ID):
Nearest person month worked: 2
Contribution to project: Assisted with measurements of mechanical properties of liver tissue
Funding Support:

Name: Chenfanfu Jiang
Project Role: Graduate Student/Postdoc
Researcher Identifier (e.g. ORCID ID):
Nearest person month worked: 12
Contribution to Project: Mr. Jiang worked to develop mesh failure, contact and cutting support for ductile fracture of soft tissues. He also worked on general computing infrastructure needed for the project.
Funding Support:

Name: Mengyuan Ding
Project Role: Graduate Student
Researcher Identifier (e.g. ORCID ID):
Nearest person month worked: 12
Contribution to Project: Ms. Ding worked to develop mesh failure, contact and cutting support for ductile fracture of soft tissues. She also worked on general computing infrastructure needed for the project.
Funding Support:

Name: Xuchen Han
Project Role: Graduate Student
Researcher Identifier (e.g. ORCID ID):
Nearest person month worked: 12
Contribution to Project: Mr. Han worked to develop mesh failure, contact and cutting support for ductile fracture of soft tissues. He also worked on general computing infrastructure needed for the project.
Funding Support:

Name: Qi Guo
Project Role: Graduate Student
Researcher Identifier (e.g. ORCID ID):
Nearest person month worked: 13
Contribution to Project: Mr. Guo worked to develop mesh failure, contact and cutting support for ductile fracture of soft tissues. He also worked on general computing infrastructure needed for the project as well as machine learning based acceleration of elasticity computations.
Funding Support:

Name: Chuyuan Fu
Project Role: Graduate Student
Researcher Identifier (e.g. ORCID ID):
Nearest person month worked: 6
Contribution to Project: Ms. Fu worked to develop novel MPM transfer techniques as well as general computing infrastructure needed for the project.
Funding Support:

Name: David Clyde
Project Role: Graduate Student
Researcher Identifier (e.g. ORCID ID):
Nearest person month worked: 3
Contribution to Project: Mr. Clyde worked on elasticity discretizations and on inverse problems for elastic parameter determination.
Funding Support:

Name: Gergely Klar
Project Role: Graduate Student
Researcher Identifier (e.g. ORCID ID):
Nearest person month worked: 3
Contribution to Project: Mr. Klar worked on elasticity discretizations and on MPM GPU implementations.
Funding Support:

Name: Theodore Gast
Project Role: Graduate Student/postdoc
Researcher Identifier (e.g. ORCID ID):
Nearest person month worked: 12
Contribution to Project: Mr. Guo worked to develop mesh failure, contact and cutting support for ductile fracture of soft tissues. He also worked on general computing infrastructure needed for the project as well as GPU accelerated MPM implementations.
Funding Support:

Name: Stephanie Wang
Project Role: Graduate Student
Researcher Identifier (e.g. ORCID ID):
Nearest person month worked: 12

Contribution to Project: Mr. Wang worked to develop mesh failure, contact and cutting support for ductile fracture of soft tissues. She also worked on general computing infrastructure needed for the project.
Funding Support:

Name: Steven Gagniere
Project Role: Graduate Student
Researcher Identifier (e.g. ORCID ID):
Nearest person month worked: 6
Contribution to Project: Mr. Gagniere worked to develop mesh cutting support for ductile fracture of soft tissues. He also worked on general computing infrastructure needed for the project.
Funding Support:

Name: Daniel Canuto
Project Role: Graduate Student
Researcher Identifier (e.g. ORCID ID):
Nearest person month worked: 36
Contribution to Project: Mr. Canuto developed the methodology for network simulations of the cardiovascular system, which were coupled with the simulations of the perfused liver.

Name: Yi-Jui Chang
Project Role: Graduate Student
Researcher Identifier (e.g. ORCID ID):
Nearest person month worked: 40
Contribution to Project: Mr. Chang developed methodology for the virtual tissue simulations, which account for tissue deformation and blood flow in the perfused liver.

Name: Adam Abiri
Project Role: Graduate Student/Postdoc
Researcher Identifier (e.g. ORCID ID):
Nearest person month worked: 8
Contribution to Project: Assistance with animal work and support as an engineering graduate student/post-doc
Funding Support:

Name: Songping Sun
Project Role: Graduate Student
Researcher Identifier (e.g. ORCID ID):
Nearest person month worked: 6
Contribution to Project: Assistance with animal work and support as a graduate student
Funding Support:

Name: Yen-Yi Juo
Project Role: Postdoc
Researcher Identifier (e.g. ORCID ID):

Nearest person month worked: 13
Contribution to Project: . Assistance with animal work and support as a surgical resident
Funding Support:

Name: Yas Sanaiha
Project Role: Postdoc
Researcher Identifier (e.g. ORCID ID):
Nearest person month worked: 5
Contribution to Project: Provided instrumental expertise in tissue harvest, set up of in-vitro pressurized measurements, creation of clinical framework for liver injury in blast and projectile impact.
Funding Support:

Has there been a change in the active other support of the PD/PI(s) or senior/key personnel since the last reporting period?
Nothing to report

What other organizations were involved as partners?
Nothing to report

8. SPECIAL REPORTING REQUIREMENTS

COLLABORATIVE AWARDS: *For collaborative awards, independent reports are required from BOTH the Initiating Principal Investigator (PI) and the Collaborating/Partnering PI. A duplicative report is acceptable; however, tasks shall be clearly marked with the responsible PI and research site. A report shall be submitted to* ***https://ers.amedd.army.mil*** *for each unique award.*

QUAD CHARTS: *If applicable, the Quad Chart (available on https://www.usamraa.army.mil) should be updated and submitted with attachments.*

9. APPENDICES:

Attach all appendices that contain information that supplements, clarifies or supports the text. Examples include original copies of journal articles, reprints of manuscripts and abstracts, a curriculum vitae, patent applications, study questionnaires, and surveys, etc.